
A Clock Laser System for Quantum Simulations with Ultracold Strontium Atoms

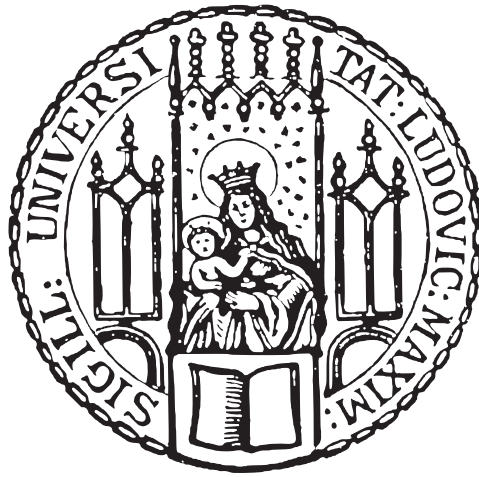
Rudolf Haindl



München 2019

Ein Uhrenlasersystem für Quantensimulationen mit ultrakalten Strontiumatomen

Masterarbeit an der Fakultät für Physik
Ludwig-Maximilians-Universität München



vorgelegt von
Rudolf Haindl
aus Traunstein

München, den 30. September 2019

Abstract

I report on my work done in the strontium experiment in Prof. Immanuel Bloch's group at the Max Planck Institute of Quantum Optics under the supervision of Dr. Sebastian Blatt, which was part of my Master's program at Ludwig Maximilian University of Munich. My work is split into three main projects. I report on the development of high bandwidth photodetectors in the strontium laboratory. I then describe the design of a fiber noise cancellation system for the active compensation of environmental influences on a narrow-linewidth laser coupled into a fiber. Lastly, I analyze the frequency fluctuations of our first-generation reference cavity for frequency stabilization of the clock laser and the red MOT laser and describe the design and construction of a second-generation reference cavity, whose zero crossing temperature I finally determine.

Contents

1	Introduction and Outlook	1
2	Model of a Laser	3
2.1	Tools for the analysis of a periodic signal	3
2.2	Amplitude and phase modulation	6
2.2.1	Amplitude Modulation	7
2.2.2	Phase Modulation	7
2.3	More General Noise Processes	11
2.4	Theory of a Laser	13
2.4.1	Planck's Law of Radiation	14
2.4.2	Einstein's Coefficients Describing a Laser	16
2.5	Noise Processes on a Laser	18
2.5.1	Formalism to Understand Line Shapes from Noise Processes	19
2.5.2	Lorentzian Line Shape of a Laser	20
2.5.3	Gaussian Line Shape of a Laser	21
2.5.4	Discussion of Line Shapes in Real Lasers	22
3	Feedback Theory and Electronics	24
3.1	Control System Basics	24
3.1.1	Laplace Transform	25
3.1.2	Low-pass Filter	25
3.2	Feedback Systems	27
3.2.1	Basic Active Electronic Circuits using Feedback	28
3.2.2	Integral Gain	30
3.2.3	A Combination of a Proportional Element with an Integrator	31
3.3	Description of a Phase-locked loop (PLL)	33
4	The Strontium Laboratory Photodetector	36
4.1	The Photodetector Circuit	36
4.1.1	A Model for a Photodiode	36
4.1.2	Transimpedance Amplifier	37
4.2	Testing the Bandwidth of the Fast Photodetector Board	40
5	A Phase-locked Loop for Fiber Noise Cancellation	48
5.1	Optical Heterodyne and Homodyne Mixing	48
5.2	Noise from a Fiber	50

5.3	Optical Setup	51
5.4	Electronic Setup	53
5.4.1	Choice of Oscillators	54
5.4.2	Extracting the Error Signal from the Beat Signal	55
5.4.3	Proportional Integral and Derivative Controller	55
5.4.4	Frequency Divison and Amplifier	58
5.5	Characterization of the Fiber Noise Cancellation System	58
5.6	Future Improvements of the Fiber Noise Cancellation System	62
6	Stability Analysis of the First-generation Cavity	63
6.1	Optical Resonators	64
6.2	Design Criteria for the Reference Cavity Housing	66
6.2.1	Pressure Fluctuations	67
6.2.2	Temperature Fluctuations	67
6.2.3	Vibration Fluctuations	69
6.3	Active Temperature Stabilization of Outside of the Aluminum Cavity	70
6.4	Resonance Frequency Drift of the Cavity in the Aluminum Housing	73
7	Design, Assembly and Characterization an Optical Resonator Housing	76
7.1	Choice of the Optical Resonator and the Support Platform	76
7.2	Design of a Steel-chamber Housing for an Optical Resonator	76
7.2.1	Stainless Steel Vacuum Chamber	77
7.2.2	Temperature Control of the Optical Resonator	78
7.2.3	Vibration isolation of the Steel-Chamber Cavity	79
7.3	Assembly of the Stainless Steel Chamber Cavity	79
7.3.1	Cleaning of the Vacuum Parts	79
7.3.2	Assembly of the Inner parts of the Cavity	80
7.4	Analysis of the Temperature Properties of the Steel Chamber Cavity	84
8	Testing the Second-generation Cavity	90
8.1	Pound-Drever-Hall Frequency Stabilization	90
8.2	Residual Amplitude Modulation (RAM)	92
8.3	Finesse Measurement of the Cavity	98
8.4	Optical Heterodyne Mixing of Two Narrow Lasers	99
8.5	Determining the Zero Crossing Temperature of the Optical Resonator	102
8.5.1	Resonance Frequency Drift caused by a Change of Temperature	102
8.5.2	The Zero Crossing Temperature of the Optical Resonator	104
8.6	Thermal Coupling of the Optical Resonator to the Copper Box	105
9	Conclusion and Outlook	107
	Acknowledgements	108
	References	110

Selbstständigkeitserklärung

117

List of Tables

2.1	Colors of Different Noise Processes	12
7.1	Fitted Time Constants of the Bakeout Process	88

List of Figures

1.1	Simple Level Diagram of Strontium	1
2.1	Illustration of the Autocorrelation Function and the Power Spectral Density	5
2.2	Phasor Representation of the Oscillation	6
2.3	Amplitude Modulation of a Signal	7
2.4	Phase Modulation of a Signal	8
2.5	Phase Modulation of a Signal	9
2.6	Double Sideband Modulation	10
2.7	Color Noise Spectra of the Phase Noise Spectrum $S_{\phi\phi}(f)$ and the Frequency Noise Spectrum $S_{\omega\omega}(f)$	13
2.8	Einstein Coefficients leading to Absorption, Spontaneous Emission and Stimulated Emission Processes	17
2.9	Illustration of a Lorentzian Power Spectral Density of the Electric Field . .	20
2.10	Illustration of a Gaussian Spectrum of the Electric Field	22
3.1	Low-pass Filter Schematic and Transfer Function	26
3.2	Sketch of a Linear Feedback System	28
3.3	Non-inverting and Inverting Operational Amplifier Configuration	29
3.4	Operational Amplifier in Integrator Configuration	30
3.5	Operational Amplifier in Proportional Gain Configuration with Capacitive Elements	32
3.6	A Phase-locked Loop System	34
4.1	Model of a Photodiode	37
4.2	Schematic of the Transimpedance Amplifier	38
4.3	The Gain of the Transfer Function of the Transimpedance Amplifier	39
4.4	Schematic of the Fast Photodiode Version V1.1	41
4.5	Test Setup for Determining the Bandwidth of the Photodetector	43
4.6	Test Setup for the Measurement of the Fast Photodiode's Bandwidth	44
4.7	Determining the Parasitic Capacitance of the Fast Photodiode	45
4.8	Comparison of Different Photodetectors Noise Power Spectral Densities . .	46
5.1	Schematic of a Heterodyne and a Homodyne Mixing Process	49
5.2	Optical Setup of the Fiber Noise Cancellation System	52
5.3	Electrical setup of the Fiber Noise Cancellation	54
5.4	Schematic of a PID-controller	56
5.5	Electronic Setup for the Test of the Fiber Noise Cancellation	59

5.6	Plot of Phase Noise on the Out-of-loop Photodetector from Single Frequency Modulation	60
5.7	The Effect of Fiber Noise Cancellation on the Peak Height of Single Frequency Noise at Different Frequencies	60
5.8	Plot of the Suppression of Phase Noise by the Fiber Noise Cancellation System	61
6.1	Plot of the Frequency-dependent Transmission through a Cavity	65
6.2	Picture of the Wood Box Surrounding the First-generation Cavity	70
6.3	Plot of the Overlapping Allan Deviation of the First-generation Cavity	72
6.4	Analysis of the Resonance Frequency Drift of the Aluminum Chamber	74
7.1	Half Section View of the Stainless Steel Vacuum Chamber	77
7.2	Pictures of the Stainless Steel Chamber and the Sidewall of the Copper Box	81
7.3	Pictures of the Thermistors with Waterjetted Form and of The Inner Heat Shield.	82
7.4	Picture of the Cavity Housing before the Vacuum Bakeout	83
7.5	Mounting of the Optical Resonator in the Vacuum Housing	84
7.6	Schematic of the Temperature Control of the Cavity	85
7.7	Temperature Ringdown of the Copper Box	86
7.8	Analysis of the Time Constants of the Bakeout Procedure	88
8.1	Schematic of a Pound-Drever-Hall Frequency Stabilization Setup	91
8.2	Test Setup for the Detection of Residual Amplitude Modulation caused by an EOM	95
8.3	The Overlapping Allan Deviation of Residual Amplitude Modulation on a Bulk EOM	96
8.4	The Overlapping Allan Deviation of Residual Amplitude Modulation on a Fiber EOM	97
8.5	Ringdown of the Cavity	99
8.6	Heterodyne Mixing Setup to compare two Lasers	100
8.7	Heterodyne Mixing Signal of Two Frequency-stabilized Lasers	101
8.8	Exponential Change of the Beat Signal	103
8.9	Measurement of the Zero Expansion Temperature	104
8.10	The Fitted Time Constants for a Heating Process of an Optical Resonator .	105

Chapter 1

Introduction and Outlook

In the last decade, strontium has become increasingly popular in the atomic physics community. Being an alkaline-earth atom, it exhibits a rich electronic structure of singlet and triplet states allowing for a variety of applications from optical lattice clocks [1, 2] to superradiant active clocks [3], tweezer arrays [4, 5], photoassociation of strontium molecules [6, 7], and a continuously loaded Bose-Einstein condensate [8].

Chronologically, the atomic structure of strontium was first explored in detail while building strontium lattice clocks [9, 10]. Lattice clocks probe the narrow intercombination line between the 1S_0 state and the 3P_0 state, called the clock transition, with a narrow linewidth laser (see Fig. 1.1).

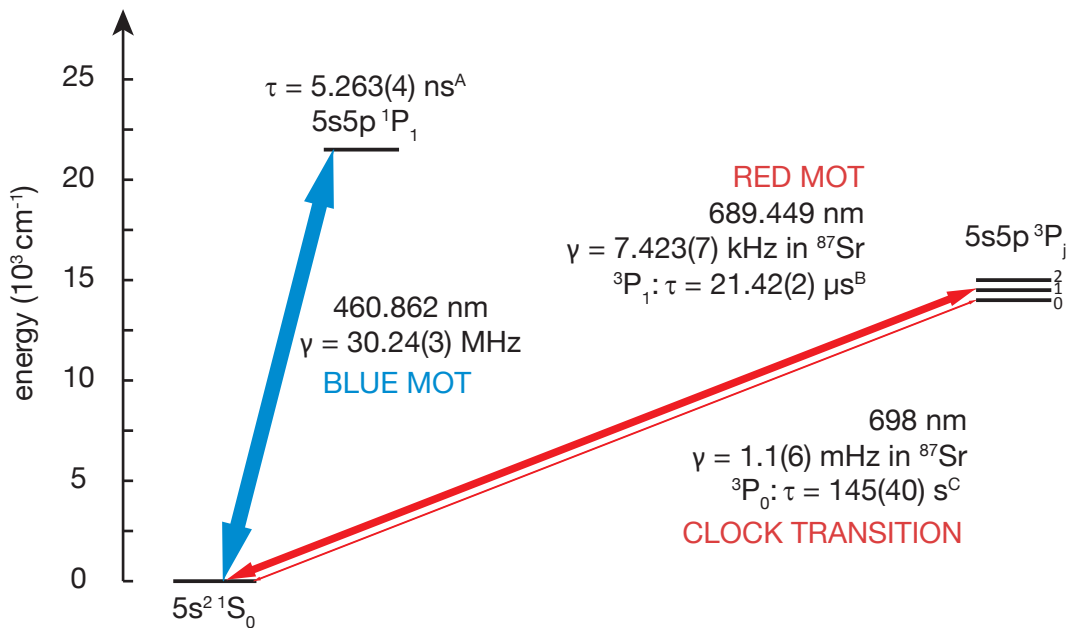


Fig. 1.1 Simplified level diagram of strontium. The clock transition connects the 1S_0 state and the 3P_0 state. The red MOT transition connects the 1S_0 state and the 3P_1 state. Lifetimes taken from ^A: [11], ^B: [12], ^C: [13]

The strive for better frequency uncertainty led to a systematic evaluation of the atomic level structure of strontium [1] and paved the way to use strontium for the simulation of quantum many body physics [14].

With the observation of Bose-Einstein-condensation of the bosonic isotopes of strontium ^{88}Sr , ^{86}Sr and ^{84}Sr [15] and a degenerate Fermi gas of ^{87}Sr [16], a new generation of strontium lattice clocks based on quantum degenerate gases is now being developed [17].

In our experiment we want to apply lattice clock technology to build a novel quantum simulator, which we will image and control with high resolution optics. With the $^1\text{S}_0$ state and the long-living $^3\text{P}_0$ state and their tuneout wavelengths [18, 12], we can generate state dependent lattices for strontium atoms. To excite atoms in the $^3\text{P}_0$ state with high fidelity, we need to address the atoms with a narrow-linewidth laser.

In this thesis, I report on the design of a clock laser system for quantum simulations with ultracold strontium. To do so, I first introduce a simple model of a laser (Chapter 2) and review basics of feedback control (Chapter 3). Furthermore, I describe the scheme of a phase-locked loop which can provide phase-stable laser light. In Chapter 4, I review the strontium laboratory design of fast photodetectors, which can be adapted to the gain/bandwidth requirements of specific applications. In the following Chapter 5, I describe the design and characterization of a fiber noise cancellation system used to reduce the spectral broadening of a narrow linewidth laser through acoustic noise in an optical fiber. I further review optical resonators and analyze the frequency stability of our first-generation cavity system in the strontium laboratory (Chapter 6) followed by a description of the design and construction of the second-generation cavity system in Chapter 7. With this second generation cavity system we aim for a frequency stability of the optical resonator of 10^{-15} . Lastly, in Chapter 8, I explain measurements of residual amplitude modulation of light passing an electro-optic-modulator which can cause uncontrolled frequency drifts. With two lasers stabilized to the first-generation cavity and the second-generation cavity, respectively, I give an upper bound on the instantaneous linewidth of the two lasers and measure the zero crossing temperature of the second-generation optical resonator.

Chapter 2

Model of a Laser

In this chapter we introduce a simple model for a laser to show how noise can influence its spectrum. First, we will understand both the time-domain picture and the frequency spectrum of a general oscillator. Using both the time-domain and the frequency-domain, we then show how amplitude- and phase-modulation can be used to get an understanding for noise processes. Finally, we derive how the spectral profile of a laser arises and how to analyze the laser's line shape.

2.1 Tools for the analysis of a periodic signal

We model the emitted electric field by a laser with the cosine function

$$E(t) = E_0 \cos(\omega_L t + \phi), \quad (2.1)$$

with real amplitude E_0 , frequency ω_L , and phase ϕ . The model describes a cosine wave with period $T = 1/(2\pi\omega_L)$. In the following, changes in phase within $\phi = [0, 2\pi\omega_L t/T)$ will be allowed. Later, this model will help us to understand laser noise properties of a narrow-linewidth laser, such as a clock laser (see Cha. 1). After introducing a more realistic laser model in Sec. 2.4, we will see how to apply the mathematical concepts derived in this Section.

First, we introduce the correlation function between two complex signals $V_A(t)$ and $V_B(t)$ [19]

$$G_{V_A V_B}(\tau) = \langle V_A^*(t) V_B(t + \tau) \rangle = \lim_{T \rightarrow \infty} \frac{1}{2T} \int_{-T}^T V_A^*(t) V_B(t + \tau), \quad (2.2)$$

where $2T$ is the observation time. Within the observation time, the correlation function measures how much the two signals $V_A(t)$ and $V_B(t)$ differ from each other, by averaging the product of $V_A(t)$ and $V_B(t)$ but delayed by time τ .

The phase noise of a signal can be analyzed by looking at the coherence of the signal which describes how much a periodic signal deviates from its original shape after a given amount of time. In other words, a signal's coherence is a measure for how much information of

the original signal is lost over a time interval τ . A measure for the coherence of a complex signal $V(t)$ is the autocorrelation function [19]

$$G_{VV}(\tau) = \langle V^*(t)V(t + \tau) \rangle = \lim_{T \rightarrow \infty} \frac{1}{2T} \int_{-T}^T V^*(t)V(t + \tau). \quad (2.3)$$

To illustrate Eqn. (2.3), we consider two different signals E_A and E_B obeying the model described in Eqn. (2.1). Both signals have the same amplitude E_0 and frequency ω_L , but signal E_B is phase-shifted from signal E_A by a phase shift $\Delta\phi$, i.e. $\phi_A = 0$ and $\phi_B = \Delta\phi$. Multiplying both signals gives

$$E_A(t)E_B(t) = E_0 \cos(\omega_L t)E_0 \cos(\omega_L t + \Delta\phi) = \frac{E_0^2}{2} [\cos(2\omega_L t + \Delta\phi) + \cos(\Delta\phi)]. \quad (2.4)$$

The product $E_A \times E_B$ has twice the frequency of the initial signals. Signals E_A , E_B and $E_A \times E_B$ are illustrated in Fig. 2.1(a).

The correlation function of E_A and E_B from Fig. 2.1(a) depends on the phase shift between the two cosine waves when averaging over a time interval $t' > t$. This means that the term $\propto \cos(2\omega_L t)$ in Eqn. (2.4) averages to zero and the correlation function is only dependent on the phase shift between the two periodic signals. Therefore, the correlation function resembles a cosine at frequency $f = 1/T$, the frequency of both E_A and E_B . Therefore one can see that the correlation function is periodically modulated by an increase in phase shift ϕ as shown in Fig. 2.1(b).

But how can the autocorrelation function tell us something about the coherence of a signal? Looking at the absolute value of the normalized autocorrelation function [19]

$$|g_{VV}(\tau)| = \left| \frac{\langle V^*(t)V(t + \tau) \rangle}{\langle V(t) \rangle^2} \right|, \quad (2.5)$$

one expects $|g_{VV}(\tau)| = 1$ for perfectly coherent signals, because the signal does not lose phase information over time. Hence, the signal's autocorrelation value does not decrease. For signals with lower coherence properties this value will decrease since phase perturbations change the signal's phase over time. The signal from Eqn. (2.1) is a perfectly coherent function according to this definition even if the cosine term modulates the amplitude of the signal. However, the amplitude of the signal goes back to its initial value after one oscillation period. This means $|g_{AA}(\tau)| = 1$ when averaging over one oscillation period, i.e. there is no decrease of coherence. A degradation of the coherence would therefore correspond to a decreasing envelope of the amplitude of the oscillation in Fig. 2.1(b). A detailed discussion of processes that can lead to lower coherence properties can be found in Sec. 2.3.

Having introduced the autocorrelation function, we can also introduce the power spectral density of a signal (PSD). Using the Wiener-Khinchin theorem one can relate the autocorrelation function of a signal to its power spectral density [20]

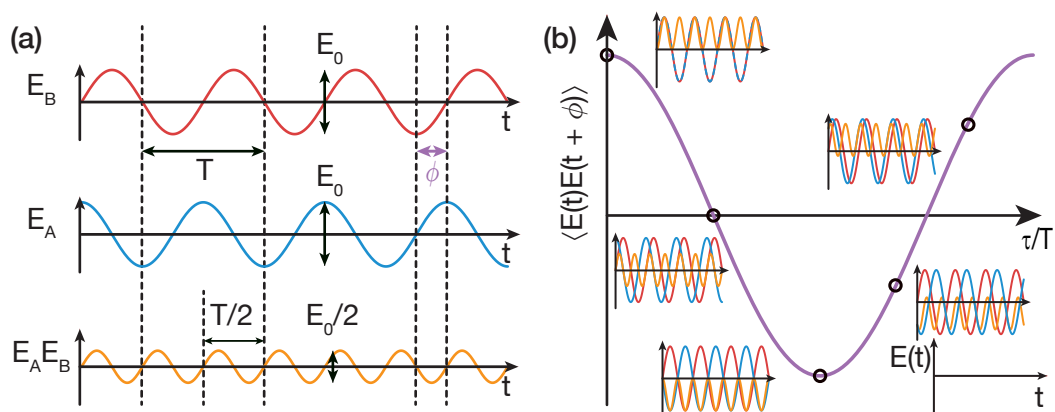


Fig. 2.1 Illustration of the signals E_A , E_B and $E_A \times E_B$ and the autocorrelation function of signal E_A . (a) The y-axis gives the value of $E(t)$ and the x-axis gives the time t . Traces E_A and E_B show an oscillation of $E(t)$, where E_B is shifted in phase by $\phi = -\pi/2$ with respect to E_A . The frequency of both oscillations is given by $f_A = f_B = 1/T$ and the amplitude of the oscillation is E_0 . Signal $E_A \times E_B$ corresponds to the multiplication of the red and the blue trace. Here the frequency is $f_{AB} = 2/T$ and the amplitude is $E_0/2$. (b) The y-axis gives the expectation value of the multiplication of signal E_A and E_B . This value is plotted against the phase delay in units of τ/T of the two cosine waves. The insets show the signals E_A , E_B and $E_A \times E_B$ corresponding to the phase delay between signal E_A and E_B given in the black circle superimposed on one plot.

$$S_{VV}(f) = \int_{-\infty}^{\infty} G_{VV}(\tau) e^{-i2\pi f\tau} d\tau. \quad (2.6)$$

This Fourier transform of the autocorrelation function describes how the power of the signal $V(t)$ is distributed over frequency space, i.e. it assigns a power to each Fourier frequency of $V(t)$. The example function $E(t)$ only has one single Fourier frequency. Therefore, the PSD of the signal is a single Dirac-Delta distribution at frequency ω_L . If the signal $V(t)$ describes a voltage, it is measured on a load resistance R . The power measured at this load is then defined as $P = V(t)^2/R$. Therefore the autocorrelation function can be correlated to units of power. Fourier transforming the autocorrelation leads to the Fourier domain of the power given in units of V^2/Hz , which is a power density over a spectral interval. Especially for periodic signals, the PSD can be useful in determining which periodicities the signal under test contains, i.e. how many different Fourier frequencies besides the carrier frequency contribute to the spectrum.

Another good way to picture periodic signals is to rewrite them in their phasor representation. In Eqn. (2.1) we described a periodic signal by a cosine function. We can express the cosine by an exponential function by plugging in Euler's formula $\exp(ix) = \cos(x) + i \sin(x)$ into Eqn. (2.1). In the phasor picture, a periodic signal is described both by the real and the imaginary part of the exponential expression. However, we can

measure only the real quantity

$$E(t) = E_0 \operatorname{Re}[e^{i(\omega_L t + \phi)}], \quad (2.7)$$

where $E(t)$ is only defined for positive frequency values ω_L . The graph in Fig. 2.2 shows the signal $E(t)$ in a frame rotating at frequency ω_L , i.e. signals with frequency ω_L do not rotate in this frame, while static signals would oscillate with frequency $-\omega_L$. The length of the arrow is given by the amplitude of the signal and ϕ is the angle with respect to the real axis.

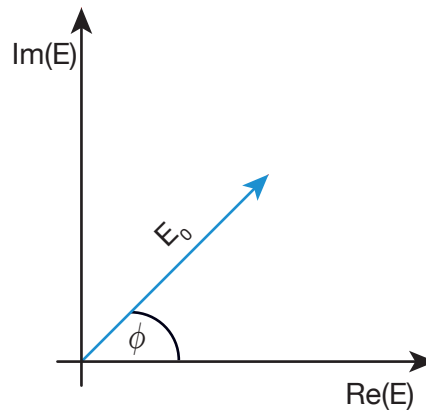


Fig. 2.2 Illustration of the unmodulated signal $E(t)$ in the complex plane. On the y-axis the imaginary part of the signal is plotted while on the x-axis the real part of the signal is plotted. The phase angle ϕ of $E(t)$ is the angle of the phasor with respect to the real axis of the signal.

We will now use the phasor picture to illustrate amplitude and phase modulation.

2.2 Amplitude and phase modulation

We now consider amplitude and phase perturbations to the ideal cosine signals, and model them with time-varying $a(t)$ and $\phi(t)$, respectively. We obtain

$$E(t) = E_0[1 + a(t)] \operatorname{Re}[e^{i(\omega_L t + \phi(t))}], \quad (2.8)$$

but continue to switch between the real signal and its complex representation whenever it is convenient. First, we will illustrate how to represent an additional periodic modulation of the amplitude and the phase at one specific frequency in the frequency domain and in the phasor picture.

2.2.1 Amplitude Modulation

We first investigate a periodic modulation of amplitude with $a(t) = m \cos(\omega_m t)$, while $\phi(t) = 0$. We find

$$E_{AM}(t) = E_0[1 + m \cos(\omega_m t)] \cos(\omega_L t) \quad (2.9)$$

$$= E_0 \operatorname{Re}\{e^{i\omega_L t} [1 + \frac{m}{2}(e^{i\omega_m t} + e^{-i\omega_m t})]\}, \quad (2.10)$$

where m is called the amplitude modulation coefficient. The amplitude modulation thus adds two sidebands at detuning ω_m and a power $P_S = (m/2)^2 P_C$ compared to the carrier signal as sketched in Fig. 2.3(a). In the phasor picture, these sidebands are represented by two additional arrows rotating around the arrowhead of the main phasor as sketched in Fig. 2.3(b). The rotation direction is anticlockwise for the blue-detuned frequency component and clockwise for the red detuned frequency component. Since there is no phase difference between the two sidebands, they point in the same direction at $t = 0$.

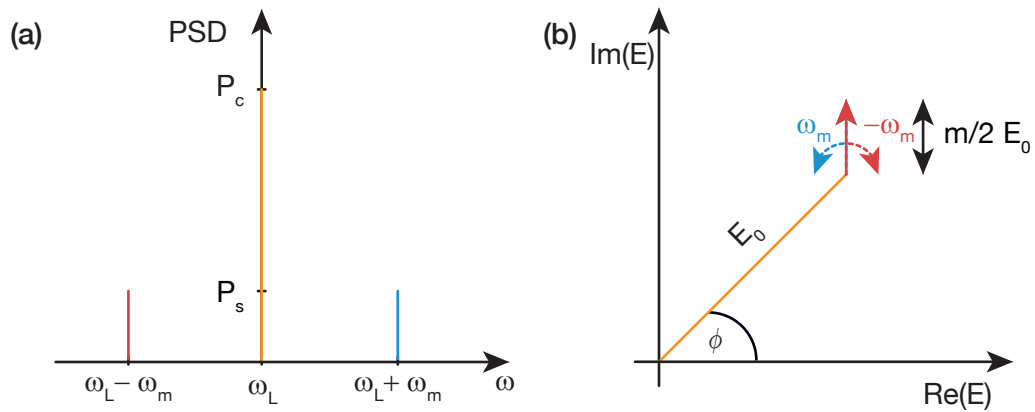


Fig. 2.3 Illustration of the amplitude-modulated signal. (a) Amplitude modulation of the carrier at frequency ω_L . The two sidebands at detuning ω_m have power P_S . (b) The amplitude modulation is represented by phasors rotating around the arrowhead of the main phasor with frequency ω_m in opposite directions (indicated by the dashed arrows) with no phase difference between the two sidebands. The phasors point in the same direction at time $t = 0$ [21].

2.2.2 Phase Modulation

We model sinusoidal phase modulation with $\phi(t) = \beta \sin(\omega_m t)$ and $a(t) = 0$ in Eqn. (2.8) and obtain

$$E_{\text{PM}}(t) = E_0 \cos[\omega_L t + \beta \sin(\omega_m t)] \quad (2.11)$$

$$= E_0 \operatorname{Re}[e^{i\omega_L t} e^{i\beta \sin(\omega_m t)}] \quad (2.12)$$

$$= E_0 \operatorname{Re}[e^{i\omega_L t} J_n(\beta) \sum_{n=-\infty}^{\infty} e^{in\omega_m t}], \quad (2.13)$$

where J_n are Bessel functions. For small phase modulation coefficients $\beta \ll 1$, Eqn. (2.13) transforms to

$$E_{\text{PM}}(t) = E_0 \operatorname{Re}\{e^{i\omega_L t} [1 + \frac{\beta}{2}(e^{i\omega_m t} - e^{-i\omega_m t})]\}. \quad (2.14)$$

The phase modulation adds two sidebands with frequency $\omega_L - \omega_m$ and $\omega_L + \omega_m$ both with power $P_S = (\beta/2)^2 P_C$ to the carrier as illustrated in Fig. 2.4(a). The two sidebands have opposite signs. However, the PSD only shows the absolute value of the sidebands in frequency space, hence the sidebands have the same sign in Fig. 2.4(a). A phase modulation of the carrier of the light at frequency ω_L can therefore be seen as additional modulation arrows on the carrier arrow. The red- and blue-detuned modulation arrows oscillate clock- and anticlockwise around the carrier. However, the components corresponding to the arrows have opposite signs and therefore point in opposite directions due to their phase difference of $\Delta\phi = \pi$, as illustrated in Fig. 2.4(b).

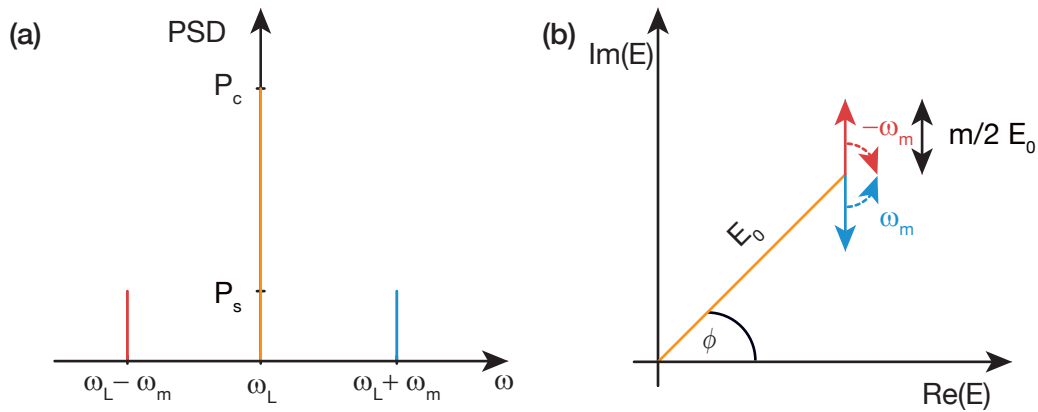


Fig. 2.4 Illustration of the phase-modulation of a signal. (a) Phase-modulation of the carrier at frequency ω_L . The two sidebands at detuning ω_m with power P_S have opposite signs. (b) The phase modulation is represented by phasors rotating around the arrowhead of the main phasor with frequency ω_m in opposite directions (indicated by the dashed lines). The phasors always point in opposite direction. [21].

Any real noise process can neither be described exclusively by amplitude noise nor by phase noise, but is a superposition of both. A noise process will typically also not have one frequency component only. However, using a model where noise is only represented by a single frequency component is a good starting point for our discussion about noise on a periodic test signal.

Starting with the description obtained from Eqn. (2.10) and Eqn. (2.14) one has four sidebands with different frequencies. The amplitude and phase modulation sidebands from Fig. 2.3 and Fig. 2.4 have an angle ψ in between them for illustration purposes as sketched in Fig. 2.5.

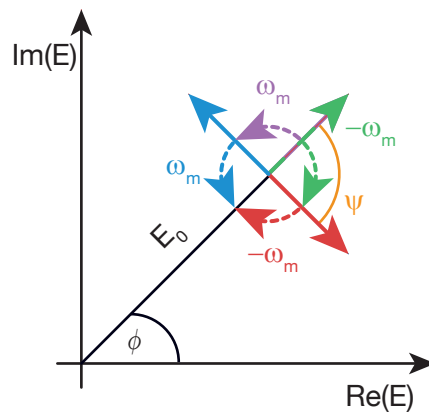


Fig. 2.5 Superposition of the four phasors from both amplitude and phase modulation. The phase modulation sidebands are displayed in blue and red while the amplitude modulation sidebands are displayed in purple and green. The angle $\psi = \pi/2$ gives the angle between phase and amplitude modulation [21].

One can superpose the four sidebands from these equations. There are two sidebands with the same frequency (both for positive modulation frequency and negative modulation frequency). Their phasors with possibly different amplitude rotate in the same direction and can therefore be superposed. That means that from the four initial sidebands from amplitude and phase rotation we can extract two effective phasors rotating around the main phasor arrowhead as shown in Fig. 2.6(a). The angle between the former amplitude and phase modulation is now the angle between the combined amplitude and phase modulation vectors.

The two phasors obtained by superposition of the amplitude and phase modulation phasors can be further transformed, by rewriting

$$E_{\text{AM+PM}}(t) = \text{Re}(E_c e^{i\omega_L t} + E_n [e^{i((\omega_L + \omega_m)t + \psi)} + e^{i(\omega_L - \omega_m)t}]) \quad (2.15)$$

$$= \text{Re}(E_c e^{i\omega_L t} + E_n e^{i(\omega_L + \psi/2)} [e^{i(\omega_m t + \psi/2)} + e^{-i(\omega_m t + \psi/2)}]) \quad (2.16)$$

$$= \text{Re}(E_c e^{i\omega_L t} + 2E_n e^{i(\omega_L + \psi/2)} \cos(\omega_m t + \psi/2)). \quad (2.17)$$

With this formula, combined amplitude- and phase-modulation can be seen as one amplitude-modulated phasor instead of initially four single phasors oscillating around the head of the carrier. The projection of the resulting vector on the real or imaginary axis is dependent on the phase $\psi/2$. A projection of the modulation arrow onto the imaginary axis corresponds to a pure phase modulation process and the projection of the modulation arrow onto the real axis corresponds to a pure amplitude modulation process. That is why the angle ψ represents the ratio of phase modulation to amplitude modulation. An illustration of this line of thought can be seen in Fig. 2.6(b).

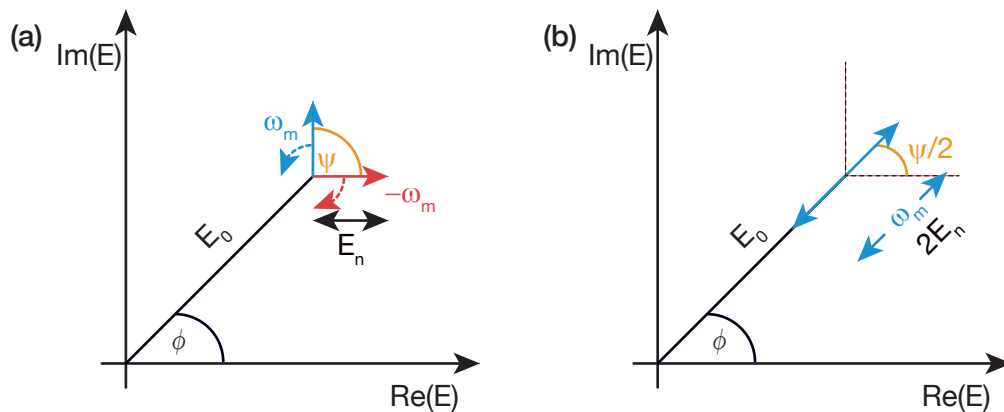


Fig. 2.6 Illustration of both amplitude and phase noise on a system. (a) Modulated light as described in Eqn. (2.15) which is exemplified by two sidebands oscillating with ω_m in the oscillating frame and a phase angle ψ in between them. (b) A noise process as shown in Fig. (a) can be transformed to a modulation of one (instead of two) sideband phasor, where only the amplitude is modulated with frequency ω_m and with angle $\psi/2$ between the transformed phasor and the real axis [21].

No real noise process that could possibly alter the laser's frequency characteristics only consists of a pure amplitude/phase modulation at a single frequency. Noise processes characteristically have multiple frequency components with different amplitude coefficients (possibly both amplitude- and phase-modulated). These processes can be illustrated by multiple vectors corresponding to different frequency components with different amplitudes oscillating around the phasor of the carrier. The multiple vector components will add up and give an instantaneous effective modulation.

The phasor models for amplitude and phase noise modulation allows us to analyze the

phase noise properties of electric fields also oscillating at radio frequencies. Let's assume we have a both amplitude and phase modulated test signal V_{test} oscillating at frequencies ω_L with sidebands ω_m . We compare the test signal with a reference signal V_{ref} which is not modulated but has the same frequency as the test signal. Typical radio-frequency mixers can detect the instantaneous difference frequency between the test signal and the reference signal, which corresponds to the phase and amplitude noise of the test signal since the frequencies of both signals are equal. A spectrum analyzer (SA) or fast fourier transform (FFT) analyzer can now detect the real part of the power spectral density of the signal corresponding to the amplitude (phase) modulation if the reference signal is in (out of) phase with the test signal. By measuring both the amplitude and the phase modulation spectrum we can determine ψ . This general technique can be applied to both radio frequency and optical signals. We will analyze the noise generated by a fiber on a light signal in Chapter 5.

The phasor picture developed in this Section can also account for single-frequency modulations of a periodic signal as we encounter it in an acousto-optic-modulator (see Chap. 5) or in an electro-optic-modulator (see Chap. 8). However, if a noise signal contains multiple frequency components, the phasor picture becomes complex and does not give further insights. Thus, we now model noise processes on a periodic signal with noise power spectral densities.

2.3 More General Noise Processes

The relation shown in Eqn. (2.6) between the power spectral density of a periodic modulation can also be used to characterize a noise spectral density, by applying the same formalism to arbitrary modulation functions $a(t)$ and $\phi(t)$.

For instance, phase noise processes on a periodic signal are characterized by the power spectral density

$$S_{\phi\phi}(f) = \int_{-\infty}^{\infty} G_{\phi\phi}(\tau) e^{-i2\pi f\tau} d\tau, \quad (2.18)$$

where $G_{\phi\phi}(\tau) = \langle \phi^*(t)\phi(t+\tau) \rangle$ is the autocorrelation function of the phase noise process $\phi(t)$.

Many phase noise processes follow simple power laws as shown in Ref. [22]. As a simple model we write the double-sided power spectral density $S_{\phi\phi}$ as

$$S_{\phi\phi}(f) = \sum_{i=0}^{-4} b_i f^i, \quad (2.19)$$

where each of the summands has a different power law behavior.

The phase noise signal $\phi(t)$ is related to the angular frequency noise signal $\omega(t)$ via the time derivative

$$\omega(t) = \frac{d\phi(t)}{dt}. \quad (2.20)$$

By Fourier transforming this relation we obtain

$$\Omega(f) = 2\pi i f \Phi(f), \quad (2.21)$$

where $\Omega = \mathcal{F}[\omega]$ corresponds to the Fourier transform of the angular frequency signal and $\Phi = \mathcal{F}[\phi]$ corresponds to the Fourier transform of the phase signal. Using this result we can also relate the angular frequency noise PSD to the phase noise PSD as [23]

$$S_{\omega\omega}(f) = 4\pi^2 f^2 S_{\phi\phi}(f) = 4\pi^2 \sum_{j=2}^{-2} b_j f^j. \quad (2.22)$$

The commonly used names for the different phase noise types as well as their power-law exponents in Eqn. (2.19) (for the exponent i) and Eqn. (2.22) (for the exponent j) are listed in Tab. 2.1.

Exp. i of $S_{\phi\phi}(f)$	Exp. j of $S_{\omega\omega}(f)$	Name of noise process	Color of noise
0	2	White phase noise	white
-1	1	Flicker phase noise	pink
-2	0	White frequency noise	brown
-3	-1	Flicker frequency noise	blue
-4	-2	Random walk frequency noise	violet

Tab. 2.1 The columns in this table describe (i) the exponents of the phase noise summands $b_i f^i$; (ii) the exponents of the frequency noise summands proportional to $b_j f^j$; (iii) common names of different noise processes; (iv) the commonly attributed colors to the noise processes.

White phase noise is independent of Fourier frequency, i.e. it contains all frequency components with equal magnitude. For all other types of noise, the magnitude of noise decreases with a power law in frequency as shown in Tab. 2.1.

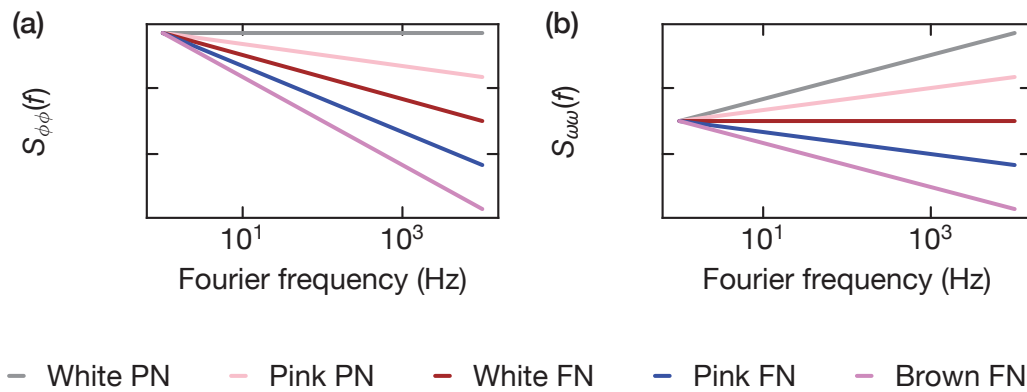


Fig. 2.7 Plot of the different power law behaviour of a noise source as given in Eqn. (2.19) for the phase noise spectrum $S_{\phi\phi}(f)$ and the frequency noise spectrum $S_{\omega\omega}(f)$. (a) This figure describes the phase noise spectrum $S_{\phi\phi}(f)$ plotted against Fourier frequencies on a double-logarithmic scale. The white phase noise process [colored in both (a) and (b) in grey] is flat for all frequencies. The other noise processes have a negative slope as it is given in Tab. 2.1. The color scheme resembles their name in the table. (b) This figure illustrates the frequency noise spectrum $S_{\omega\omega}(f)$, which can be derived from (a) using Eqn. (2.20), plotted on a double-logarithmic graph against frequencies. A white phase noise process in this plot has a slope of 2. The slopes of the other noise processes are given in Tab. 2.1.

The exponents of the noise processes from Fig. 2.7 shift by +2 whether one looks at the frequency noise spectral density or at the phase noise spectral density.

We now apply these concepts to a laser. For simplicity, we assume that the laser is linearly polarized. Therefore approximating the electric field of the laser with $E(t)$ from Eqn. (2.1) is valid. However, no laser is ideal in the sense of oscillating at one single frequency ω_L and without amplitude noise. Thus, the model of amplitude and phase noise made in Sec. 2.2 is a better approximation. In Sec. 2.5.1, we present a discussion of the influence of noise processes on a laser's line shape.

2.4 Theory of a Laser

Lasers are quantum devices which use the energy difference between two levels spaced in energy by $E_L = \hbar\omega_L$ to send out light at frequency ω_L . The functionality of lasers is described in detail in Ref. [24] and Ref. [25]. To understand how stimulated emission of an electric field from a laser comes about, we first need to understand how radiation processes in a two system can be modeled.

2.4.1 Planck's Law of Radiation

Planck's law of radiation describes the mean energy density of radiation in thermal equilibrium with a black body. To derive it we start by looking at the the Maxwell equation

$$\nabla \cdot \mathbf{E}(\mathbf{r}, t) = 0, \quad (2.23)$$

where $\mathbf{E}(\mathbf{r}, t)$ is the electric field vector. The Maxwell equation implies that the electric field is time dependent but does not depend on the position. Hence the electric field is proportional to $e^{i\omega t}$, where ω is the angular frequency. Since the electric field is assumed to be periodic, it also fulfills the Helmholtz equation

$$\nabla^2 \mathbf{E}(\mathbf{r}, t) = \frac{1}{c^2} \frac{d^2 \mathbf{E}(\mathbf{r}, t)}{dt^2}. \quad (2.24)$$

A solution of the electric field which fulfills both the Maxwell and the Helmholtz equation is given by

$$E(\mathbf{r}, t) = E_0 \operatorname{Re}[e^{i(\omega t + \mathbf{k} \cdot \mathbf{r})}], \quad (2.25)$$

where $\phi = \mathbf{k} \cdot \mathbf{r}$ describes the spatial phase of the electric field. Plugging this solution into the Helmholtz equation gives the relation between the wave vector \mathbf{k} and the frequency of the electric field as

$$i^2 E_0 \begin{pmatrix} k_x^2 \\ k_y^2 \\ k_z^2 \end{pmatrix} = \frac{i^2}{c^2} \omega^2 E_0 \begin{pmatrix} 1 \\ 1 \\ 1 \end{pmatrix}. \quad (2.26)$$

Hence, the wave vectors are uniform in all spatial directions and the dispersion relation $\omega = ck$ holds.

Using Planck's law, one can give an expression for the electromagnetic radiation inside a cavity [25]. The electric field must vanish at the surfaces of the cavity. The cavity is assumed to be cubic, where each edge has length L leading to periodic boundary conditions on the three-component periodic signal

$$E_x(\mathbf{r}, t) = E_x(t) \cos(k_x x) \sin(k_y y) \sin(k_z z), \quad (2.27)$$

$$E_y(\mathbf{r}, t) = E_y(t) \sin(k_x x) \cos(k_y y) \sin(k_z z), \quad (2.28)$$

$$E_z(\mathbf{r}, t) = E_z(t) \cos(k_x x) \sin(k_y y) \cos(k_z z), \quad (2.29)$$

where the wave vector \mathbf{k} limits the number of allowed modes in the cavity. A formulation of the electric field in this way satisfies the Helmholtz equation from Eqn. (2.24) since it is a periodic signal and also the boundary conditions if the components of \mathbf{k} fulfill

$$\mathbf{k} = \left(\frac{\pi l}{L}, \frac{\pi m}{L}, \frac{\pi n}{L} \right), \quad (2.30)$$

where l , m and n are integers. The solution for the electric field in Eqns. (2.27) - (2.29) also satisfies the Maxwell equation from Eqn. (2.23) if \mathbf{k} is perpendicular to $\mathbf{E}(t)$.

To derive Planck's law of radiation we need an expression for the number of field modes for a given energy. A frequency interval in the cavity corresponds via the dispersion relation of an electromagnetic wave in vacuum

$$\omega + d\omega = ck + c dk, \quad (2.31)$$

to the absolute value of the electric field vector k and the speed of light c . Since we are looking for the number of modes per frequency interval, we are only interested in the absolute value of the wave vector $k = |\mathbf{k}| = \sqrt{k_x^2 + k_y^2 + k_z^2}$. Therefore, we can limit our discussion to the cavity cube in the octant where k_x , k_y and k_z are positive. The number of modes in a spherical shell between k and $k + dk$ is obtained by integrating over the surface of the spherical shell in the first octant. By adding a factor 2 for the two possible polarizations of the light we get the the number of modes in the cavity

$$n_{\text{modes}} = \frac{2}{8} \frac{4\pi k^2 dk}{(\pi/L)^3}. \quad (2.32)$$

For our further derivations we are interested in the field mode density, i.e. we want to divide out the cavity volume from Eqn. (2.32) and we use the dispersion relation $\omega = ck$. Therefore Eqn. (2.32) transforms to the density of field modes

$$p(\omega)d\omega = \frac{\omega^2 d\omega}{\pi^2 c^3}. \quad (2.33)$$

After arriving at an expression for the number of modes per frequency interval we would like to find an expression for the number of photons per mode.

Reference [24] gives an approach to derive this result. First, we consider photons carrying energy $E_{\text{ph}} = \hbar\omega_{\text{ph}}$. The probability distribution for n photons with energy $E = \hbar\omega$ is proportional to the Boltzmann factor $\exp(-n\hbar\omega/k_B T)$ as the photons are in thermal equilibrium with a black body radiator at temperature T . This corresponds to the probability of a state with energy nE_{ph} in a canonical ensemble with the energy of the system being $\sum_{n=0}^{\infty} e^{-n\hbar\omega_{\text{ph}}/k_B T}$. The mean number \bar{n} of photons at frequency ω_{ph} is then given by

$$\bar{n} = \frac{\sum_{n=0}^{\infty} n e^{-n\hbar\omega_{\text{ph}}/k_B T}}{\sum_{n=0}^{\infty} e^{-n\hbar\omega_{\text{ph}}/k_B T}} = \frac{1}{e^{\hbar\omega_{\text{ph}}/k_B T} - 1}, \quad (2.34)$$

where the second part of the equation is evaluated using a geometric series.

Finally, we can combine the number of modes per frequency interval from Eqn. (2.33), the number of photons per mode from Eqn. (2.34), and the energy per photon $E_{\text{ph}} = \hbar\omega$ to obtain the energy spectral density of electromagnetic radiation

$$W(\omega)d\omega = \frac{\hbar\omega^3}{\pi^2c^3} \frac{1}{\exp(\hbar\omega/k_B T) - 1} d\omega, \quad (2.35)$$

where ω describe the Fourier frequencies, \hbar is the reduced Planck constant, k_B is the Boltzmann constant and T corresponds to the temperature of the black body emitting electromagnetic radiation. This equation, which is called Planck's law of radiation, gives us a tool to describe a radiative process inside a cavity between a system which can provide for photons and a thermal bath and the system itself.

2.4.2 Einstein's Coefficients Describing a Laser

A two level system of atoms in a ground and an excited state, where photons can mediate a transition between the two states can be modeled with the theory of Einstein coefficients. To understand the theory of Einstein coefficients we first want to consider a two level system inside a cavity, which consists of an excited state $|2\rangle$ and a ground state $|1\rangle$ with population numbers N_2 and N_1 , respectively. In our simplified approach the two levels are non-degenerate. We allow for an external electric field to enter the system. The total spectral density of electromagnetic radiation from the excited state to the ground state is then

$$W_{\text{total}}(\omega) = W_{\text{planck}}(\omega) + W_{\text{external}}(\omega) \quad (2.36)$$

which consists of a summand which assumes that the cavity is a black body and a summand caused by the external electric field.

Transitions in the two level system can only occur if one of the following three processes happens (as illustrated in Fig. 2.8):

- (a) **Spontaneous emission:** A spontaneous emission process is illustrated in Fig. 2.8(a). An atom in the excited state emits a photon with rate A_{21} into the full solid angle. The frequency of the light from this process is given by the energy level difference between the two levels $\Delta E = \hbar\omega$. The change in population of the excited state

$$\frac{dN_2}{dt} = -A_{21}N_2, \quad (2.37)$$

is only dependent on the rate A_{21} and the population of the excited state N_2 .

- (b) **Absorption:** An absorption process can happen when a radiative field with frequency $\omega = \Delta E/\hbar$ is incident on the atom. An excited atom can transit from the

ground state to the excited state. The process will happen with rate $B_{12}W_{\text{total}(\omega)}$. Therefore the absorption process leads to a rate equation for the excited state

$$\frac{dN_2}{dt} = +B_{12}N_1W_{\text{total}(\omega)}, \quad (2.38)$$

which is dependent on the population of the ground state N_1 .

- (c) **Stimulated Emission:** The presence of radiation can also enhance the emission of photons from the two level system. If an atom is in the excited state and a photon with wave vector k , frequency ω , and a specific polarization is incident on the atom, the atom can emit photons with rate $B_{21}\langle W_{\text{total}(\omega)} \rangle$. The emitted photons have the same wave vector k , frequency ω , and the same polarization as the incident photons. In addition, the emitted light also has the same phase as the incident light. The stimulated emission process gives a rate equation for the excited state

$$\frac{dN_2}{dt} = -B_{21}N_2W_{\text{total}(\omega)}, \quad (2.39)$$

which is dependent on the population of the excited state N_2 .

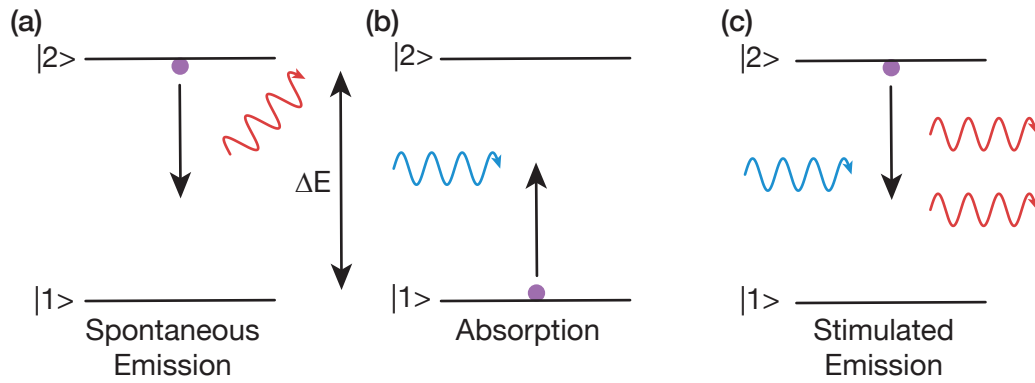


Fig. 2.8 Illustration of transition processes in a two level system consisting of the non degenerate ground state $|1\rangle$ and excited state $|2\rangle$ with number populations N_1 and N_2 , respectively. Incident photons are blue and outgoing photons are red. The black arrow denotes the direction of transition. (a) An atom occupying the excited state $|2\rangle$ emits a photon with wavelength $\omega_L = \Delta E$. The direction of emission for the photon is equal over the full solid angle. (b) An atom occupying the ground state $|1\rangle$ transits from the ground state to the excited if it can absorb a photon with a frequency $\omega_L = \Delta E$. (c) A Photon absorbed by an atom in the excited state $|2\rangle$ stimulates the emission of another photon with the same wave vector k , polarization and phase.

If we can make sure that a steady-state population inversion exists in the system, i.e. $N_2/N_1 > 1$, then a continuous stimulated emission in this system can take place, which allows us to build a laser based on such a system.

However, the model of a simple two level system is not sufficient to describe a population inversion in a laser. For a population inversion we need to add a second excited state $|3\rangle$ with a higher energy than the first excited state $|2\rangle$ to our model. A pump excites atoms to the second excited state $|3\rangle$. The atoms decay from the second excited state $|3\rangle$ to the first excited state $|2\rangle$. With the correct choice of the Einstein coefficients A_{21} , B_{21} and B_{12} we can achieve a population inversion of the first excited state $|2\rangle$ compared to the ground state [25]. Stimulated emission from the excited state is generated by reflecting photons from two mirrors the active region. This ingredient of our laser is called the laser-cavity.

The total transition rate from the excited state to the ground state for stimulated emission is described in Eqn. (2.39). We now want to look at the frequency distribution of this transition. The stimulated emission produces phase stable photons with the same polarization, wave vector and frequency as the incoming atom and we assume the laser to be in a steady state in the lasing condition. This means that we assume that there are constantly photons stimulating the two level system, but the photons emitted from the system stay coherent. A fully coherent output is an idealized approach to think about the laser system. For narrow spectral distributions of the energy spectral density $W_{\text{total}}(\omega)$ the output of the the stimulated emission spectra can be modeled by

$$\frac{dN_2}{dt} = -B_{21}N_2 \int g(\omega)W_{\text{total}}d\omega, \quad (2.40)$$

where the line shape function $g(\omega)$ is a normalized function representing any broadening mechanism on the light and $W_{\text{total}}(\omega)$ is assumed to be Dirac-Delta-distributed in frequency space since it is spectrally more narrow than the line shape function $g(\omega)$.

In the next Section we will discuss about which noise processes can broaden the spectrum of a laser and therefore change the spectral emission characteristics of a laser. As a starting point we assume that the laser radiation is almost monochromatic. However, we will modulate phase noise onto the laser which will broaden the line shape of the laser. The laser under investigation will be linearly polarized, such that the electric field is

$$E(t) = E_0 \text{Re}[e^{i(\omega_L t + \phi(t)}], \quad (2.41)$$

where $\phi(t)$ is the time-dependent phase noise on the system which will be characterized in the next Section.

2.5 Noise Processes on a Laser

Phase noise can significantly broaden the line shape of a monochromatic laser.

We will characterize the phase noise by low-pass-filtered white frequency noise, which is described by a flat angular frequency power spectral density as shown in Fig. 2.7. The low-pass-filtered white frequency noise can be expressed as

$$S_{\omega\omega}(f) = b_0 f^0 = b_0; f \ll f_c, \quad (2.42)$$

$$S_{\omega\omega}(f) = 0; f \gg f_c, \quad (2.43)$$

which is constant up to the cutoff frequency f_c , but vanishes for frequencies $f \gg f_c$.

Using this definition of frequency noise to model the phase noise $\phi(t)$ of the laser, we can develop a formalism to calculate the line shape function $g(\omega)$ for a given cutoff frequency f_c . With this model we will be able to explain both Gaussian and Lorentzian line shapes of a laser [26–28].

2.5.1 Formalism to Understand Line Shapes from Noise Processes

Assuming the model given in Eqn. (2.41) we calculate the autocorrelation function of this signal as

$$G_{EE}(\tau) = \langle E(t)E(t + \tau) \rangle \quad (2.44)$$

$$= E_0^2 \exp(i\omega_L \tau) \langle \exp\{i[\phi(t) - \phi(t + \tau)]\} \rangle \quad (2.45)$$

$$= E_0^2 \exp(i\omega_L \tau) \exp\left\{-\frac{1}{2} \langle [\phi(t) - \phi(t + \tau)]^2 \rangle\right\}. \quad (2.46)$$

In the last line the Gaussian moment theorem for the Gaussian process $\phi(t)$ was applied, which ensures that the odd moments of the Gaussian process vanish [27].

References [27, 28] expand $\langle [\phi(t) - \phi(t + \tau)]^2 \rangle$ further to eventually obtain the autocorrelation function

$$G_{EE}(\tau) = E_0^2 \exp(i\omega_L \tau) \exp\left[-2 \int_0^\infty S_{\omega\omega}(f) \frac{\sin^2(f\tau)}{f^2} df\right]. \quad (2.47)$$

This autocorrelation function can be Fourier-transformed to obtain the power spectral density of the electric field

$$S_{EE}(f) = 2 \int_{-\infty}^{\infty} \exp(-i2\pi f\tau) G_{EE}(\tau) d\tau. \quad (2.48)$$

This power spectral density of the electric field can be used to derive the line shape of a laser. If we plug in the noise spectral density $S_{\omega\omega}(f)$ into Eqn. (2.47), we obtain the autocorrelation function

$$G_{EE}(\tau) = E_0^2 e^{(i\omega_L \tau)} e^{-2\frac{b_0}{f_c} [\sin^2(\pi f_c \tau) - \pi f_c \tau \int_0^{2\pi f_c \tau} 2\pi f_c \tau]}. \quad (2.49)$$

Unfortunately, this integral is not easy to Fourier-transform analytically. However, there are two limits in which we can Fourier-transform the autocorrelation function to obtain the power spectral density of the signal.

2.5.2 Lorentzian Line Shape of a Laser

If we approximate the frequency noise power spectral density $S_{\omega\omega}(f)$ to be flat over the full frequency space, i.e. the cut off frequency $f_c \rightarrow \infty$, we obtain a Lorentzian power spectral density

$$S_{EE}^L(f) = |E_0|^2 \frac{b_0}{(\pi b_0/2)^2 + (f - f_0)^2}, \quad (2.50)$$

when applying the Wiener-Khinchin theorem to the autocorrelation function in Eqn. (2.49). The full width half maximum of this Lorentzian is $\text{FWHM} = \pi b_0$. Therefore the power spectral density of a process which is flat in frequency space will lead to a Lorentzian spectrum. Figure 2.9(a) shows the white frequency spectrum with the scaling factor b_0 . The shape of the Lorentzian function is shown in Fig. 2.9(b). Here one can see that the wings of the Lorentzian function are fairly prominent compared to the resonance, especially if we later compare the Lorentzian function to the Gaussian function.

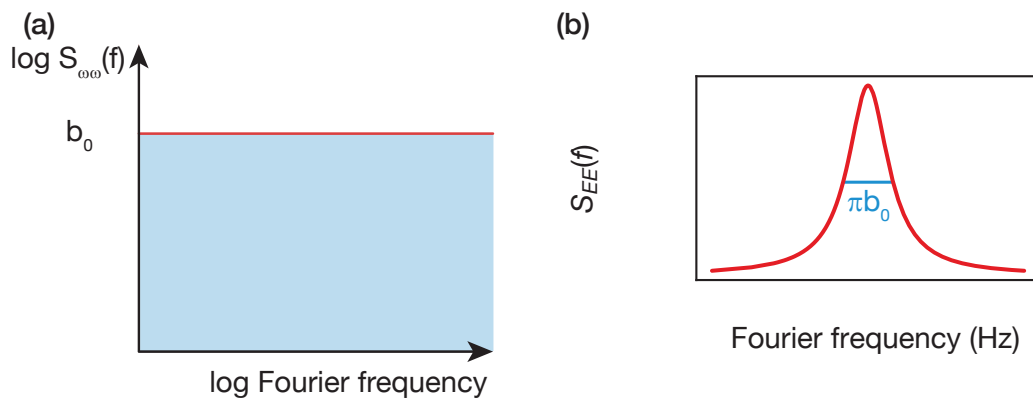


Fig. 2.9 Illustration of a Lorentzian power spectral density of the electric field caused by a flat frequency noise spectrum. (a) The frequency noise power spectral density $S_{\omega\omega}$ is plotted against the Fourier frequency. The white frequency noise in this plot is flat in frequency space with the scaling factor b_0 . The blue shaded area indicates how much integrated frequency noise is incident on the laser. (b) The power spectral density of the electric field has a Lorentzian line shape if $\phi(t)$ is a Gaussian noise process. The full width half maximum value of the Lorentzian function is given by πb_0 .

We chose the approach from Eqn. (2.49) to find a general function for a white frequency noise process to derive the Lorentzian line shape of the electric field. However, there is also a more intuitive approach to derive the Lorentzian line shape of the laser [26]. Assuming that the mean phase jitter $\langle \Delta\phi^2(\tau) \rangle = \langle [\phi(t) - \phi(t + \tau)]^2 \rangle$ is a stationary Gaussian process and therefore is normally distributed, we can assume the phase jitter

$$\langle \Delta\phi^2(\tau) \rangle = \frac{\pi b_0}{2} |\tau| \quad (2.51)$$

to be proportional to the time delay. This corresponds to Brownian motion, where the variance of the phase (the phase jitter) increases linearly with time. Using Eqn. (2.51), we can compute the power spectral density of the signal as the Fourier transform of the autocorrelation function

$$G_{EE}(\tau) = |E|^2 e^{-\frac{1}{2} \langle \Delta\phi(\tau)^2 \rangle} e^{i\omega_L \tau} = |E|^2 e^{-\pi b_0/2 |\tau|} e^{i\omega_L \tau}. \quad (2.52)$$

The result of this transformation gives the Lorentzian line shape from Eqn. (2.50) again. A Lorentzian line shape of a laser is therefore obtained if the frequency noise on the laser is constant over all frequencies.

2.5.3 Gaussian Line Shape of a Laser

If we approximate the frequency noise power spectral density $S_{\omega\omega}(f)$ to have only very low-frequency components, i.e. $f_c \rightarrow 0$, applying the Wiener-Khinchin theorem to Eqn. (2.44) will give a Gaussian line shape of the spectrum

$$S_{EE}^G(f) = |E_0|^2 \left(\frac{2}{\pi b_0 f_c} \right)^{1/2} \exp \left[-\frac{(f - f_0)^2}{2 b_0 f_c} \right]. \quad (2.53)$$

The full width half maximum of this Gaussian is $\text{FWHM} = 2\sqrt{2 \ln(2) b_0 f_c}$.

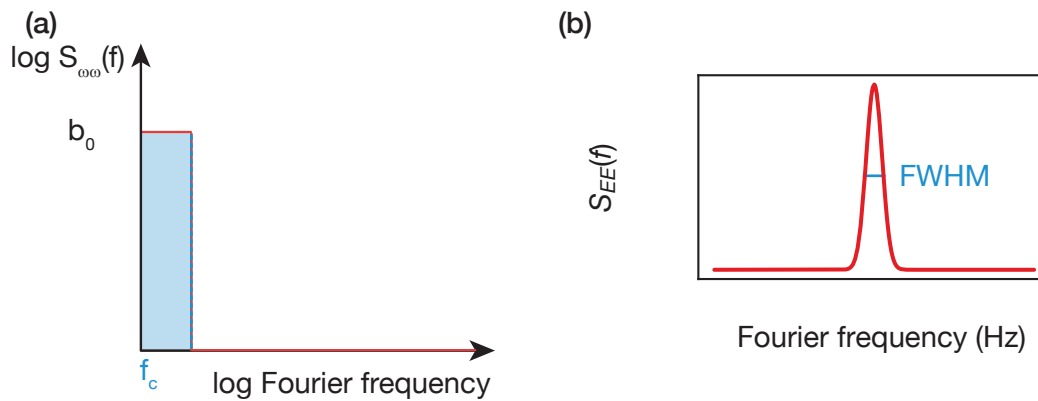


Fig. 2.10 Illustration of a Gaussian spectrum of the electric field caused by a low pass filtered flat frequency noise spectrum. (a) The frequency noise spectrum $S_{\omega\omega}$ is plotted against the Fourier frequency. The white frequency noise in this plot is flat in frequency space with the scaling factor b_0 up to the cutoff frequency f_c . The blue shaded area shows the integrated phase noise. (b) The power spectral density of the electric field has a Gaussian line shape if $\phi(t)$ exhibits the noise properties from Fig. (a). The full width half maximum value of the Gaussian function is $2\sqrt{2\ln(2)}b_0f_c$.

An important remark to make is that the Lorentzian and Gaussian line shape functions $S_{EE}^{L/G}(f)$ are not easily comparable even though their definitions contain the same coefficients. However, the coefficient b_0 in Eqn. (2.50) must be related to the integrated frequency noise spectrum over all frequencies whereas for the Gaussian function the scaling factor b_0 is related to the cutoff frequency f_c and therefore leads to a much smaller integrated frequency noise.

After deriving the two analytic limits of line shapes that can be obtained from white frequency noise on the phase $\phi(t)$ of the laser, we want to discuss in the next Section how the line shape results derived in this Section can be connected to the noise properties of a real laser.

2.5.4 Discussion of Line Shapes in Real Lasers

White frequency noise in a laser can be attributed to the spontaneous emission of light of excited state of the laser system as described in Eqn. (2.37). A spontaneous emission event emits a photon with a certain energy $E_{sp} = \hbar\omega_{sp}$ at a random time into a random direction. We assume the emission of a photon to be a white frequency noise process. Therefore the linewidth of the Lorentzian described in Fig. 2.9 has a finite contribution from this process, called the Schawlow-Townes limit [24, 26]. The Schawlow-Townes limit is a fundamental lower limit on the linewidth of a free running laser. However, this white frequency noise can be reduced by active frequency stabilization of the laser [24].

The Gaussian line shape derived in the previous Section [see Eqn. (2.53)] is attributed to low-pass-filtered white frequency noise. Most of the technical noise sources on the laser, i.e. any noise induced by the environment around the laser (acoustic noise, mechanical vibrations, thermal fluctuations), is low-frequency noise. As an approximation one can simulate these noise sources, with the low-pass-filtered white noise from Fig. 2.10(a). Therefore extracting the Gaussian line shape of a laser gives us insight into the technical noise properties of the laser.

Chapter 3

Feedback Theory and Electronics

Low noise properties of a laser can be obtained by active control of its output spectrum. The response time of the control system and the added noise of the control system then determine the phase noise properties of the controlled laser.

In this Chapter we introduce important feedback techniques for stabilizing lasers. To understand how these techniques work, we first need to get familiar with the language of control theory including the Laplace transform. We will take a look at a low-pass filter, which is a very basic example of a linear system. This simple example is going to be very useful for analyzing the bandwidth of our homebuilt photodetectors in Chap. 4 and also for analyzing the temperature behavior of the cavity discussed in Chap. 7. In addition, we will give two examples for electronic feedback loops, which will be used in Chap. 5 as a part of a loop filter of the fiber noise cancellation. We will further explain the feedback system of a phase-locked loop (PLL). This technique transfers the phase stability of one oscillator to another oscillator and is the basis for the fiber noise cancellation technique.

3.1 Control System Basics

We describe a system with a periodic input signal $v_{\text{in}}(t)$ and a periodic output signal $v_{\text{out}}(t)$ by blocks which manipulate the system linearly. Let $g(t)$ model one of the blocks which describe the dynamic evolution of the system. Then the system responds linearly to the input [29]

$$v_{\text{out}}(t) = \int_0^t g(t')v_{\text{in}}(t - t')dt'. \quad (3.1)$$

Since we are interested in the system's reaction to an input signal, it is useful to look at the transfer function of the system, which requires us to introduce the Laplace transform of $g(t)$, called $G(s)$.

3.1.1 Laplace Transform

In Chapter 2 we have introduced the time-domain representation and the power spectral density of a signal. Here, we will introduce a second frequency representation of a signal. The Laplace transformation of a time-domain signal $y(t)$ is defined as

$$Y(s) = \mathcal{L}[y(t)] = \int_{0^-}^{\infty} y(t)e^{-st} dt, \quad (3.2)$$

$$y(t) = \frac{1}{2\pi i} \int_{\sigma-i\infty}^{\sigma+i\infty} Y(s)e^{st} ds, \quad (3.3)$$

where the complex Fourier frequency $s = \sigma + i\omega$ corresponds to the Laplace transformed time and σ is the frequency offset allowing for the treatment of damped oscillations. In the following σ is set to zero, but in general σ has to be chosen to lie to the right of all poles of $Y(s)$. The Laplace transformation is thus a generalization of the Fourier transform. In comparison with the Fourier transformation, which is defined for both negative and positive frequencies, the Laplace transform contains only positive frequency components and can be used to give a frequency representation of damped signals [24].

Similarly to Eqn.(2.22) we can derive the relation

$$\mathcal{L}[d^n y(t)/dt^n] = s^n Y(s), \quad (3.4)$$

which relates the Laplace transform of the derivative of a time domain signal to the time domain signal multiplied with the frequency of the signal [30]. We can now express the transfer function of the linear system block $g(t)$ in the frequency domain as $G(s)$. Laplace-transforming Eqn. (3.1) gives a simple relation for the transfer function

$$G(s) = \frac{V_{\text{out}}(s)}{V_{\text{in}}(s)}. \quad (3.5)$$

Applying the transfer function to a signal gives the signal's response to the transfer function. The transfer function can both change the amplitude and the phase of the signal but it does not change the frequency of a signal.

3.1.2 Low-pass Filter

An electronic low-pass filter of first order, which is shown in Fig. 3.1, consists of a resistor with resistance R and a capacitor with capacitance C . It acts as a frequency discriminator and passes signals with a frequency lower than the cutoff frequency $\omega_0 = 1/RC$ while it damps signals with a frequency higher than the cutoff frequency. We assume that a voltage signal $v_{\text{in}}(t)$ is incident on the low-pass filter and a voltage signal $v_{\text{out}}(t)$ leaves the low-pass filter. Using Ohm's law, the voltage drop between the output and input

voltage

$$v_{\text{out}}(t) - v_{\text{in}}(t) = Ri(t), \quad (3.6)$$

corresponds to a current $i(t)$ multiplied by the resistance of the circuit. The current through the system is connected to the voltage over the capacitor as

$$i(t) = \frac{d[Cv_{\text{out}}(t)]}{dt}. \quad (3.7)$$

Plugging Eqn. (3.6) into Eqn. (3.7), we obtain the time-domain representation of the system

$$\dot{v}_{\text{out}}(t) = -\frac{1}{RC}v_{\text{out}}(t) + \frac{1}{RC}v_{\text{in}}(t). \quad (3.8)$$

The low-pass filter acts as a linear transformation on the input signal in the Laplace domain, i.e. the system has a transfer function $G(s)$.

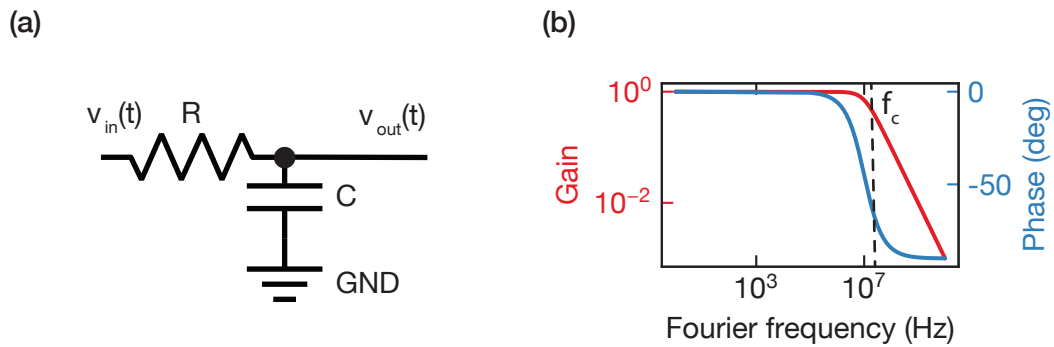


Fig. 3.1 Schematic of an electrical low-pass filter and its transfer function. (a) The low-pass filter consists of a resistor with resistance R and a capacitor with capacitance C to ground. $V_{\text{in}}(t)$ and $V_{\text{out}}(t)$ are the in- and outgoing signals respectively. (b) Bode plot of the transfer function $G(i\omega)$. The gain of the transfer function is plotted in red and has a cutoff frequency f_c . The phase angle of the transfer function is plotted in blue. For low frequencies it is zero, for large frequencies the phase obtains a phase lag of $\arg G(i\omega) = -\pi/2$

Laplace-transforming Eqn. (3.8) gives

$$sY(s) = \omega_0 Y(s) - \omega_0 U(s), \quad (3.9)$$

where $Y(s)$ is the Laplace-transformed output signal and $U(s)$ is the Laplace-transformed input signal. Substituting $s = i\omega$ and solving Eqn. (3.9) for the transfer function of the low-pass filter

$$G(i\omega) = \frac{Y(i\omega)}{U(i\omega)} = \frac{1}{1 + i\omega/\omega_0}, \quad (3.10)$$

lets us express the response of the low-pass filter to arbitrary periodic signals by multi-

plying the signal with the transfer function.

The complex transfer function of a system accounts for both the amplitude and phase transformation of the linear system. The amplitude is defined as the absolute value of the transfer function and the phase is defined as the angle between the imaginary and the real part of the transfer function. Plotting both the amplitude (also called gain response) and the phase response of the system

$$|G(i\omega)| = \frac{1}{\sqrt{1 + \omega^2/\omega_0^2}}, \quad (3.11)$$

$$\arg G(i\omega) = \tan^{-1} \left\{ \frac{\text{Im}[G(i\omega)]}{\text{Re}[G(i\omega)]} \right\} = -\tan^{-1}(\omega/\omega_0), \quad (3.12)$$

on the same frequency axis is called a Bode plot. In Fig. 3.1(b) one can see the Bode plot representation of Eqn. (3.11). The transfer function of the system has unity gain for low frequencies, but its gain is decreased for high frequencies. The characteristic cutoff frequency f_c gives the frequency at which the gain is half the value of the gain for low frequencies. The phase of the output signal is in phase with the input signal for low frequencies and acquires a $-\pi/2$ phase shift for high frequencies, i.e. the output signal gets out of phase with the input signal.

3.2 Feedback Systems

A feedback system can be used to stabilize a output signal to a reference signal. Feedback systems are linear systems, where a change of the output signal $v_{\text{out}}(t)$ at time t directly influences the change of the output signal $v_{\text{out}}(t + \tau)$ at a later time $t + \tau$. The time constant τ describes the characteristic time constant of the system. In the Laplace domain we can describe a feedback system if the output signal $V_{\text{out}}(s)$ of the system with transfer function $G(s)$ is compared with a stable reference signal $V_{\text{ref}}(s)$ in the detector with transfer function $D(s)$. The detector computes a linear error signal from the difference of the reference and the output signal. This error signal gets weighted in the loop filter with transfer function $K(s)$ and then fed back into the modulation port of the system $G(s)$. A schematic of this scheme is shown in Fig. 3.2.

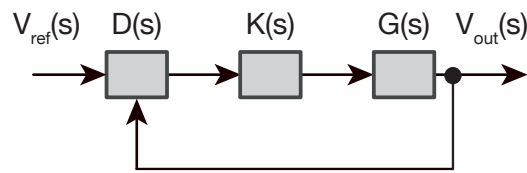


Fig. 3.2 A linear feedback system. The frequency-domain input signal V_{ref} is compared with the output V_{out} of the system $G(s)$ in the detector $D(s)$. The loop filter $K(s)$ gives a weight to the detector output $D(s)$ and feeds the resulting signal to the modulation input of the system $G(s)$.

Using feedback systems we can describe so called active electronic elements - meaning electronic devices which are the source of an electronic signal. Two examples of active electronic circuits are discussed in the following. Both will later be useful to describe the components of a loop filter for a phase-locked loop.

3.2.1 Basic Active Electronic Circuits using Feedback

An elementary part of analog loop filters are operational amplifiers. Using operational amplifiers one can generate a transfer function that suits the stability requirements of a loop filter in the feedback loop. Operational amplifiers are active electronic devices. By adjusting the electronic elements around an operational amplifier we can manipulate the transfer function of operational amplifiers to suit our requirements. In the following, we review the electrical setup of an integrator, which amplifies low frequency components, and a combination of proportional and integral gain. First, we must understand how we can obtain a feedback condition using operational amplifiers.

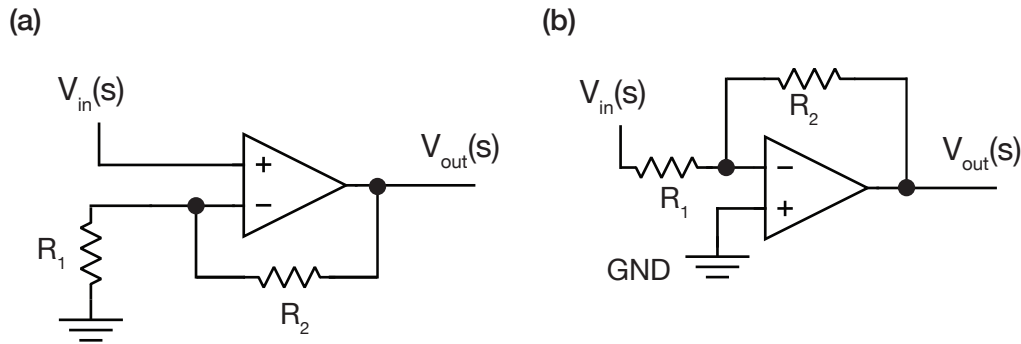


Fig. 3.3 Configurations of operational amplifiers. (a) A non-inverting operational amplifier configuration. (b) An inverting operational amplifier configuration. In both cases the resistances R_1 and R_2 determine the gain of the operational amplifier configuration [31].

The configuration shown in Fig. 3.3(a) is a non-inverting operational amplifier configuration. In this configuration the negative input terminal of the operational amplifier is connected via resistance R_1 to ground and via resistance R_2 to the output of the operational amplifier. The positive input terminal is connected to the input signal. The transfer function of this operational amplifier configuration is [31]

$$G_{\text{non inv}} = 1 + \frac{R_2}{R_1}. \quad (3.13)$$

Looking at Eqn. (3.13) it is clear why the operational amplifier configuration is called non-inverting. The sign of the transfer function of the amplifier is positive and the fraction of R_2 over R_1 determines the gain.

Using operational amplifiers we can also obtain negative gain of an amplifier system. A simple inverting operational amplifier configuration is shown in Fig. 3.3(b). The transfer function of this configuration is [31]

$$G_{\text{inv}} = -\frac{R_2}{R_1}. \quad (3.14)$$

In contrast to the non-inverting configuration the inverting configuration has a transfer function with a negative sign determined only by the fraction of R_2 over R_1 . The transfer function of the two configurations is frequency-independent if we only use purely resistive elements in the two configurations shown in Fig. 3.3.

A operational amplifier feedback system in which the transfer function is frequency independent, i.e. flat in the frequency domain, is called a proportional gain element.

However, especially for loop filters we need frequency dependent feedback loops. To realize this behavior in an electronic circuit, we will use electronic elements with frequency

dependent resistances such as capacitors and inductors. When replacing the resistors R_1 and R_2 of the operational amplifier configurations from above with more complex configurations consisting of resistors, capacitors and inductors, the generalized resistance Z of the replaced configurations determines the transfer function's coefficients. The generalized resistance, also called impedance, is defined for capacitors as

$$Z_L = \frac{1}{i\omega C}, \quad (3.15)$$

and for inductors as

$$Z_L = i\omega L. \quad (3.16)$$

In the following we want to review two different active electronic feedback configurations. The first configuration is an integrator with high gain at low frequencies and low gain at high frequencies. The second configuration is an proportional element with an integral element. Additionally this configuration has a gain limiter for low frequencies. We will understand in Chap. 5 how both feedback loops can be used in a loop filter.

3.2.2 Integral Gain

An operational amplifier in integrator configuration is shown in Fig. 3.4(a).

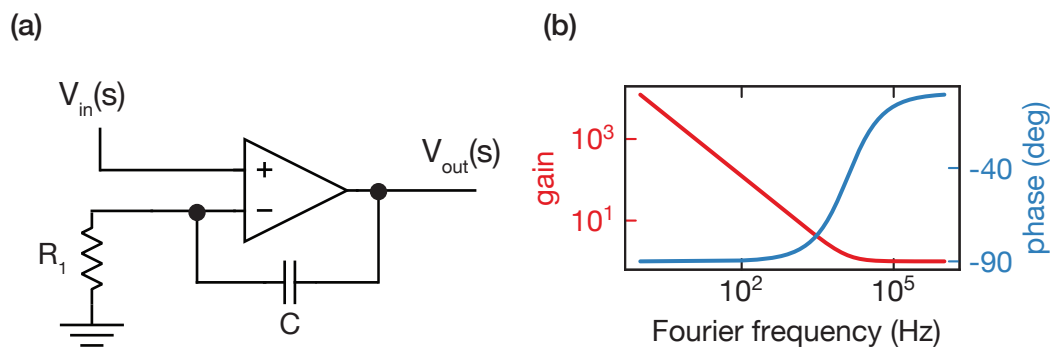


Fig. 3.4 Operational amplifier in integrator configuration. (a) The operational amplifier in non-inverting configuration has a feedback impedance consisting of the capacitor C . The feedback impedance and the resistor R_3 determine the gain of the operational amplifier. (b) A Bode plot of the integrator described in (a). On the x-axis the Fourier frequency of the signal is displayed. The red curve shows the gain of the integrator on a logarithmic y-axis. The blue curve shows the phase lag induced by the integrator on a linear y-axis in degrees. The values taken for this plot are: $R_1 = 10 \text{ k}\Omega$ and $C = 1 \text{ nF}$

The operational amplifier configuration is non-inverting. Hence, its transfer function is

defined as in Eqn. (3.13). The feedback impedance consists of a capacitor with capacitance C . The closed loop gain of the integrator is therefore given by

$$G(i\omega) = 1 + \frac{1/(i\omega C)}{R_1}. \quad (3.17)$$

In the limit of low frequencies the term $1/\omega C$ will diverge and in the limit of high frequencies this term will vanish. Therefore also the gain will diverge for low frequencies, while it will be at the stable value $|G(i\omega)| = 1$ for high frequencies. A detailed analysis of the transfer function of the integrator can be found in the Bode plot in Fig. 3.4(b). The low and high frequency values of the gain correspond to the approximations from above. In the plot one can see that the phase lag of the loop filter on the output signal v_{in} is 90° for small frequencies. The low frequency components are amplified significantly. For high frequencies the phase lag tends to 0° and the gain is unity, which means that the output signal is in phase with the input signal and is not amplified.

3.2.3 A Combination of a Proportional Element with an Integrator

A negative feedback condition can be obtained by using an inverting operational amplifier configuration as described in Fig. 3.3(b). From Eqn. (3.14) we can see that the transfer function in this configuration has a negative sign.

A schematic of a proportional element with the characteristics described can be found in Fig. 3.5(a).

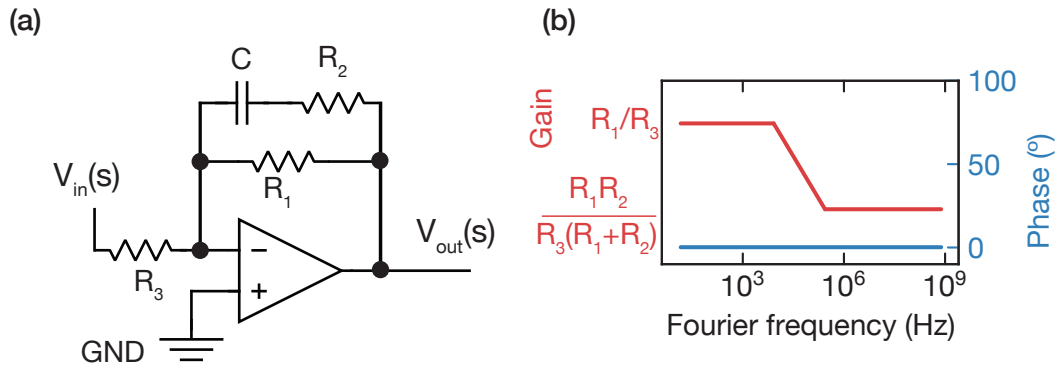


Fig. 3.5 Operational amplifier in proportional gain configuration. (a) The operational amplifier in inverting configuration has a feedback impedance consisting of the resistors R_1 , R_2 and the capacitor C . The feedback impedance together with the resistor R_1 determines the gain of the operational amplifier. (b) A Bode plot of the proportional feedback loop described in (a). On the x-axis the frequency of the signal is displayed. The red curve shows the gain of the proportional element on a logarithmic y-axis. The blue curve shows the phase lag induced by the proportional element on a linear y-axis in degrees. The plot is a sketch of the transfer function. For small Fourier frequencies we expect an amplification as described in Eqn. (3.20), for high Fourier frequencies we expect a gain as in Eqn. (3.21).

The feedback impedance of the proportional gain system is given by

$$R_{||} = \frac{1}{\frac{1}{R_2 + 1/(i\omega C)} + \frac{1}{R_1}}. \quad (3.18)$$

Hence the transfer function of the inverting operational amplifier configuration is given by

$$G(i\omega) = -\frac{R_{||}}{R_3}. \quad (3.19)$$

For low frequencies ω the the transfer function of the system can be approximated by

$$G_{\omega \rightarrow 0} = -\frac{R_1}{R_3}, \quad (3.20)$$

while for high frequencies the gain can be approximated by

$$G_{\omega \rightarrow \infty} = -\frac{\frac{R_1 R_2}{R_1 + R_2}}{R_3} = -\frac{R_1 R_2}{R_3(R_1 + R_2)}. \quad (3.21)$$

From Eqn. (3.20) and Eqn. (3.21) the low and high frequency limits of the proportional element can be computed. For the gain to be (negative) unity in the low frequency regime the ratio of R_1 and R_2 should be roughly 1, as can be seen from Eqn. (3.20). To get a low

gain for high frequencies the resistor value of R_2 should be fairly small in comparison with the resistor values of R_1 and R_3 as can be seen in Eqn. (3.21). A plot of the gain and the phase of Eqn. (3.18) can be depicted from Fig. 3.5.

With a proportional gain configuration as described in Fig. 3.5(b) we are able to implement negative feedback. We are also able to dampen high frequency components of the phase detector while amplifying the low frequency components with a limited gain.

It is important to note that all calculations in this chapter are only theoretical calculations assuming that the transfer function is linear over all frequencies. The calculations from above give a good intuition for the behavior of the PI loop. However, for real operational amplifiers, this assumption cannot be true since the operational amplifier is only in approximation a linear device. Therefore real measurements of transfer functions will deviate from our model. One should keep in mind that real operational amplifiers have finite open loop gains. Hence, an integrator can at maximum amplify low frequency values with the open loop gain of the operational amplifier. Since the open loop gain is a frequency dependent upper boundary of the integrator's amplification, the phase lag in this frequency region goes to zero.

3.3 Description of a Phase-locked loop (PLL)

A phase-locked loop is a feedback technique which references an oscillator to a reference oscillator and makes the two oscillators phase-stable. This can be achieved with a feedback system as depicted in Fig. 3.6 which looks similar to the general schematic of a linear feedback system shown in Fig. 3.2. The system with transfer function $G(s)$ is here represented by a voltage controlled oscillator (VCO) with a frequency modulation input. The detector with transfer function $D(s)$ is replaced by an electronic phase detector. The loop filter with transfer function $K(s)$ consists of different operational amplifier configurations. The two signals $v_{\text{ref}}(t)$ and $v_{\text{VCO}}(t)$ are both cosine waves with frequencies ω_{ref} and ω_{VCO} . The reference is assumed to be an absolutely stable reference with frequency ω_{ref} and no phase noise, while the VCO is oscillating at frequency ω_{VCO} with a fluctuating phase $\phi_{\text{VCO}}(t)$. Therefore it holds that

$$v_{\text{ref}}(t) = v_0 \cos(\omega_{\text{ref}}t) \quad (3.22)$$

$$v_{\text{VCO}}(t) = v_0 \cos(\omega_{\text{VCO}}t + \phi_{\text{VCO}}(t)). \quad (3.23)$$

The phase detector produces an output linearly proportional to the phase difference between the two signals $v_{\text{ref}}(t)$ and $v_{\text{VCO}}(t)$. If the phase difference changes over time then the two oscillators differ in frequency. However, the phase detector can also give a linear discrimination signal for two oscillators if the frequency difference is within the linear frequency regime of the phase detector. This linear phase or frequency discrimination

signal will then be weighted using a loop filter as described in the next Section. If the loop filter is tuned correctly, the VCO will be modulated such that the VCO tracks the frequency and phase of the reference.

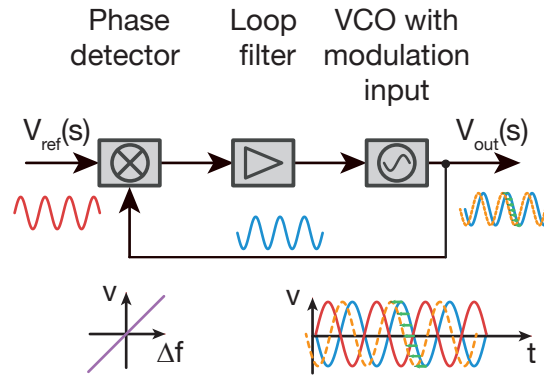


Fig. 3.6 A phase-locked loop. The frequency difference between the reference signal (in red) and the VCO signal (in blue) is compared in the phase detector. For frequency differences of the reference signal and the output signal that are within the loop bandwidth the phase detector gives a linear error signal (see inset under phase detector). The error signal is then fed into the loop filter which weights the error signal and then controls the VCO frequency via the modulation port of the VCO. If the loop filter is tuned correctly, the VCO signal is following the reference signal in the direction of the green arrows and then becomes the orange periodic function in the inset.

A feedback loop can either amplify a fluctuation of the system or it can counteract against the fluctuation of a signal. The VCO from our example oscillates at a higher frequency if the voltage on the modulation input port increases and oscillates at a lower frequency if the voltage on the modulation input port decreases. Therefore, our loop filter must make sure that if the phase of the VCO signal is larger than the phase of the reference signal, the loop filter outputs a negative voltage and vice versa to obtain a stable phase relation. This counteracting of the fed back signal is called negative feedback.

The modulation bandwidth of a VCO describes how fast the VCO can change its frequency when modulated. The loop filter also has a bandwidth specified as the frequency at which the gain response of the loop filter is half the gain it is for low frequencies.

For the loop filter bandwidth design we have two different choices. One option is to choose the loop filter bandwidth to be small. In this case the loop filter will have a high gain for low frequencies and the gain will fall off quickly. Using a loop filter configuration like this will let the VCO follow the reference only slowly, i.e. drifts and low frequency noise fluctuations can be compensated, but high frequency fluctuations can not. If the phase-noise properties of the VCO are good enough for the desired application, then a low-bandwidth loop filter is a good choice. If we design the loop filter to have a high bandwidth, the VCO will be able to follow fast frequency fluctuations of the reference.

This means we can not only compensate for drifts of the VCO but also for bad phase noise properties of the VCO since in this case the negative feedback can compensate the VCO's phase noise relative to the reference. However, if the phase noise properties of the reference signal are not good or influenced by spurious signals within the loop filter bandwidth, these noise components will be transferred to the VCO signal.

Apart from the design choice for a high or low bandwidth loop filter, one must also decide which transfer function profile is optimal for a phase-locked loop. The gain of the loop filter for low frequencies should be high. If the error signal contains non-zero DC-components then the two oscillators of the PLL are not phase stabilized, i.e. the VCO signal has a different frequency than the reference signal. With an amplification of the low-frequency components of the error signal, the VCO can get more quickly phase stabilized to the reference oscillator. Higher frequency components of the error signal should not be amplified as much as low frequency components, otherwise the VCO might not end up in a stable phase relation with the reference oscillator, but rather make the PLL unstable.

Another design consideration is the noise performance of the loop filter. Any noise in the feedback loop will be transferred onto the VCO because it can not be discriminated from fluctuations on the output. A loop filter should therefore be designed such that its added noise to the system (also called noise figure of the loop filter) is small. A loop filter can be either realized as a digital loop filter or as an analog loop filter. Digital loop filters can have more variable transfer function profiles but are generally precision-limited because their digital to analog converter can only resolve a discrete ratio of the voltage of their output voltage regulator. Hence, the output signal can only change stepwise, which does not allow for a smooth tuning of the output voltage of the digital loop filter. Thus, a digital loop filter is less sensitive to changes of the feedback loop and also more noisy when servoing on a specific setpoint. We decided to build an analog loop filter for the phase-locked loop of the fiber noise cancellation because the application of the phase-locked loops requires low noise characteristics and a fine tuning range of the feedback loop.

Chapter 4

The Strontium Laboratory Photodetector

This chapter gives an overview of the design of the fast photodetector developed in the Strontium laboratory. It was initially designed by Nejc Janša [32] in 2016 and was further developed in the subsequent years. Since then, two versions of the photodetector were developed: A low-bandwidth photodetector with high gain (in the following called slow photodetector) mostly used for laser intensity stabilization and absorption spectroscopy, and a high bandwidth photodetector with low gain (fast photodetector), developed for laser frequency stabilization and beat measurements. Nejc's version of the photodetector (version 4.1) can be equally used for low bandwidth applications. For high bandwidth applications the photodetector printed circuit board design was optimized to reduce parasitic capacitance.

In this Chapter we first review the basic schematic of a photodetector. We will develop a model for the bandwidth for the gain-bandwidth-product of a photodetector. Then we will measure the residual parasitic capacitance on the current version of the fast photodetector board and give examples for possible transimpedance/bandwidth combinations for the fast photodetector board.

4.1 The Photodetector Circuit

Our photodetector boards consist of three different parts: The photodiode, the transimpedance amplifier, and the second stage amplifiers. The three different parts are described in the following.

4.1.1 A Model for a Photodiode

Photons from a light source can create electron hole pairs when incident on a photodiode via the photoelectric effect [33]. However, the speed with which electron-hole pairs can be created is finite. The capacitance of a photodiode C_D , corresponding to the cut-off frequency of the transfer function of the photodiode, is many orders of magnitude larger than needed to detect light waves directly. Hence, photodiodes create an averaged current corresponding to the average intensity of the light wave incident on the photodiode.

However, photodiodes with bandwidths of several GHz are commercially available. An equivalent circuit diagram of the photodiode is shown in Fig. 4.1.

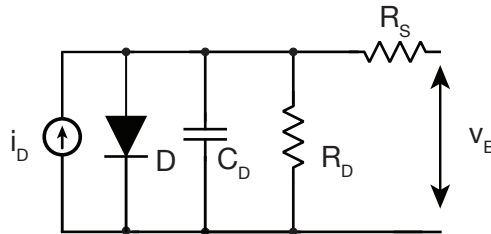


Fig. 4.1 Model of a photodiode with a current source i_D , a diode D , a capacitance C_D , and the resistances R_D and R_S . The photodiode is biased with voltage v_B . Figure adapted from Ref. [33].

A photodiode can be modeled by a current source i_D , an ideal diode D , a capacitor C_D modeling the electric charge stored by the photodiode and an output resistance modeling the residual current flow (dark current) when biasing the photodiode. Biasing the photodiode with a bias voltage v_B decreases the capacitance of the photodiode. This can be explained by an increased distance between the two depleted regions of the photodiode where the charge carriers of the semiconductor have been diffused away. Increasing the distance between the two depleted regions then leads to a decreased capacitance as the two depleted regions act as a plate capacitor [33]. The output current of the photodiode is linearly related with to incoming light power via the responsivity coefficient η .

Linearity of photodetectors used in feedback systems is essential. In the photodetector board setup a transimpedance amplifier configuration preserves the photodiode's signal linearity when transferring the current signal to a voltage signal.

4.1.2 Transimpedance Amplifier

A model of a transimpedance amplifier configuration for a photodiode is given in Fig. 4.2. It consists of a negatively biased photodiode, an inverting operational amplifier configuration as described in Eqn. (3.14) with frequency-dependent gain $A(s)$, a feedback resistor determining the gain of the operational amplifier, and capacitances coupling elements of the circuit at different positions with each other. The photodiode's capacitance limits the bandwidth of the photodiode. The common-mode capacitance of the C_{CM} couples the inverting terminal of the operational amplifier to ground, while the differential capacitance C_{DIFF} couples the inverting terminal of the operational amplifier to the noninverting terminal of the operational amplifier. These two capacitances are determined by the PCB board design and will dominate the capacitance of the fast photodetector PCB in the following.

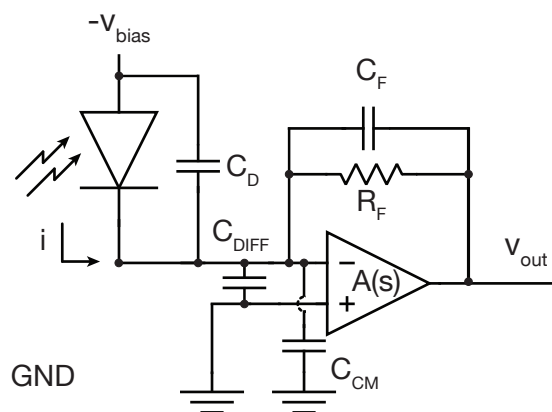


Fig. 4.2 Schematic of the transimpedance amplifier with open loop transfer function $A(s)$. The inverting amplifier configuration has a feedback impedance consisting of R_F and C_F . The photodiode is negatively biased and connected to the inverting input terminal of the operational amplifier. Its capacitance is represented by C_D . The capacitance C_{DIFF} couples the operational amplifiers input terminals and the capacitance C_{CM} couples the inverting terminal of the operational amplifier to ground. Figure adapted from Ref. [34].

A transimpedance amplifier has high-impedance input terminals. However, the negative feedback configuration of the current-to-voltage transformer described in Fig. 4.2 bypasses the operational amplifier's negative input terminal to the output terminal of the operational amplifier and forces the load of the photodiode to zero. Hence, there is only very little voltage swing over the operational amplifier if the current on the photodiode output changes.

To explore the linear characteristics of the transimpedance amplifier let's take a look at the transfer function of the transimpedance amplifier configuration. An inverting operational amplifier configuration with a frequency-independent open-loop gain is described in Eqn. (3.14). However, for our fast photodiode design with low capacitance photodiodes the non-infinite open-loop gain of the operational amplifier will influence the photodiode's bandwidth. Hence, the operational amplifier's gain $A(s)$ is modeled as a low pass filter where the operational amplifier's gain crossover frequency (denoted as gain-bandwidth product GBP) is defined as the frequency of unity loop gain. The transfer function of the transimpedance configuration is given as [34]

$$\frac{V_O}{I_D} = \frac{-Z_F}{1 + \frac{1+Z_F/Z_G}{A(s)}}, \quad (4.1)$$

where Z_F is the feedback impedance of the operational amplifier determined by the capacitor and the resistor connected in parallel and $Z_G = 1/C_S$ is the noise gain of the system determined by the overall source capacitance [31, 34]

$$C_S = C_D + C_{DIFF} + C_{CM}. \quad (4.2)$$

For low frequencies the loop gain from Eqn. (4.1) is determined by the open-loop gain of the amplifier A_{OL} . This case is the relevant case for the slow photodetector. In the high frequency regime, the transfer function is not so easy to evaluate. However, Fig. 4.3 gives a sketch of the transfer function of the system.

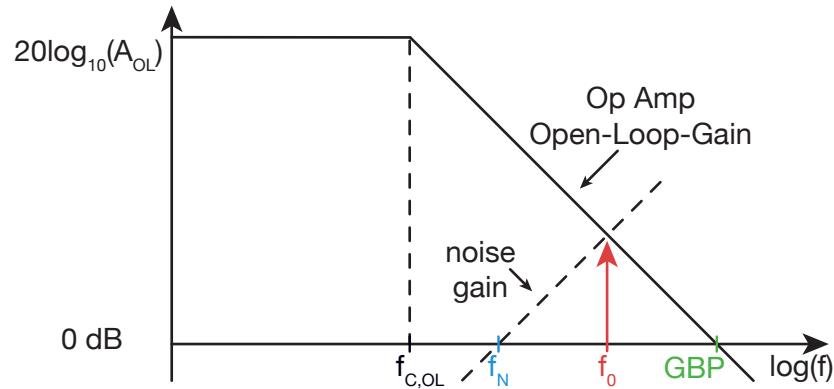


Fig. 4.3 The gain of the transfer function of the transimpedance amplifier. The plot shows the gain of the transfer function on the y-axis and the logarithmic frequencies of the power spectral density on the x-axis. The gain from the operational amplifier is flat up to the cutoff frequency $f_{C,OL}$. The noise gain crosses 0 dB at f_N . At frequency f_0 the noise gain meets the operational amplifier roll off and the total gain of the noise spectrum of the amplifier has a maximum. The Op Amp open loop gain crosses 0 dB at the crossover frequency. Figure adapted from Ref. [34].

The transfer function of the transimpedance amplifier consists of two components: The operational amplifier loop gain is determined by the operational amplifier characteristics. It has a low pass filter behavior and falls off linearly on a log-log plot of gain vs frequency after its frequency of maximum noise gain, reaching unity gain at the gain crossover frequency. The noise gain of the amplifier is caused by the source capacitance, increases linearly on the log-log plot of gain vs frequency and crosses unity gain after the noise crossover frequency [34]

$$f_N = \frac{1}{2\pi R_F (C_F + C_S)}. \quad (4.3)$$

The noise gain and the operational amplifier loop gain cross at the frequency of maximum noise gain, where the transfer function reaches a maximum. The noise gain is damped by the operational amplifier gain for frequencies higher than the frequency of maximum noise gain f_0 . The frequency of maximum noise gain in this model is given as [33]

$$f_0 = \sqrt{f_N \cdot \text{GBP}}, \quad (4.4)$$

where the gain bandwidth product is specific for the used operational amplifier. The bandwidth given by the frequency, where the resonance of the photodetector is decreased by 3 dB. It is related to the frequency of maximum noise gain since the operational

amplifier gain roll off is linear on a log-log plot of gain vs frequencies.

For our high-bandwidth photodiodes the capacitance C_D is approximately half the operational amplifiers common-mode and differential capacitance $(C_{DIFF} + C_{CM})/2$. Hence we can assume that the transfer function of the photodiode (isolated from the transimpedance amplifier) will roll off for higher frequencies than the transfer function of the operational amplifier.

4.2 Testing the Bandwidth of the Fast Photodetector Board

Using last section's approximations about the transfer function of the transimpedance amplifier we can now estimate the parasitic capacitance of the current version of the fast photodetector board. Also we will be able to give a selection criterion for the target bandwidth of a photodetector's transimpedance.

The signal path of the fast photodetector circuit schematic is shown in Fig. 4.4. The voltage regulators are the same as in Nejc's design [32].

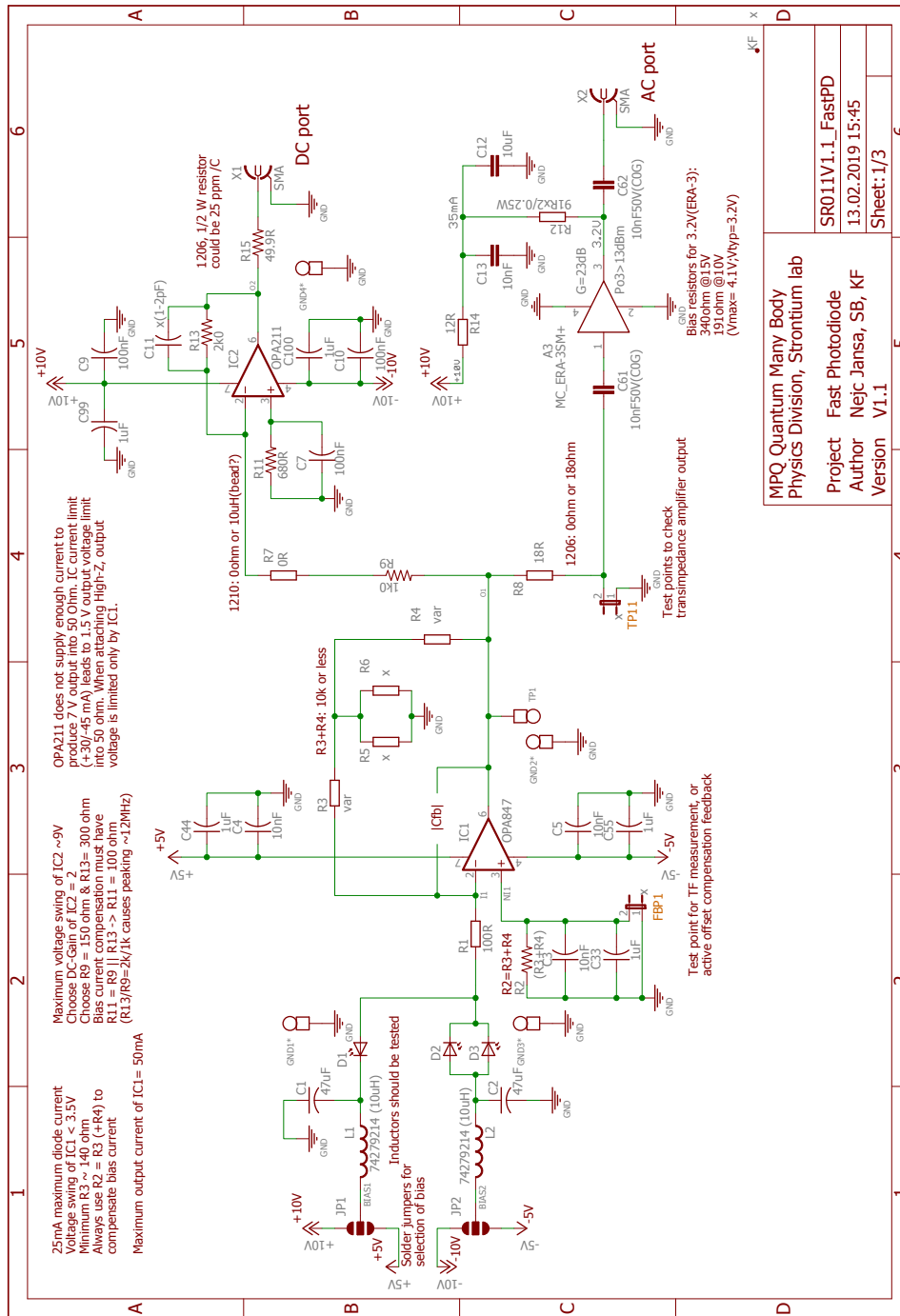


Fig. 4.4 Schematic of the fast photodiode version V1.1. Main features are the positive biased photodiode, which is connected on the D1 slot. The transimpedance amplifier (IC1) with the transimpedance resistor (R3 and R4) and the compensating resistor (R2) is followed by a DC-(IC2) and an AC-coupled (IC3) second amplification stage.

The transimpedance stage of the circuit resembles the schematic from Fig. 4.2. The photodiode is connected to the inverting input of the transimpedance amplifier. The transimpedance amplifier's output and inverting input terminal are connected via the transimpedance resistance. The compensating resistor ensures that the current present at the non-inverting terminal matches the current flowing through the transimpedance resistance to the inverting terminal of the operational amplifier. It is important to have a close to zero offset voltage for small photodetector signals for intensity stabilization of signals (refer to Ref. [33] for further reading). The transimpedance amplifier's output is connected to the DC-coupled monitor signal path and the AC-coupled signal output, where high bandwidth signals can be monitored.

We wanted to test the bandwidth characteristics of our photodetector boards and built a test setup with the Hamamatsu S5973 photodiode. This photodiode has a capacitance $C_D = 1.6$ pF at 3 V bias voltage, which corresponds to a cutoff frequency of 1 GHz. As an operational amplifier we use the OPA847 (Texas Instruments), which is a voltage-feedback operational amplifier with a GBP = 3.9 GHz, a differential capacitance $C_{DIFF} = 2.0$ pF and a common-mode capacitance $C_{CM} = 1.7$ pF. At the AC-coupled second amplification stage we use an ERA-3+ (Mini-Circuits) amplifier. This amplifier has a typical gain of 23.4 dB and a bandwidth of approximately 3 GHz. Hence neither the bandwidth of the photodiode nor the bandwidth of the second stage amplifier limited us in our test.

For our bandwidth test we first needed to demonstrate that measuring the noise power spectral density of the photodiode is equivalent to determining the bandwidth of the photodetector. We tested this by measuring the gain of the transfer function of a periodic signal through the photodiode. This can be done by connecting the tracking generator of a spectrum analyzer to the input of the transimpedance amplifier and then measuring the transmitted signal through the transimpedance amplifier on the spectrum analyzer. For this test we used the setup shown in Fig. 4.5(a).

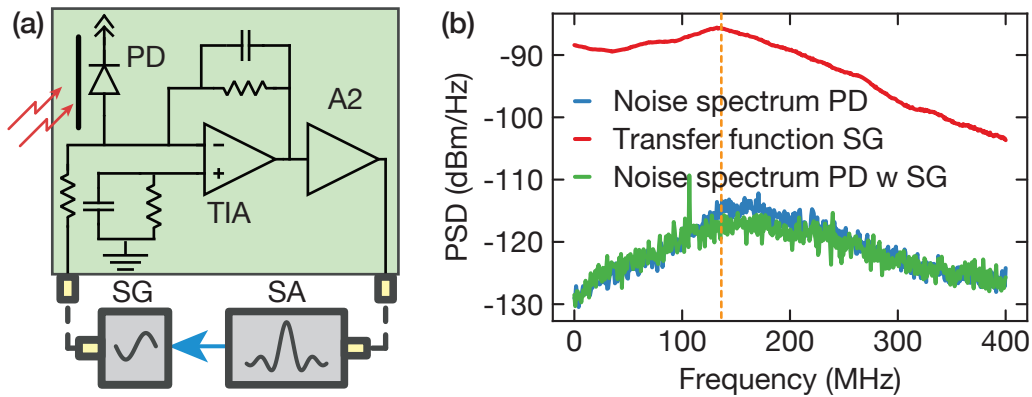


Fig. 4.5 Test setup for determining the bandwidth of the photodetector. (a) The photodiode (PD) is connected in parallel to the tracking generator (SG) of the spectrum analyzer (SA), which is connected in series with a $910\ \Omega$ resistor. The output of the photodiode and the tracking generator is connected to the transimpedance amplifier (TIA). The output signal from the transimpedance amplifier is amplified on a second amplification stage (A2) and measured by the spectrum analyzer. Incident light on the photodiode is blocked. (b) The transfer function of the signal from the tracking generator is measured. The noise spectrum of the transimpedance amplifier without the tracking generator connected but with an additional not terminated SMA port is plotted in green. The transferred signal of the tracking generator is connected in parallel with the photodiode and amplified by the transimpedance amplifier as shown in red. The blue curve shows the noise power spectral density of the photodiode without the additional SMA port. The orange dashed line indicates resonance frequency of the transfer function. The resolution bandwidth (RBW) of the SA is 10 kHz.

In our test setup we connected the tracking generator of the spectrum analyzer (Rohde & Schwarz FSEB 30) with the photodiode output in parallel. The tracking generator's output is at a constant power level but changes its frequency synchronously with the sweep of the spectrum analyzer. Hence, with the knowledge of the knowledge of the power level at the output of the tracking generator, the spectrum analyzer can calculate an estimate of the transfer function of the operational amplifier.

Knowing the signal level of the tracking generator ($-80\ \text{dBm}$) and the amplification of the second stage of the photodetector (23 dB), we can estimate the resulting power on the spectrum analyzer. We expect the transferred power spectral density of the tracking generator signal on the spectrum analyzer to be amplified by 23 dB plus an additional 6 dB because the low-impedance output signal of the signal generator was measured on the high-impedance input port of the transimpedance amplifier. Adding an additional 40 dB on the spectrum from Fig. 4.5(b) to compensate for the subtracted resolution bandwidth of the power signal, we obtained a spectrum analyzer signal of roughly $-45\ \text{dBm}$ on the spectrum analyzer.

Further we can see in Fig. 4.5(b) that the maximum gain frequency of the power spectral density of the transferred signal from the tracking generator matches with the frequency

of maximum noise gain of the photodetector (with and without an added SMA cable). The tracking generator is connected to the photodetector as shown in Fig. 4.5(a). Hence, we can assume that the bandwidth obtained from the noise power spectral density of the photodetector is a good approximation for the bandwidth of the photodetector.

With the test setup shown in Fig. 4.6(a) we can measure the noise spectra of the fast photodetector for different transimpedance resistances.

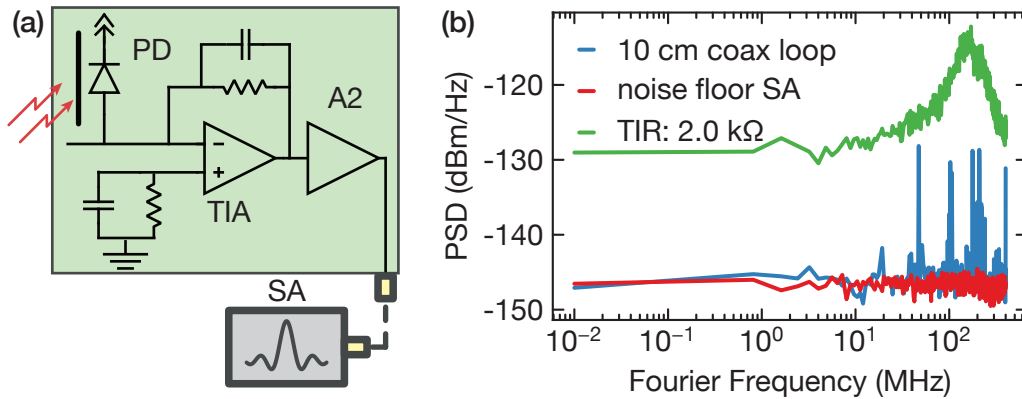


Fig. 4.6 Test setup for the measurement of the fast photodiode's bandwidth. (a) The photodetector is connected to a spectrum analyzer while the photosensitive area of the photodiode is covered. (b) Power spectral density on a logarithmic frequency axis of the photodetector with a transimpedance resistance (TIR) of $2.0 \text{ k}\Omega$ (green trace). The spectrum analyzer noise floor is displayed in red. The coax loop power spectral density is displayed in blue.

For this test, the photosensitive area of the photodiode on the photodetector was blocked. The photodetector AC-coupled output was connected to the spectrum analyzer (SA). Care was taken to not couple in electric noise at RF-frequencies by shielding the photodiode using an anodized aluminum casing around the photodiode. The screws connecting the photodiode to its anodized casing must be tightened to increase electrical contact and hence shielding from the environment.

The noise power spectral density of a photodetector with a transimpedance resistance of $2.0 \text{ k}\Omega$ is shown in Fig. 4.6(b). The noise power spectral density of the photodetector is flat for low frequencies and has a resonance at the frequency of maximum noise gain f_0 . Equation (4.4) relates the frequency of maximum noise gain of the noise power spectral density to the transimpedance of the configuration.

The frequency of maximum noise gain is a good reference value to obtain the -3 dB bandwidth as can be seen in Fig. 4.7(a).

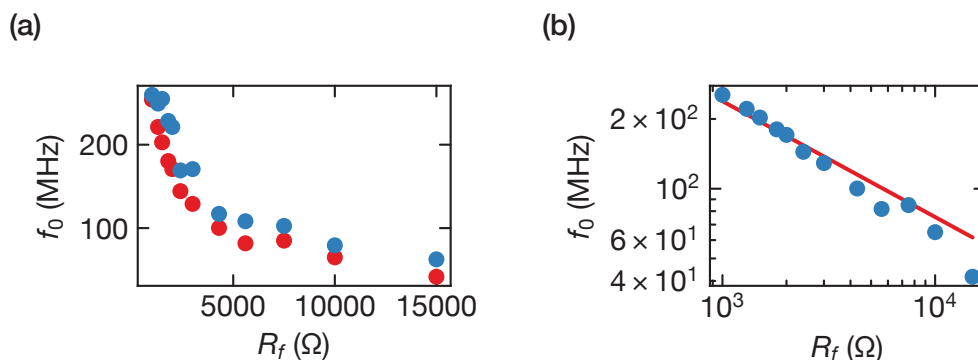


Fig. 4.7 Determining the parasitic capacitance of the fast photodiode. (a) Frequencies of maximum noise gain f_0 (red trace) and bandwidths (blue trace) of the fast photodetector plotted against transimpedances. (b) The resonance frequencies f_0 are plotted against transimpedances on a log-log plot. The values are fitted using Eqn. (4.4). From the fit one obtains a total capacitance of 10.6 pF.

Comparing the frequency of maximum noise gain of our setup for transimpedances from 1 k Ω to 15 k Ω gives a measure for the parasitic capacitance on the photodetector board. Fitting Eqn. (4.4) to the obtained values gives a value for $C_{\text{tot}} = C_S + C_F + C_P$, where C_P is the parasitic capacitance from the board design and from imperfect soldering.

The fitted capacitance of 10.6 pF contains errors not only from the uncertainty of the fit but also from uncertainties from soldering, since we needed to resolder the transimpedance resistance for each noise power spectral density. Subtracting the capacitances from the photodiode and the operational amplifier, this calculation leaves us with a parasitic capacitance of 5.3 pF. Parasitic capacitances can be easily picked up at any part of the PCB. We expect the feedback resistor to have a contribution to the parasitic capacitance of < 1 pF, the 100 Ω resistor between the diode and the transimpedance amplifier to have a < 1.5 pF contribution to the parasitic capacitance, which leaves a contribution of approximately 2 pF to the parasitic capacity from the printed circuit board and the box surrounding it.

The parasitic capacitance on the new version of the fast photodetector can be compared with Nejc's version of the board [32]. Nejc measured a frequency of maximum noise gain of approximately 45 MHz on his photodiode without additional phase compensation capacitance. Solving Eqn. (4.4) for the capacitance C_{total} and plugging in the GBP = 900 MHz of the operational amplifier LM6609 [35] and the transimpedance resistance $R_T = 3$ k Ω that Nejc used, we get an approximate value for the capacitance of the old version of the PCB of $C_{\text{total}} = 24$ pF. From this value one must subtract the input capacitance of the operational amplifier $C_I = 1.2$ pF and the diode's capacitance $C_D = 1.6$ pF to obtain the PCB's parasitic capacitance.

The choice of transimpedance resistance of the fast photodiode should be adjusted for the highest estimated bandwidth of the photodetector needed in the application. For Pound-Drever-Hall frequency stabilization applications with modulation frequencies of around 20 MHz usually bandwidths of approximately 50 MHz are more than sufficient. Hence a 15 k Ω or 20 k Ω resistor is suggested. For higher frequency applications one can go to low resistance values as e.g. 1.0 k Ω resistance which gives a bandwidth of approximately 280 MHz. In Fig. 4.8, a comparison of the the homebuilt fast photodetector with transimpedance resistances of 10 k Ω , 2.4 k Ω and 1.0 k Ω and the photodetector PD10A2 from Thorlabs with a specified bandwidth of 150 MHz is shown.

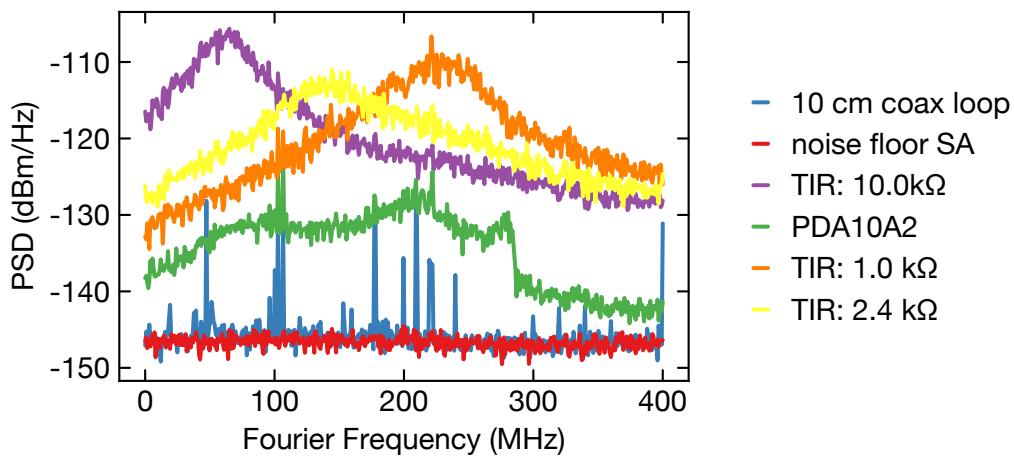


Fig. 4.8 Comparison of different photodetectors. The power spectral density is plotted against a linear frequency x-axis. The PSD of the fast photodetectors with 1.0 k Ω transimpedance resistance (TIR) (orange trace) is compared with the PSD of the fast photodetector with 10 k Ω (purple trace), the PSD of the fast photodetector with 2.4 k Ω transimpedance resistance (yellow) and with the Thorlabs photodetector PD10A2 with specified bandwidth of 150 MHz (green trace). The spectrum analyzer noise is plotted in red and the coax loop power spectral density is plotted in blue.

A 10 cm coax loop is measured to identify the spurious peaks of radio bands and other noise sources on the noise power spectral density of the photodetectors (see e.g. the radio band peak on the noise power spectral density of the Thorlabs photodetector in Fig. 4.8).

Unfortunately comparing the homebuilt fast photodetectors and the Thorlabs fast photodetectors is not so easy. The homebuilt photodetector with 2.4 k Ω transimpedance resistance has a similar bandwidth as the Thorlabs photodetector, but a significantly higher noise power spectral density. We do not know what the electrical schematic of the Thorlabs photodetector looks like, but the gain of the circuit is specified as 5 kV/A for

50 Ω impedances and the transimpedance amplifier is also of type OPA847. With the GPB of the OPA847 one cannot obtain a frequency of maximum noise gain of 150 MHz using a 10 k Ω transimpedance resistance (see Eqn. (4.4) with $C_N = 1$ pF). Hence the specified gain of the Thorlabs photodetector can only be obtained by a second amplification stage.

The homebuilt fast photodetector with a gain of 1 k Ω has a comparable noise spectrum to the Thorlabs photodetector PD10A2 up to frequencies of approximately 100 MHz. An approximately 6 dB higher noise spectral density of the fast photodetector is caused by a 23 dB second amplification stage which boosts the 1 k Ω gain of transimpedance amplifier to an overall 10 kV/A gain. Hence, the 1 k Ω homebuilt photodetector has double the gain of the Thorlabs photodetector. Converting the voltage gain to a power spectral density gives a 6 dB difference on the power spectral density, which lets the two photodetectors perform similarly concerning noise specifications.

However, the noise power spectral density of the homebuilt fast photodetector has a noise peak at its frequency of maximum noise gain. This behavior deviates from an ideal low-pass filter roll off and is caused by a high parasitic capacitance of the transimpedance resistor for low resistor values. This mechanism can not easily be solved. Hence it is recommended to use the photodetector board for detecting signals with frequencies well below the unity frequency; ideally one uses the photodetector board at frequencies below the frequency of maximum noise gain, where the noise gain is heavily suppressed. The unity noise gain frequency f_N for the 1.3 k Ω transimpedance is 6 MHz (obtained from Eqn. (4.3) and plugging in the fitted capacitance value for the board). However, this frequency is much lower than typical beat frequencies we use the fast photodetector for. Hence, for typical high frequency measurements with the photodetector board we will always have noise from parasitic capacitances on our PCB.

With the redesign of the fast photodetector we made an important improvement on the parasitic capacitance of the photodetector circuit. We designed a general-purpose fast photodetector which is adaptable to most photodiodes. Additionally, we can adapt the fast photodetector circuit to match the gain and the bandwidth to the needs of the application.

Chapter 5

A Phase-locked Loop for Fiber Noise Cancellation

External noise processes can broaden the phase noise spectrum of a frequency stabilized laser if the laser is exposed to perturbation processes. A change in the refractive index of the air or of a fiber will shift the phase of the laser such that it undergoes phase fluctuations. For a frequency-narrow laser this effect can be quite significant. A laser with a full width half maximum frequency uncertainty on the order of 1 Hz can be broadened up to the level of 1 kHz in an optical fiber [36]. With a fiber noise cancellation system we can actively compensate for the phase shift picked up in an optical fiber.

Jun Ye kindly shared the electronic schematics for the JILA fiber noise cancellation system with us. His design is described in Ref. [36]. We adapted his electronic schematic and designed a new printed circuit board (PCB) on the basis of this schematic.

The aim of this section is to describe the working mechanism of the fiber noise cancellation. First, we will understand how to detect noise on a laser. Then we will explain how to describe phase noise on the fiber arm. Next, we will describe the design of a setup which can detect phase noise induced by an optical fiber. Afterwards, the electronic setup used to actively compensate for phase noise will be described. With a test setup we will measure the bandwidth and noise damping performance of the first version of our fiber noise cancellation system. Finally, we will summarize problems of the first version of the PCB and we will discuss future improvements to the design of the electronic circuit.

5.1 Optical Heterodyne and Homodyne Mixing

In Chap. 2 we discussed the lineshapes of lasers. We obtained approximate expressions for their lineshape for different noise models. However, measuring the lineshapes of lasers is not straightforward. The narrow linewidth transitions of strontium are in the red. In the wavelength range from 600 nm to 700 nm corresponding to frequencies between 430 THz and 500 THz. These frequencies are far beyond the bandwidths of any photodetectors - our homebuilt photodetectors have bandwidths of up to 280 MHz. Hence, we can not detect the light spectrum directly, but we need to interfere two electric fields on a photodetector to gain information about their spectral profile. Let's assume that we combine

beams with electric fields E_A and E_B

$$E_A(t) = E_A a(t) \operatorname{Re} [e^{i(\omega_A t + \phi_A(t))}] \quad (5.1)$$

$$E_B(t) = E_B a(t) \operatorname{Re} [e^{i(\omega_B t + \phi_B(t))}], \quad (5.2)$$

with frequencies ω_A and ω_B , phase noise $\phi_A(t)$ and $\phi_B(t)$ and amplitude modulation $a(t)$ on a photodetector. The two fields are assumed to have the same polarization. Hence the signal on the photodetector

$$\begin{aligned} |E_A(t) + E_B(t)|^2 = & a(t)^2 (|E_A|^2 + |E_B|^2) \\ & + \sqrt{|E_A|^2 |E_B|^2} a(t)^2 \cos[(\omega_A - \omega_B)t + \phi_A(t) - \phi_B(t)], \end{aligned} \quad (5.3)$$

corresponds to low-frequency amplitude-modulation and a standing wave at the difference frequency $|\omega_A - \omega_B|$ of the signals E_A and E_B . However, we need to restrict the model to difference frequencies $|\omega_A - \omega_B|$ within the bandwidth of the photodetector to be able to detect the beat of the two frequencies.

An optical heterodyne beating with two different lasers A and B on a photodiode can be obtained with an optical setup as shown in Fig. 5.1(a).

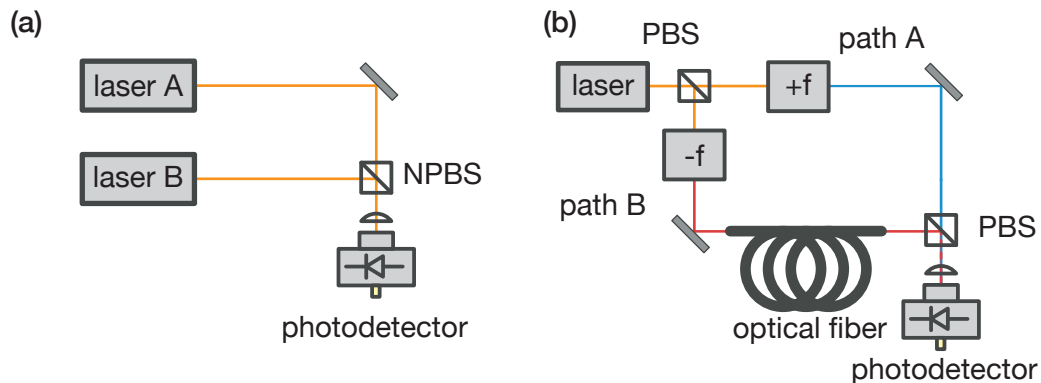


Fig. 5.1 A heterodyne and a homodyne mixing process. (a) Heterodyne mixing of two lasers. Two Lasers A and B are overlapped on a photodetector to obtain interference between the two lasers. (b) Fiber noise cancellation setup. The laser light is split into two interference arms A and B at a polarizing beam splitter. Both arms are frequency-shifted in opposite directions and one of the arms is phase modulated in an optical fiber, while the other interference arm is unperturbed. The two interference arms are combined at a non polarizing beam splitter and then interfere on the photodetector.

Here, the phase noise $\phi_A(t)$ and $\phi_B(t)$ on the beat signal on the photodiode can give information of the overall phase noise both from signal $E_A(t)$ and from $E_B(t)$. The heterodyne mixing setup will be used in Cha. 8 to measure the phase noise properties of our laser. Equation (5.3) can be adjusted to explain the working principle of our fiber

noise cancellation setup. The optical setup corresponds to optical homodyne beating of one laser as shown in Fig. 5.1(b). The laser which is split off into path A and path B is a narrow linewidth laser with a long coherence length. Hence, path A and path B are correlated. However, if we expose path B to a noise source $\phi_B(t)$, which is uncorrelated with the laser, we are able to differentiate these two noise sources on the spectrum on the photodetector. To obtain a nonzero difference frequency of light we additionally placed frequency shifters in the two paths, which supply a frequency difference of $2f$ of the two signals on the photodetector. The resulting AC-coupled signal on the photodiode is given by

$$V_{\text{PD,AC}}(t) = |E_A(t) + E_{A'}(t)|_{\text{FNC}}^2 = \sqrt{|E_A|^2 |E_{A'}|^2} a(t)^2 \cos[2ft - \phi_B(t)], \quad (5.4)$$

assuming that the phase noise $\phi_A(t)$ in path A is negligible. The squared value of the electric field described in Eqn. (5.3) and (5.4) is converted to a voltage in the photodetector as described in the previous Chapter.

5.2 Noise from a Fiber

A possible scenario for phase modulation on light is noise on an optical fiber caused by fluctuations of its refractive index n . If the refractive index changes its value at a specific length interval of the fiber, the light wave travels with a modified speed $c_n = c/n$ in this length interval, where c is the speed of light. A local change of the speed of light will be visible on the phase detector as the optical path length and hence phase of the laser light will change.

If not the refractive index of the light is changed, but rather the length of the light path, i.e. the fiber is stretched, then the optical path length of the light will also change. These fluctuations can be seen as a change of the resonance frequency of the cavity [see Eqn. (6.13)]. However, acoustic noise processes will dominate the noise on a fiber.

We would like to use a phase-locked loop to cancel out the phase deviations in the fiber by modulating the negative of the phase modulation imparted by the fiber on the light. This can either be done by changing the refractive index, changing the length of the fiber, or by changing the frequency of the light. It turns out that the latter method is the most practical since a frequency change (and therefore also phase change) can be easily transferred to the light by an acousto-optic-modulator (AOM) [37]. The choice of an AOM as a frequency and therefore phase actuator explains addition of frequency shifters in Fig. 5.1(b). These modulators convert an applied RF frequency to a refractive index modulation in an acousto-optic crystal. This modulation is used as a diffraction grating to frequency-shift the diffracted laser light [24].

It is important to note that the optical fiber in Fig. 5.1(b) can also be replaced by an arbitrary noise source. Hence the fiber noise cancellation technique can also be used to phase lock two interfering arms of a laser, which e.g. are exposed to different vibrational

influences, but should be common mode. However, to implement this different phase lock scheme with our fiber noise cancellation PCB several changes, which are described in Sec. 5.6, must be considered.

In the next Section we will explain the test setup for fiber noise cancellation.

5.3 Optical Setup

The fiber noise cancellation test setup should test the fiber noise cancellation capabilities of our cancellation system for noise generated on the fiber. Hence, we must be able to control the noise properties in a fiber. A fiber in a lab environment will pick up uncontrollable noise. However, we can make noise at different frequencies more prominent by placing a speaker next to the fiber. In this case harmonics of the frequency of the speaker can also be seen on the spectrum. A more direct way of analyzing the suppression of noise from a fiber cancellation system is to actively phase-modulate the system. This can be realized by using an electro-optic-modulator (EOM) [20]. The EOM modulates the phase of the electric field of the light as described in Sec. 2.2. The fiber EOM (Jenoptik PM705) we use has a very large bandwidth, which we can use to generate phase noise on the fiber. Additionally the fiber EOM phase modulation response is linear to the modulation voltage within its bandwidth. This method gives us an estimate of the bandwidth of the fiber noise cancellation setup since we directly compare how much specific frequencies get damped.

The fiber noise cancellation test setup implements an interferometer as shown in Fig. 5.1(b). However, the test setup is more complicated, since we need to frequency actuate the light that goes through the fiber. The test setup is shown in Fig. 5.2 and explained in the following.

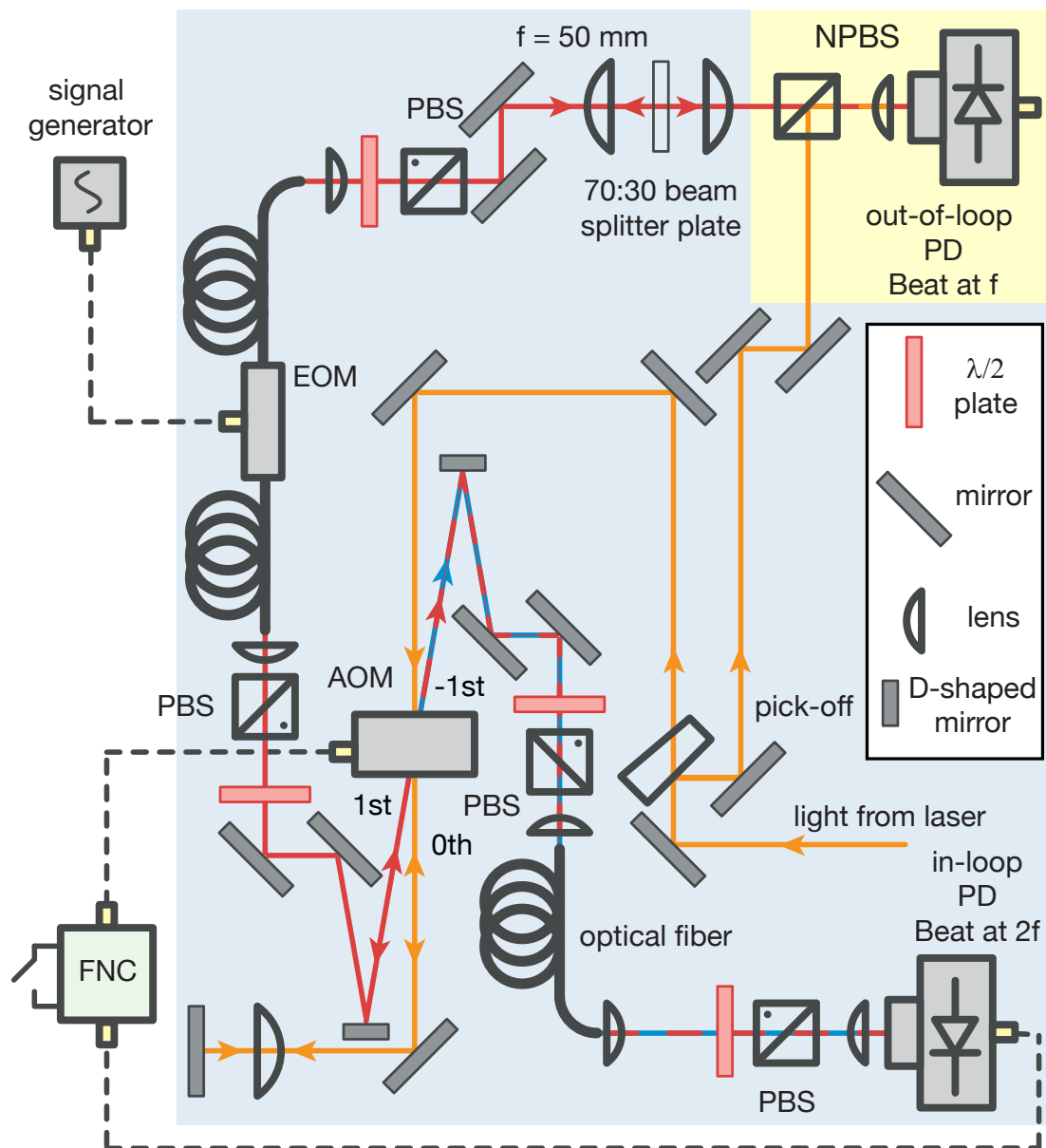


Fig. 5.2 Optical setup for the test of the fiber noise cancellation system. In the in-loop setup (blue shaded) light from a narrow linewidth laser is sent through an AOM. The red detuned transmitted first order of diffraction (red beam) of the AOM is sent through an EOM, phase noise is generated on this arm using a signal generator, and partially backreflected at a beam splitter plate. The light then travels back through to the AOM and gets diffracted again. The transmitted zeroth order of diffraction is retroreflected through the AOM and then blue detuned on the negative first order diffraction of the AOM (blue beam). Both the blue and the red beam are combined on the in-loop photodetector. The out-of-loop setup (yellow shaded) is obtained from a beat of the laser with the single fiber pass light on the out-of-loop photodetector. The fiber noise cancellation PCB actuates the AOM by using information obtained by the in-loop-PD. Symbols: polarizing beam splitter (PBS), non polarizing beam splitter (NPBS).

Light from a narrow linewidth laser is incident on the setup. A beam sampler splits off a beam and guides it to the out-of-loop setup. The rest of the light is sent through an AOM (Gooch & Housego AOMO 3080-120). Here, the first order diffraction gets 80 MHz red detuned. The beam is then polarization-cleaned with a $\lambda/2$ -plate and a polarizing beam splitter (to only keep one linear polarization) and coupled into the fiber EOM. In the fiber EOM, the light gets modulated with a signal generator and picks up the phase noise $\phi_{\text{EOM}}(t)$. The light leaving the fiber is again polarization cleaned, and then partially retro reflected at a 70 : 30 beam splitter plate. The transmitted light through the beam splitter plate is guided to the out-of-loop setup. Lenses with focal length $f_{\text{focal}} = 50$ mm are used in a cat's eye configuration [38] to achieve a good coupling efficiency in the reverse direction through the EOM. Since the light moves with speed of light, the light picks up the same phase noise $\phi_{\text{EOM}}(t)$ on the second pass through the EOM. The perturbed light is guided back through the AOM. On the negative first order of the AOM (first order of the back reflected light), the fiber interferometer arm is overlapped with a reference interferometer arm which passes the AOM in the zeroth order, gets retroreflected and then gets blue detuned in the negative first order of the AOM. The overlapped beam is again coupled into a short polarization maintaining fiber for mode cleaning, since the AOM has some back reflected light that stems from a non perfect AR coating on the AOM crystal. The light incident on the fiber is again polarization cleaned and then focused (not shown) on the in-loop photodetector.

The AC-coupled signal incident on the in-loop photodetector is given by

$$V_{\text{iLPD}}(t) = V_0 \cos[2ft + 2\phi_{\text{AOM}}(t) + 2\phi_{\text{EOM}}(t)], \quad (5.5)$$

where $\phi_{\text{AOM}}(t)$ is the compensated phase on the light from a frequency change of the AOM. If the fiber noise cancellation is locked, this phase shift has the same value as $\phi_{\text{EOM}}(t)$, but with a different sign. If the fiber noise cancellation is not phase stabilized, this value is not actively controlled. The beat signal on the out-of-loop photodetector is used to extract the error signal for the phase-locked loop.

5.4 Electronic Setup

The in-loop-signal oscillating at a frequency of $2f$ must be mixed down to give an error signal for the loop filter. The loop filter will frequency-stabilize a voltage controlled surface acoustic wave oscillator (VCSO) which actuates the AOM to a voltage controlled crystal oscillator (VCXO). The electrical schematic is shown in Fig. 5.3.

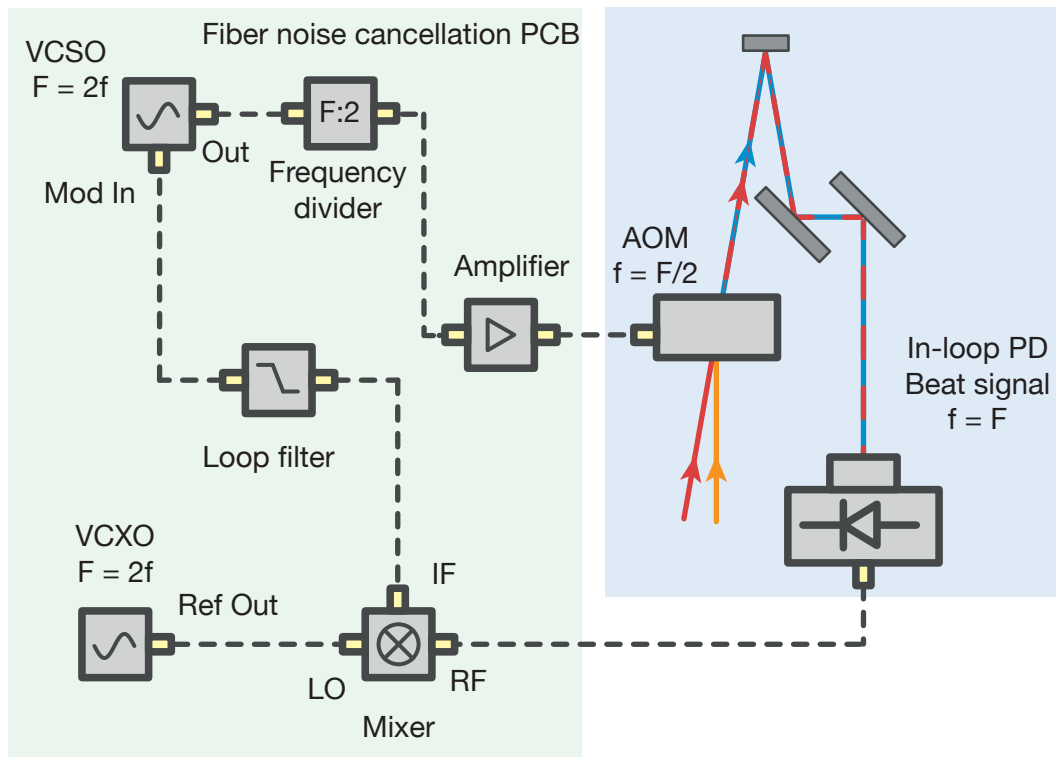


Fig. 5.3 Electrical setup of the fiber noise cancellation. The beat signal oscillating at $2f$ is mixed down using a VCXO at the same frequency in a mixer. Then the error signal at the IF port of the mixer is low pass filtered and sent to a loop filter. The loop filter actuates the VCXO. The output frequency of the VCXO is frequency divided by factor two and drives the AOM via an amplifier.

5.4.1 Choice of Oscillators

The fiber noise cancellation needs two different kinds of VCOs. The modulation oscillator must be modulated very quickly to suppress the noise picked up on the fiber, while the reference oscillator must be very stable since the frequency shift from the first order of diffraction on the light will in the final setup also be on the light sent through the fiber. The light that is sent to the main experiment must be very stable in frequency since our laser is very narrow and if the resonance frequency of the reference oscillator changes, the overlap between the laser and the atomic transition will decrease. However, both oscillators must have low-noise characteristics since any additional phase noise in the feedback loop will add up and be transferred onto the light. The reference oscillator in our application is the ABRACON ABLNO-V-156.250 [39], a voltage controlled crystal oscillator. Its control voltage is grounded with a $2\text{ k}\Omega$ resistor. Oscillators of this kind usually have a very narrowband frequency spectrum. The phase noise of the crystal oscillator 10 kHz detuned from the carrier is -134 dB suppressed with respect to the carrier.

The full specification can be taken from Ref. [39]. The modulation oscillator is chosen such that the modulation bandwidth is high. The VCSO Vectron VS-705 [40] has a modulation bandwidth of 200 kHz which is far above any acoustic noise in the laboratory. It also has very good phase noise properties with a phase noise 10 kHz detuned from the carrier only 20 dB higher than the phase noise from the VCXO.

The output of both oscillators is a square wave with all odd Fourier components of the baseband oscillation at 156 MHz. However, only the baseband of the VCSO is within the bandwidth of the AOM such that the AOM will only see a sine wave.

5.4.2 Extracting the Error Signal from the Beat Signal

We are mainly interested in the phase information of the beat signal from the in-loop-photodetector. However, external perturbations of e.g. the amplitude of the beat signal can change the shape of the oscillation of the sine wave. A modulated beat signal might not correctly reproduce the phase of the beat signal. Hence, in our electronic setup we amplify the beat signal using an RF-limiter such that signals above (below) a threshold voltage get amplified to the upper (lower) voltage limit of the RF-limiter. The RF-limiter sharpens the rising and the falling edges of the sine. Hence, we can determine the phase of the beat signal more precisely.

The error signal of a phase-locked loop should be a straight line which biases the VCSO's frequency linearly. We can mix down the frequency of the in-loop photodetector beat signal a double balanced mixer (DBM). The DBM mixes the voltage from the photodetector V_{iLPD} with the a local oscillator at the same frequency $V_{LO}(t) = V_{LO} \cos(2ft)$ to obtain the intermediate frequency voltage

$$V_{IF}(t) = V_{LO} V_0 \sin[2\phi_{AOM}(t) + 2\phi_{EOM}(t)] + (4f \text{ terms}). \quad (5.6)$$

Low-pass filtering this signal leaves one only with the DC term. Additionally, for small signals one can apply the small angle approximation $\sin(x) \approx x$ to obtain for the phase detector signal

$$V_{IF}(t) = V_{LO} V_0 [2\phi_{AOM}(t) + 2\phi_{EOM}(t)]. \quad (5.7)$$

The low-pass-filtered error signal from the mixer is proportional to the phase noise process $2\phi_{EOM}(t)$ and the compensation phase shift by the AOM $2\phi_{AOM}(t)$. This signal is the output signal from the phase detector and is sent to the loop filter.

5.4.3 Proportional Integral and Derivative Controller

The loop filter of the phase-locked loop converts the error signal to a modulation voltage of the VCSO. The VCSO will then actuate the AOM. Hence, the PI-loop is the element of

the fiber noise cancellation system which calculates the frequency change of the VCXO needed such that the beat signal on the in-loop-photodetector matches the frequency of the reference crystal oscillator. Once the loop is phase stabilized, the loop filter transfers changes of the error signal (corresponding to phase noise on the fiber) to the VCXO.

The loop filter for the fiber noise cancellation consists of three different components: the proportional gain element P responsible for an overall amplification or damping of the error signal, the integral gain element I for the amplification of low frequency parts of the error signal and the high frequency amplifying gain element D. Connecting the P, I and D components in parallel and then combining them as shown in Fig. 5.4 allows us to tune all three elements of the control system individually, providing for an optimal transfer function of the feedback loop [29].

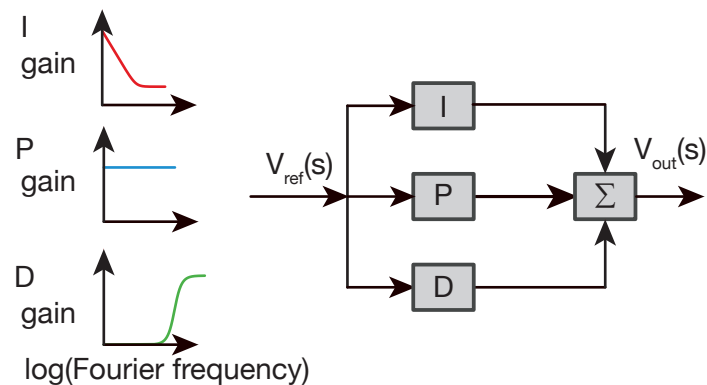


Fig. 5.4 Schematic of a PID-controller. The error signal from the double balanced mixer is weighted by a proportional element P, an integral element I and a derivative element D with the transfer functions indicated on the left. The signal from the three linear elements is combined on the combining element Σ of the fiber noise cancellation.

To obtain a good phase-stabilization of the VCXO to the VCXO, the PID-controller must follow specific requirements. In the following we describe the design of our PID-controller.

Integrator The error signal of the double balanced mixer is a constant value if the frequency of the VCXO and the beat signal is different. To phase stabilize the beat signal to the VCXO the constant offset voltage must be reduced. To do that very quickly, the PID-controller has an integral element, which amplifies small frequency error signals more than high frequency elements. The integral element is implemented by a non-inverting operational amplifier as described in Sec. 3.2.2. For DC-signals the phase delay of the integrator goes to 0° , such that the VCXO and hence the beat signal tracks the VCXO without phase delay (except for electronic phase delays).

Design aspects for the choice of the operational amplifier are low pink frequency noise, which describes the noise on the integral element of the PID-controller for

small frequency and is proportional to $1/f$, where f is the Fourier frequency of a signal ($1/f$ noise processes are described in Sec. 2.3). For our loop filter we need the operational amplifiers to have low noise specifications to keep the overall noise induced by the loop filter as low as possible. For the integrator especially low $1/f$ -noise is important since for higher frequencies the P and the I element have a higher gain. Furthermore the operational amplifier should have a high bandwidth to also amplify higher frequency noise and support the P and the I element. We decided to use the operational amplifier AD8675 (Analog Devices) as the integrator element in our loop. The AD8675 is a low voltage noise amplifier especially in the low frequency regime between 1 Hz and 10 Hz [41].

Derivative element The derivative element of the PID-controller lets high frequency components of the input signal pass the system while it blocks low frequency components of the input signal. In our PID-control the derivative element is implemented as first order high pass filter consisting of a capacitor. This capacitance value can be varied to optimize the transfer function.

Proportional element To change the transfer function for mid frequencies - frequencies between the cutoff frequency of the integrator and the cutoff frequency of the derivative element - we can place a proportional element. The simplest proportional element is a resistor, after which the transmitted voltage drops depending on the resistance value. However, for our circuit we did not use a proportional element. Nevertheless, if needed, the circuit allows to place a resistor parallel to the integrator and the derivative element.

Combiner Both signals from the integrator and the derivative element are summed in the combiner. The combiner is implemented as a operational amplifier in inverting configuration as described in Sec. 3.2.3. The transfer function of the combiner should amplify the low frequency components of the input signal pre-amplified by the integrator and also amplify the high frequency components transmitted by the proportional element. The bandwidth of the operational amplifier chosen determines the overall loop filter bandwidth. Operational amplifiers with a high bandwidth typically have higher $1/f$ noise figures than operational amplifiers as the LM6626 (Texas Instruments) used for integrators [42]. Hence we want to limit the gain of the operational amplifier for small frequencies where the amplification of the integrator dominates. For our combiner we used the operational amplifier in inverting configuration as described in Fig. 3.5.

The output signal obtained from the loop filter is fed into the modulation input of the VCISO. The VCISO does not directly drive the AOM but is frequency divided and amplified.

5.4.4 Frequency Divison and Amplifier

Once phase stabilized, the VCISO oscillates at the same frequency as the beat signal on the in-loop photodetector. However, the PI-loop modifies the error signal such that it adds twice the compensation phase shift to the signal at twice the frequency of the AOM. Since the light from the laser passes the fiber on it's way to the atoms only once, we need to compensate only for one phase noise shift $\phi_{EOM}(t)$. Hence, we divide the output frequency of the VCISO by factor 2 in the digital frequency divider and actuate the AOM with the frequency (and phase shift) halved output signal from the VCISO

$$V_{VCISO/2}(t) = V_{VCISO/2}[ft + \phi_{AOM}(t) + \phi_{EOM}(t)]. \quad (5.8)$$

The output signal of the frequency divider gets amplified in an AOM-driver and then drives the AOM.

After understanding the feedback loop of the fiber noise cancellation system we now want to characterize the system.

5.5 Characterization of the Fiber Noise Cancellation System

Using the optical setup described in Fig. 5.2 we can generate noise on the fiber interference arm of the system with the fiber EOM. On the out-of-loop photodetector we see a beat signal of the fiber interference arm with the unperturbed laser. If we generate noise with the fiber EOM on the fiber interference arm, the spectrum of the beat on the out-of-loop photodetector broadens. With the fiber noise cancellation we can actively compensate for the broadening of the beat signal. The compensation effect of the fiber noise cancellation against spectral broadening induced by fiber noise can be measured with the test setup described in Fig. 5.5. Using the electronic test setup we can quantify the bandwidth and the noise suppression of the fiber noise cancellation system.

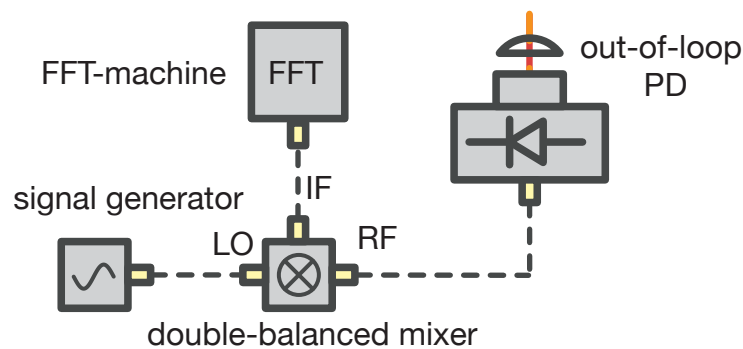


Fig. 5.5 Electronic setup for the test of the fiber noise cancellation. The beat signal with beat frequency f on the out-of-loop photodetector is mixed down to DC with a signal generator oscillating at frequency f and a double balanced mixer. The intermediate frequency port of the double balanced mixer is monitored on a fast fourier transform machine.

The out-of-loop photodetector beat signal at frequency f is mixed down with a reference oscillator, which is also oscillating at frequency f . The so obtained signal is monitored on a fast fourier transform (FFT) machine (SRS SR760 FFT Spectrum Analyser). With the FFT machine we can measure the power spectral density of the mixed down beat signal. The beat signal encodes the generated phase noise from the fiber EOM. Hence we can detect the phase noise generated by the fiber EOM on the out-of-loop photodetector. Comparing the power spectral density on the out-of-loop photodetector when the EOM is modulated and when the EOM is not modulated we can calculate a suppression of noise that the fiber noise cancellation can achieve. Modulating phase noise at different frequencies allows us to measure the bandwidth of the loop, which corresponds to the frequency at which the suppression of noise decreases by 3 dB.

In Fig. 5.6 we modulated frequency noise at a single frequency on the optical fiber and analyzed the effect of the fiber noise cancellation to the perturbation. The single frequency noise is detected on the FFT machine and averaged over 5 power spectra. This averaging is done for all further plots in this Section.

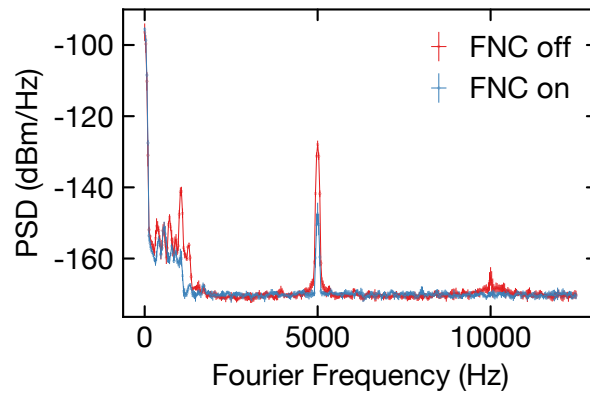


Fig. 5.6 Plot of phase noise on the out-of-loop photodetector from single frequency modulation at a frequency of 5 kHz and a voltage of 100 mV on the EOM. The plot shows the power spectral density of the the mixed down signal of the out-of-loop photodetector. The peak height of the baseband frequency noise peak with fiber noise cancellation is 20 dB suppressed with respect to the peak height without fiber noise cancellation turned on.

The fiber noise cancellation reduces the peak height of the noise generated at a frequency of 5 kHz and a voltage of 100 mV on the EOM by approximately 20 dB. When measuring the suppression of noise peaks at different frequencies we observe a decrease of the suppression of noise of the fiber noise for higher frequencies as can be seen in Fig. 5.7.

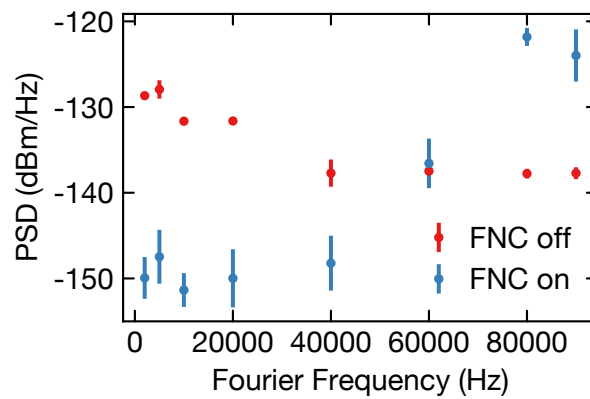


Fig. 5.7 Comparing the effect of fiber noise cancellation on the peak height of single frequency modulation at different frequencies. The peak height of the single frequency modulation at different frequencies in the case that fiber noise cancellation is activated (blue) and deactivated (red) is shown.

We can see that the fiber noise cancellation is more effective for low frequency modulations. A frequency modulation of the EOM can be compensated by 20 dB in this regime. The effect of fiber noise cancellation decreases and eventually inverts for high frequencies above 60 kHz. Subtracting the peak heights with and without fiber noise cancellation and plotting them on a logarithmic frequency as in Fig. 5.8 lets us compare the effect of the fiber noise cancellation for high frequencies with a low pass filter.

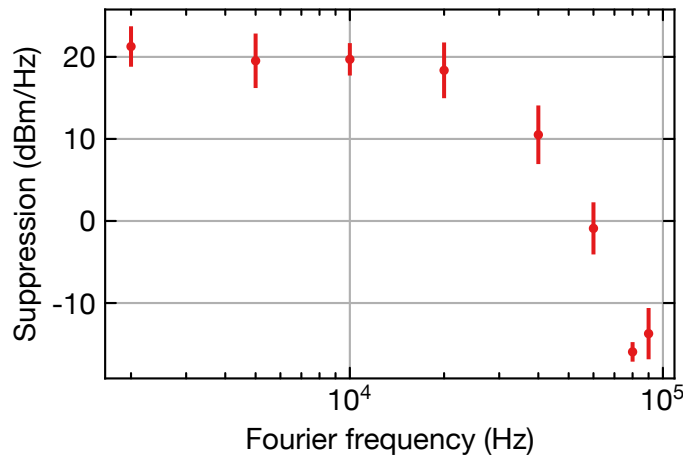


Fig. 5.8 Plot of the suppression of frequency noise by the fiber noise cancellation system. The frequency modulation peak height without and with fiber noise cancellation is subtracted and plotted on a logarithmic Fourier frequency scale. We can approximate the bandwidth of the loop to be roughly 20 kHz.

The gain of the fiber noise cancellations decreases for higher frequencies. Drawing the analogy to a low-pass filter we can approximate a cutoff frequency from Fig. 5.8 of $f_{\text{cutoff}} \approx 20$ kHz. Describing the fiber noise cancellation system as a low pass filter for noise, the gain of the overall system breaks down after the frequency f_{cutoff} . For higher modulation frequencies the fiber noise compensation signal picks up a phase delay with respect to the beat signal on the out-of-loop photodetector. If the phase delay approaches $\phi_{\text{delay}} = \pi$, the fiber noise cancellation compensation is out of phase with the generated noise and will drive an oscillation inducing more noise on the system. Hence, the suppression of the fiber noise cancellation system can become negative.

fiber noise cancellation signal can stimulate noise on the system since it is out of phase with it.

5.6 Future Improvements of the Fiber Noise Cancellation System

In this chapter we presented the design and a test of the first version of the fiber noise cancellation printed circuit board (PCB). The system consists of two PCBs: one PCB where both the VCXO and the VCSO are soldered on. Additionally, this PCB supplies for frequency dividing the output of the VCSO. The other PCB contains the RF-limiter, the mixer and the loop filter.

Bandwidth of fiber noise cancellation The fiber noise cancellation has a bandwidth $f_{\text{cutoff}} \approx 20$ kHz and a suppression of noise within the bandwidth of the loop of approximately 20 dB. With this suppression we can damp acoustic noise in the environment very well. However, the VCSO of the fiber noise cancellation has a modulation bandwidth of 150 kHz. Hence, the loop filter of the fiber noise cancellation can be further optimized by changing the loop filter elements.

Crosstalking of the two oscillators With two oscillators on one PCB we saw crosstalking of the reference oscillator and the compensating oscillator. This was observed as low frequency noise on the power spectral density of the two oscillators. There were spurious peaks at the difference frequency of the two oscillators. Crosstalking between the two oscillators can be reduced by separating the oscillators as much as possible, i.e. by placing them on different PCBs and also shielding them with electromagnetic shielding.

Low frequency noise The fiber noise cancellation system has not yet been optimized for low frequency noise characteristics. In Fig. 5.6 we can see low frequency noise at around 1 kHz that the fiber noise cancellation can not compensate for. It is likely that the low frequency noise is generated in the amplifier, a standard AOM driver. Hence, the reason of the low frequency noise should be further investigated.

The fiber noise cancellation PCB can also be used for low noise phase locks. With this setup we can for example damp vibrations in the laboratory between two fibers of a laser going to two different places in the optical setup. A simple way to implement this noise damping scheme is to replace the retroreflector of the zeroth order of the AOM (see Fig. 5.2) with another fiber (called zeroth order fiber), where we retroreflect a part of the electric field at the other side of the fiber. The phase-locked loop will be able to reduce the incoherent noise on light passing the two fibers to common mode noise. The fiber noise cancellation system then controls the noise power spectral density of the light going through the first order fiber such that it matches the noise power spectral density of the light going through the zeroth order fiber.

Chapter 6

Stability Analysis of the First-generation Cavity

The phase-locked loops described in Cha. 3 are able to phase-stabilize a laser to a reference laser. However, this technique can only improve the phase noise of the laser to the limit of the reference laser. The Pound-Drever-Hall locking scheme instead allows to transfer the stability of an optical resonator to a laser. Optical resonators can be very frequency-stable such that their fractional frequency fluctuations $\Delta\nu$ at room temperature can be pushed down to be on the order of [32]

$$\frac{\Delta\nu}{\nu} = 10^{-15}, \quad (6.1)$$

which was the design goal for the first reference cavity in the Strontium laboratory.

Prior to the start of my project in the Strontium laboratory, two master students had already worked on the first iteration of a reference cavity. Nejc Janša designed the vacuum chamber and the components inside the cavity responsible for mounting the optical resonator and shielding it from the environment [32]. Stephan Wissenberg took over the project after Nejc finished his thesis and assembled and locked the red MOT (Magneto Optical Trap) laser to the finished cavity [43]. The full reference cavity system built by Nejc and Stephan will be referred to as the first-generation cavity in the next Sections. The first-generation cavity is our current reference cavity for the experiment, i.e. both the red MOT and the clock laser are locked to this cavity. However, we had a few problems with the first-generation cavity:

We encountered a degradation of the finesse of the optical resonator which we attributed to outgassing processes in the vacuum chamber when vacuum baking the vacuum chamber. After changing the mirrors of the optical resonator we reassembled the cavity but we did not turn on the heaters on the inside of the vacuum chamber, to which Stephan attributed the finesse degrading process [43]. An additional problem of the first-generation cavity was a sudden pressure rise in the vacuum chamber to 10^{-3} mbar. After pumping out the vacuum chamber again, we only reached a pressure of 10^{-6} mbar.

However, we decided to build a new reference cavity with an improved design to circumvent the problems of the first-generation cavity.

In the beginning of this Chapter we will understand how a laser can be referenced to an optical resonator. It will become clear that an optical resonator must be well isolated

from its environment to obtain frequency-stable resonances. We then describe an actively temperature-stabilized wood box that shields the cavity from the environment. Finally, we compare the frequency fluctuations of the first-generation cavity to the fluctuations of the environment and see that the frequency fluctuations of the first-generation cavity can be mainly attributed to temperature fluctuations.

First we summarize the basics of optical resonators.

6.1 Optical Resonators

As discussed in Sec. 2.4.1, the solutions of an electric field in a one-dimensional optical resonator are given by

$$E(r, k_q) = E(t) \sin(k_q r), \quad (6.2)$$

where k_q can only take the values

$$k_q = \frac{\pi q}{L}, \quad (6.3)$$

with the length L of the cavity and the discrete number of modes q . The electric field $E(t)$ obeys the dispersion relation of an electromagnetic wave in vacuum $\nu = ck/2\pi$. Hence we can express the resonant frequencies of the cavity as

$$\nu_q = q \frac{c}{2L}, \quad (6.4)$$

where c is the speed of light. Resonant modes of the cavity are spaced by a free spectral range defined as $\nu_{\text{FSR}} = c/2L$.

The optical resonances can be further described by their finesse F . This quantity gives a measure for how strict the condition from Eqn. (6.3) for real resonators is. An optical resonator consists of two mirrors M_1 and M_2 with high intensity reflectivities $R_1 = R_2 = R$ and low transmission coefficients $T_1 = T_2 = T$, spaced by the distance L . Light with the electric field $E(r, \nu)$ is coupled into the resonator through one of the two mirrors. The light wave between the two mirrors travels from mirror M_1 to mirror M_2 . When reaching mirror M_2 , the ratio R of the electric field will be reflected and travels back to mirror M_1 while the transmission ratio T of the electric field will be transmitted through mirror M_2 . In Fig. 6.1(a) this process is shown.

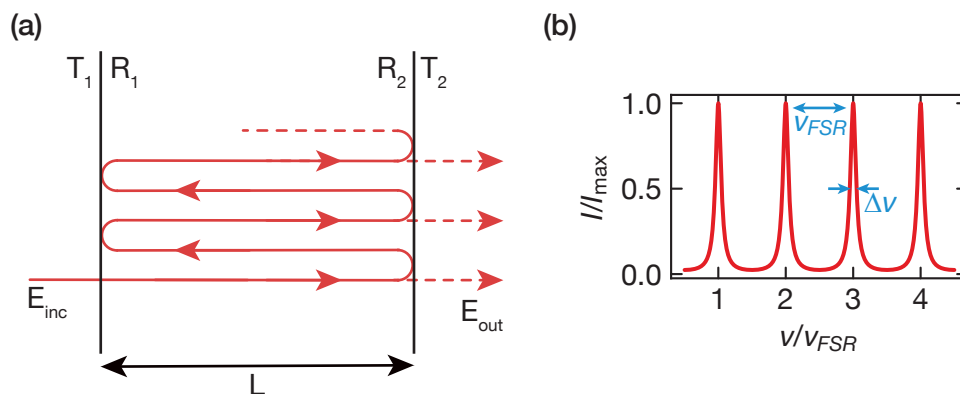


Fig. 6.1 Transmission through a cavity. (a) A cavity consists of mirrors $M_{1/2}$ with transmission and reflectivity coefficients $T_{1/2}$ and $R_{1/2}$ respectively. The mirrors are separated by length L . The reflected light at a mirror is represented by a red solid line. The transmitted light is represented by a dashed line. The half circle that the electric field undergoes when being reflected is only for illustration purposes. In reality the light beam overlaps with its reflected counterpart. (b) The transmission peaks through a cavity with finesse 50 when scanning over several free spectral ranges. Figures (a) and (b) adapted from Ref. [20].

This process repeats an infinite amount of times. A steady state will be reached when the transmitted light reaches a constant value. Since the electromagnetic waves will be reflected from both mirrors M_1 and M_2 an infinite amount of times, the electric field can be summed up using a geometric series to obtain the light intensity in the resonator [20]

$$I(\nu) = \frac{I_{\max}}{1 + (2F/\pi)^2 \sin^2(\pi\nu/\nu_{\text{FSR}})}. \quad (6.5)$$

Here I_{\max} is the maximum intensity coupled into the optical resonator on resonance and the finesse is approximated as [20]

$$F = \frac{\pi\sqrt{R}}{1 - R}, \quad (6.6)$$

for $F \gg 1$. Equation (6.5) has the form of an Airy function and is plotted in Fig. 6.1(b). Hence, the finesse is a scaling factor for the Airy function's spectral width of the resonance frequency of an optical resonator. The higher the finesse of an optical resonator, the narrower the resonance frequencies. The spectral width of an optical resonator can be approximated by

$$\Delta\nu_{\text{FWHM}} \approx \frac{\nu_{\text{FSR}}}{F}. \quad (6.7)$$

As the finesse is a measure of the reflectivity of the mirrors, we can obtain the finesse of a resonator by measuring the transmitted power from the cavity after turning off the light beam coupled into the cavity. In this case the system will not be in a steady state anymore, and the light intensity stored in the cavity will be decreased at each mirror

by a factor $(1 - R)$. The reduction of the stored light intensity leads to a differential equation

$$\frac{dI(t)}{dt} = -\frac{c}{L}(1 - R)I(t), \quad (6.8)$$

which describes the loss of intensity of the electric field in the cavity. The solution to this differential equation is an exponential decay $I(t) = I_0 \exp(-t/\tau)$. Relating the time constant of the decay of the light intensity $\Delta\nu_{\text{FWHM}} = 1/(2\pi\tau)$ to the spectral width of the resonance one can thus calculate the finesse from the characteristic time constant τ of the optical resonator by using Eqn. (6.7) as

$$F = \frac{\pi c\tau}{L}. \quad (6.9)$$

The discussion in this Section was made using principles from ray optics only. However, real-world cavity modes are described by Hermite-Gauss-modes of light, which are described in Ref. [43]. However, the description of the allowed modes and the finesse of an optical resonator using Hermite-Gauss-modes (see e.g. [20]) agrees with the ray optics approach for our purposes.

6.2 Design Criteria for the Reference Cavity Housing

A high-finesse optical resonator transmits only light within a very narrow frequency spectrum around its resonance. The Pound-Drever-Hall locking technique for lasers uses this characteristic feature of an optical resonator to stabilize lasers. The principles of this technique are described in Cha. 8. However, to understand the design choices for an optical resonator we want to anticipate the slope of the error signal ϵ of the Pound-Drever-Hall locking technique around resonance. It is defined as [1]

$$\epsilon = \frac{-16F\sqrt{P_c P_s}L}{c}(f - f_R), \quad (6.10)$$

where P_c and P_s are the optical powers in the carrier and the sideband respectively, f is the frequency of the laser, and f_R is the frequency of the cavity resonance. Hence we need a high-finesse cavity to obtain a steep error signal. By using an error signal with a steep slope the PI loop is able to keep the laser very frequency-stable since the ratio of signal to electronic noise of the PI loop is then higher. Equation (6.10) also suggests that the distance between the two mirrors of the cavity should be long.

Another design consideration to make for a reference cavity is the stability of the resonance. The resonance frequency of an optical resonator should not drift over time, so that one can always be sure that one locks a laser to the exact same frequency. The resonance frequencies of the optical resonator are connected to the length difference between

the mirrors via Eqn. (6.4). However, real optical resonators cannot be operated in perfect vacuum conditions. Hence, we must include a possible modification of the refractive index n in Eqn. (6.4) such that it transforms to

$$\nu_q = q \frac{c}{2Ln}. \quad (6.11)$$

Using this relation a laser's frequency noise can be traced back to the noise on the length and the refractive index of the optical resonator. We will discuss several possible causes for a length instability of the optical resonator.

6.2.1 Pressure Fluctuations

Looking at Eqn. (6.11) we express the frequency fluctuation as a fluctuation of the refractive index

$$\frac{\Delta\nu}{\nu} = -\frac{\Delta n}{n} \quad (6.12)$$

of the vacuum in between the two cavity mirrors. The change in refractive index effectively changes the optical path length $L_{\text{opt}} = L_{\text{abs}}n$ from the absolute path length. Approximating the remaining gas in the vacuum chamber as nitrogen we can express the fractional change of the index of refraction for a given pressure change ΔP in mbar at 30°C as [1, 32, 43]

$$\frac{\Delta n}{n} = 2.65 \times 10^{-7} \Delta P. \quad (6.13)$$

Hence, we need to stabilize the pressure of our optical resonator to a level of approximately 10^{-8} mbar to obtain a frequency uncertainty of 10^{-15} .

6.2.2 Temperature Fluctuations

Temperature fluctuations change the frequency of an optical resonator just as pressure fluctuations do. For a temperature fluctuation, the length of an ultra low expansion (ULE) spacer, separating the two cavity mirrors, will change if the temperature of the system. The length difference can be approximated in first order by

$$\frac{\Delta\nu}{\nu} = -\frac{\Delta L}{L} = -\alpha_{\text{CTE}} \Delta T, \quad (6.14)$$

where the coefficient of thermal expansion (CTE)

$$\alpha_{\text{CTE}} = \frac{1}{L} \frac{dL}{dT} \quad (6.15)$$

is defined as the coefficient which determines the fractional change in length of the optical resonator per K. ULE glasses typically have a zero crossing temperature. At this temperature, the coefficient of thermal expansion vanishes. Hence, one should temperature-stabilize optical resonators to the zero crossing temperature. For ULE glasses the CTE can be approximated around the zero crossing temperatures as [44]

$$\alpha_{\text{CTE}}(T) = a(T - T_0) + b(T - T_0)^2. \quad (6.16)$$

For ULE glasses the coefficients a and b typically take the values [44]

$$a \approx 1.8 \times 10^{-9} \frac{1}{\text{K}^2} \quad (6.17)$$

$$b \approx 10 \times 10^{-12} \frac{1}{\text{K}^3}. \quad (6.18)$$

Due to the small a and b coefficients ULE is ideally suited for the spacer material, which maintains the length distance between the two mirrors of the optical resonator.

Looking at Eqn. (6.18) one must temperature stabilize the optical resonator to a level of less than 1 mK to obtain a fractional frequency uncertainty of 10^{-15} when heating or cooling the optical resonator to the zero expansion temperature T_0 .

Heat can be transferred between two solid components either via conductivity or via radiation. To minimize heat transfer from the environment to the optical resonator, using thermal shields has proven to be a suitable strategy [45]. Thermal shields act as low-pass filters for thermal fluctuations. Reference [32] made an analogy of heat flow to electrical currents. We also use this analogy where the temperature difference of two system corresponds to the voltage difference between two systems and the electrical current corresponds to the heat flow

$$P = \frac{dQ}{dt}, \quad (6.19)$$

where P is the thermal power transfer of a body to the environment. We express the heat capacity of a thermal system as

$$C = \frac{Q}{\Delta T} = mc, \quad (6.20)$$

where m is the mass of the capacitance and c is the thermal conduction coefficient. The resistance between two bodies is given by

$$R = \frac{\Delta T}{P}. \quad (6.21)$$

We now want to understand how we should design our system to have good low pass filter properties to isolate the optical resonator from any fluctuations. If a temperature fluctuation heats up the heat shield at one spot, a high thermal conductivity of the heat

shield can distribute the temperature fluctuation over the whole heat shield. Furthermore, if the heat shield is connected with a low contact resistance to a heat sink, which is assumed to be at equilibrium, then the temperature fluctuation will transfer to the heat sink. The heat capacity of the heat shield gives a time constant of this process. However, this is not the only possible process. The heat shield can also transfer the temperature fluctuation either via conduction or radiation to the optical resonator. This rate is determined by the thermal resistance R . The thermal resistance R_{con} for conduction and radiation processes is defined as [32]

$$R_{\text{con}} = \frac{d}{\kappa A}, \quad (6.22)$$

and depends on the thermal conductivity κ , the cross section A , and the thickness d of the material for conduction processes. For radiation processes between two bodies stacked in each other, the thermal resistance depends on the emissivity, the temperature and area of the two bodies. The thermal resistance is small for high emissivities of the two bodies and gets larger if one of the two bodies has a smaller emissivity coefficient [45]. For a strong damping of high frequency processes, the heat should flow from the heat shield to the heat sink, while it is not transferring any heat power to the optical resonator. Hence, the thermal conductivity should be high, the emissivity of the heat shield and of the optical resonator should be small, and the optical resonator should not be in contact with the heat shield to avoid heat conduction.

6.2.3 Vibration Fluctuations

An optical resonator in a laboratory environment is exposed to different kinds of vibrations and acoustic noise, for instance from a turbo pump or from a chiller of a laser. The length change of a cavity resulting from any vibrations induced on the cavity can be expressed as [46]

$$\frac{\Delta L}{L} = \mathbf{k} \cdot \mathbf{a}, \quad (6.23)$$

where \mathbf{a} is the acceleration vector and \mathbf{k} is the vibration sensitivity of the optical resonator. For horizontally mounted optical resonators one can find support points of the cavity that minimize the the vibration sensitivity to smaller than $\frac{\Delta L}{L}/k_{x,y,z} = 10^{-11}/(\text{ms}^{-2})$ [46]. However, even if the mounting structure allows for a very good vibrational insensitivity, we also want to minimize the vibrational accelerations on the optical resonator, as the accelerations should be slower than $10^{-4}(\text{ms}^{-2})$ to achieve a fractional frequency stability of 10^{-15} .

Knowing how the environment influences the resonance frequency of the optical resonator, we can now analyze the thermal environment of the first-generation cavity. Since we cannot temperature-stabilize the copper box of the first-generation cavity, it is especially important to shield the first-generation cavity from external temperature fluctua-

tions. Hence we built an actively temperature-stabilized wood box around the vacuum housing of the first-generation cavity.

6.3 Active Temperature Stabilization of Outside of the Aluminum Cavity

A picture of the wood box assembled around the cavity is shown in Fig. 6.2.

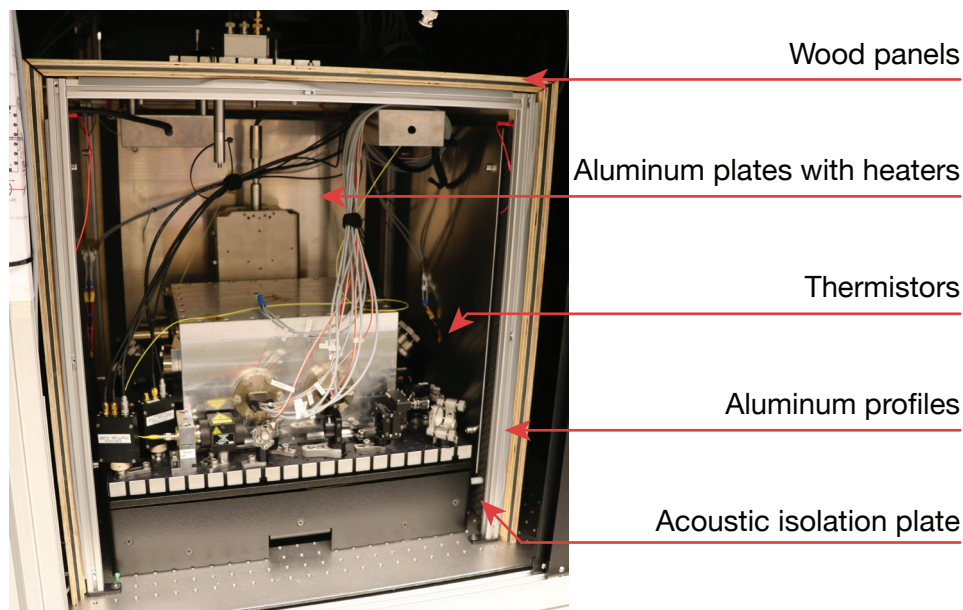


Fig. 6.2 One side panel of the wood box is open. The wood box is mounted on an aluminum profile. Acoustic shielding rubber plates are glued on the panels to obtain maximum acoustic isolation properties. On the wood panels aluminium plates are mounted via stainless steel posts. The aluminum plates are servoed on with a PI loop which uses the thermistors attached to the aluminum panels on the right and left side of the box as sensors.

The wood box consists of 16 mm thick acoustic isolation wood BaryVam. Acoustic shielding rubber plates are glued on the panels to obtain maximum acoustic isolation properties. Furthermore, the aluminum plates are mounted with steel posts on the wood plate with two radiative Kapton heaters attached to the back of the plate. The high thermal conductivity of aluminum allows the heat to be radiated onto the cavity homogeneously. The active temperature stabilization of the wood box is split into two different PI loops, the right side of the cavity (when looking at Fig. 6.2) and the left side. The reason for this is the big hole on the top of the wood plate for the cables that need to go out of the wood box. Hence, the right side of the wood box needs more heating power to be servoed to the same temperature as the left side of the box.

To estimate the effect of the wood box as a heat shield we compared the temperature fluctuations of the thermistors on the copper box inside the aluminum chamber with the fluctuations of the outside temperature. This was done for a time interval from March to September in 2018, when the wood box was not yet placed and a time interval in 2019 from March to September, when the wood box was placed and the PI loop was working. The time interval was chosen such that an air conditioning breakdown in Fall 2018 was not considered in this measurement.

To analyze the temperature data we computed the overlapping Allan deviation (OADEV) of the temperature data, which is computed from the standard Allan variance [47]

$$ADEV_T^2(\tau) = \sigma_T^2(\tau) = \frac{1}{2(N-2)\tau^2} \sum_{i=1}^{N-2} [T_{i+2} - 2T_{i+1} + T_i]^2, \quad (6.24)$$

where T_i is the temperature data at a specific time t_i and N is the number of temperature points T . By averaging over all possible temperature-time combinations for one averaging interval τ we get the overlapping Allan variance OAVAR of the temperature data. Taking the square root of the overlapping Allan variance gives the overlapping Allan deviation OADEV. This measure allows us to identify periodic processes in the temperature data. Periodic processes with period τ will average when computing the Allan deviation for the averaging time τ . Hence, dips of the overlapping Allan deviation for specific time intervals indicate periodic processes with the same periodicity that influence the temperature. An overall smaller value of the overlapping Allan deviation indicates a smaller variance of the temperature, i.e. the system is less exposed to temperature fluctuations.

We compared the periodicity of temperature perturbations on the cavity by looking at the overlapping Allan deviation of one of the sensors on the copper box inside the cavity for the two time intervals in 2018 and 2019. Additionally we plotted the overlapping Allan deviation of the temperature fluctuation on the outside of the wood box and on the actively servoed thermistor on the aluminum plate. The overlapping Allan deviation has dips for averaging times which coincide with the periodicity and multiples of the periodicity of a perturbation. Looking at the trace of the ambient temperature fluctuation in the year 2019 in Fig. 6.3,

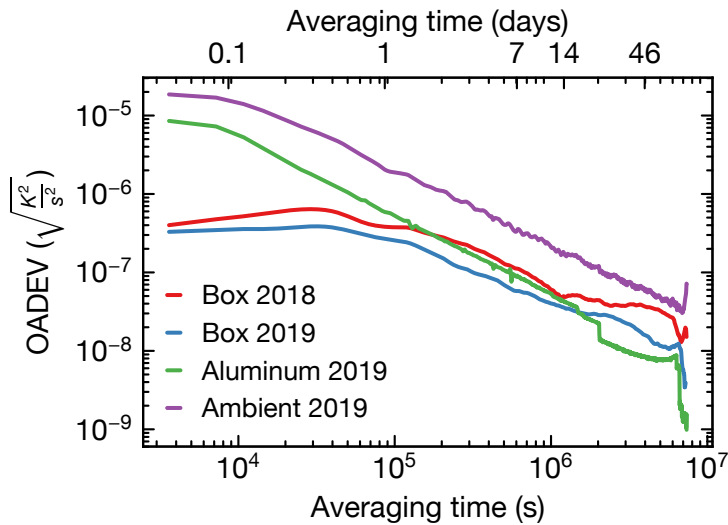


Fig. 6.3 Plot of the overlapping Allan deviation OADEV of the ambient temperature and the temperature inside the cavity.

we can see that the ambient temperature has a dip over the course of roughly one day. This daily periodicity is almost not visible anymore on the sensor on the aluminum plate. The PI loop cancels the temperature fluctuations with a characteristic time constant much smaller than one day. The copper box on the inside of the cavity saw the daily temperature fluctuations in 2018, as can be seen from the dip very clearly. The Allan deviation over a time interval shorter than a day is damped due to the low pass filter characteristics of the aluminum chamber as a heat shield. However, over longer time periods the copper follows temperature drifts from the environment as can be seen by the higher Allan deviation value of the copper box than the PI box. The Allan deviation of the copper box in the time interval 2019 is constantly lower than the time constant of the copper box in the year 2018. Especially in the regime of one day, the averaging dip is less visible. Therefore daily temperature fluctuations have a reduced effect. In the mid term regime of 1 day to 2 weeks the PI controlled wood box limits the Allan deviation of the copper box while in 2018 the temperature was less stable on this timescale. Over long timescales of 1 month and more the PI loop can not regulate the temperature of the cavity anymore. This we attribute to external influences like a higher humidity of the laboratory in Summer, which leads to a higher thermal conductivity of air and therefore to increased temperature fluctuations. To interpret this data it is also important to know that the doors surrounding the optical table were not used in the time frame in 2018, while they were almost always closed in the time frame 2019. This change must also be considered when comparing the datasets. However it becomes clear from the plot, that the active temperature stabilization improves the temperature stability of the cavity over short and mid time frames.

With the wood box set in place, we can analyze the frequency fluctuations of the resonances of the cavity.

6.4 Resonance Frequency Drift of the Cavity in the Aluminum Housing

Using the expressions for the frequency-dependence of the resonance frequency we can now understand the drifts of the first-generation cavity by referencing the cavity resonance to the reference in the atoms. Strontium has a narrow 1S_0 - 3P_1 transition (red MOT transition), which is used as the second stage of a two stage MOT sequence (a detailed description of our MOT setup and sequence can be found in Refs. [32, 48]). To stabilize the red MOT laser to the transition we set up a Pound-Drever-Hall frequency-stabilization (see Cha. 8) to the resonance of the optical resonator, which is close to the 1S_0 - 3P_1 transition. We further implemented AOMs in double-pass configuration [49] to frequency shift the red MOT laser's frequency to the 1S_0 - 3P_1 transition of the atoms. Due to the 1S_0 - 3P_1 transition's narrow linewidth of 7.4 kHz, tuning the red-MOT laser's frequency to obtain maximum atom number is an accurate measure for the optical resonator drift over time.

In the following we analyzed the maximum atom number of the red MOT of the fermionic isotope ^{87}Sr in the time interval between April and August 2019. In the red MOT sequence we use a stirring laser beam to maximize the atom number in the red MOT. The stirring laser beam shuffles the populations of the hyperfine states of ^{87}Sr in the red MOT (see Ref. [50] for a detailed description of the laser cooling of ^{87}Sr). We shift the frequency of the stirring laser beam with a direct digital synthesis (DDS) device connected to an acousto-optic modulator in double-pass-configuration.

In Fig. 6.4(a), a plot of the stirring laser's DDS frequencies f from April to August 2019 is shown.

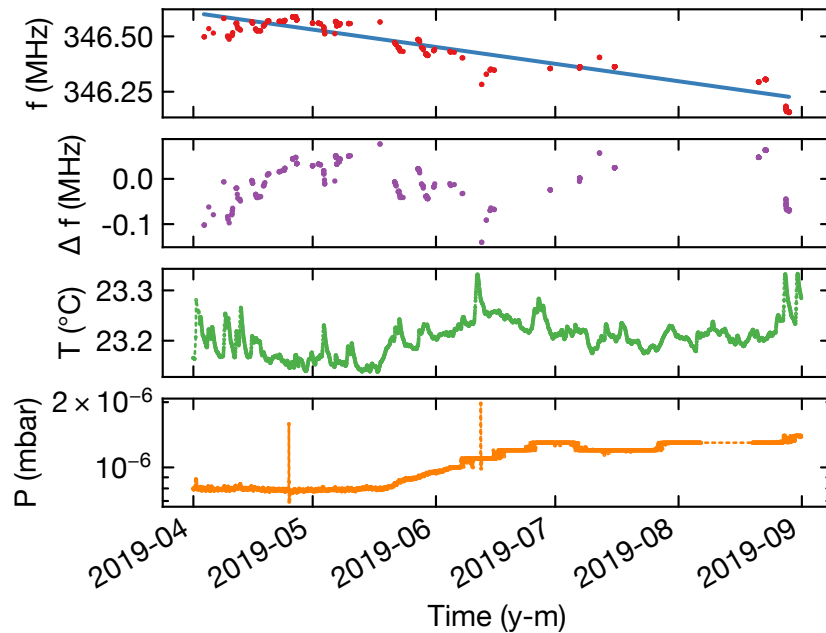


Fig. 6.4 Analysis of the Resonance Frequency Drift of the Aluminum Chamber. (a) The frequency f of the DDS channel controlling the frequency of the stirring laser beams is plotted against the time. From a linear fit on the drift of the frequency f we obtain a drift rate of $-29.6(6)$ mHz/s. (b) The fitted drift rate of the optimized atom number is subtracted from the resonance frequencies to be able to correlate the frequency changes to external influences. (c) Plot of the temperature of a thermistor inside the cavity housing against the time. (d) Plot of the pressure at the ion pump inside the vacuum chamber against time. The jumps of the pressure are caused by the pressure measurement accuracy of the ion pump for pressures above 10^{-6} mbar. Also the logging of the pressure was turned off in August (indicated by the dotted line).

The DDS frequency f drifts linearly over time. This drift is caused by an ongoing crystallization of the glass of the optical resonator. For ULE glasses this drift is specified to be on the scale of $\Delta L/L \approx 10^{-16} \text{ s}^{-1}$ [51], which corresponds to a frequency drift of 40 mHz/s for light with a wavelength of 689 nm. Fitting the linear drift of the DDS frequencies f gives a slope of $-29.6(6)$ mHz/s. Hence, our optical resonator drifts on a reasonable timescale. In Fig. 6.4(b) the drift of the cavity is removed from the DDS frequencies f . The so obtained drift-free DDS frequency variation $\Delta f \approx 150$ kHz can be correlated both to the pressure in the cavity (shown in Fig. 6.4(d)) and to the temperature drift of the copper box T , which surrounds the optical resonator [shown in Fig. 6.4(c)]. The pressure increased over the observed time interval from April to August 2019 from 8×10^{-7} mbar to 1.3×10^{-6} mbar. However, this increase in pressure cannot account

for the big temperature drifts. Plugging in the overall pressure difference in this time interval into Eqn. (6.13) we obtain a frequency variation of 70 Hz over the whole time interval, which is much smaller than the observed frequency variation. Hence we can neglect pressure fluctuations as a cause for the resonance frequency fluctuations.

The temperature fluctuations in Fig. 6.4(c) can already be correlated to the frequency fluctuations of the DDS frequency by eye.

Using Eqns. (6.14) - (6.16) we can do a back of the envelope calculation for the magnitude of a frequency changes caused by fluctuations of the temperature of the aluminum vacuum chamber. Taking the zero crossing temperature of the optical resonator $T_0 = 33^\circ\text{C}$ [43] and using the a and b coefficients from Eqns. (6.17) and (6.18) we can calculate the frequency change caused by a 0.1°C temperature change at a wavelength of 689 nm to be approximately 700 kHz at an initial temperature of 23.2°C .

This frequency change is higher than the frequency change of 150 kHz which we observed for our cavity in Fig. 6.4(b). However, the zero expansion coefficient model from Eqn. (6.14) only holds close to the zero crossing temperature. Hence the model might not be accurate at 23.2°C . Nevertheless this approximation of frequency drifts lets us conclude that temperature drifts are the main cause for the frequency drifts of the optical resonator in the aluminum vacuum housing.

Chapter 7

Design, Assembly and Characterization an Optical Resonator Housing

In this Chapter we will explain the main design aspects of the second-generation cavity housing. We show and explain the assembly process of this cavity. Finally, we compare the thermal isolation properties of the second-generation vacuum chamber design to the thermal isolation properties of the first-generation.

7.1 Choice of the Optical Resonator and the Support Platform

We bought an optical resonator from Stable Laser Systems for our cavity. The ULE spacer of type 6020-4 Notched Spacer is 100 mm long. A plane mirror and a concave mirror with a radius of curvature of 500 mm are optically contacted to the two ends of the spacer. The cavity has a target finesse of $F = 300000$ for light with a wavelength of 698 nm. Stable Laser Systems measured the zero crossing temperature of the optical resonator to be $32.75^{\circ}\text{C} \pm 1^{\circ}\text{C}$. The notched optical resonator is mounted on a support structure made from Zerodur, a material with low CTE. The Zerodur support structure has $10 \times 10 \text{ mm}^2$ pockets for Viton pads on the top side and $4 \times 4 \text{ mm}^2$ mm pockets on the bottom side respectively. The Viton pads act as a vibration isolation. The pockets on top of the Zerodur spacer reference the position of the optical resonator to a position that is optimal to reduce vibrations of the resonator. The design of the support structure stayed unchanged from the first-generation cavity and is described in Ref. [32].

7.2 Design of a Steel-chamber Housing for an Optical Resonator

This Section describes the design of the second-generation Strontium laboratory reference cavity. To circumvent any vacuum problems we decided to build a stainless steel chamber vacuum housing with CF-flanges, which are suitable for ultra high vacuum applications. Another major design change was to exchange the Kapton heaters for Peltier

elements, as Peltier elements have proven to have outgassing rates low enough to obtain pressures on the order of 10^{-9} mbar [52]. We avoided using any other glue than Torr Seal, with which vacuum levels of 10^{-9} mbar can be reached.

A schematic of the stainless steel vacuum housing is shown in Fig. 7.1.

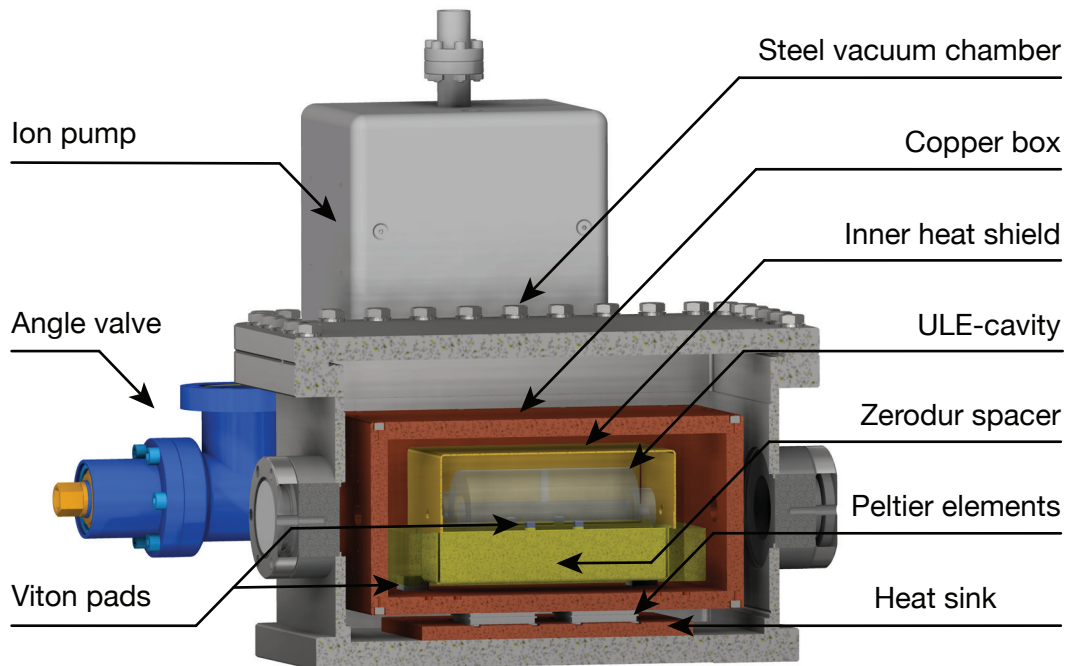


Fig. 7.1 Half section view of the stainless steel vacuum chamber of the reference cavity. The vacuum chamber contains an the copper box, which is standing on two Peltier elements. The Peltier elements are mounted on a copper plate acting as a heat sink for the Peltier elements. Inside the copper box the Zerodur holder of the cavity is standing on Viton pads. The second heat shield is laying on the Zerodur spacer and surrounds the ULE-cavity, which is mounted on the Zerodur spacer with Viton pads. Attached to the cavity are the ion pump and the angle valve.

7.2.1 Stainless Steel Vacuum Chamber

We decided to build the vacuum chamber from stainless steel of type AISI 304. It has good vacuum properties since stainless steel allows one to use copper CF gaskets with stainless steel parts. CF flanges can in principle reduce leak rates to less than 10^{-11} (mbar l s⁻¹) [53]. This vacuum sealing technique in combination with an ion-pump with a pump speed of the order of 10 L/s is in principle able to pump much below our specified target pressure of 10^{-8} mbar.

The vacuum chamber has five CF-40-flanges. The CF flanges are sealed with copper gaskets. Two of the flanges are needed for D-SUB-9 electrical feedthroughs for the wiring

of the Peltier elements. The electrical feedthroughs can not be seen in Fig. 7.1, as they are in the front of the cavity. On two of the other CF-flanges the viewports for the transmission of the light are mounted. The viewports are mounted exactly on the height of the cavity, such that the light coupling into the cavity enters the cavity directly through the center of the viewport. The glass of the viewports is angled with 0.5° with respect to the surface of the steel chamber and therefore to the surfaces of the mirrors such that no reflections between the inside of the viewport and the cavity can cause etaloning effects, i.e. a standing wave on the reflection signal from the cavity. The viewports are antireflection-coated on two wavelength intervals: They are coated in a blue wavelength interval around 450 nm and in a red wavelength interval from 675 nm - 700 nm. In these two intervals the reflection of light from the viewport is less than 0.5%. The fifth flange of the vacuum chamber connects the back of the vacuum chamber via a 5-way-cross to the ion pump (Agilent VaclonPlus 20 L/s), which pumps both noble gases and hydrogen and allows for vibration free pumping. One of the other flanges on the 5-way-cross is connected to the angle valve, where the turbo pump for the initial pumping process can be connected. The other two flanges of the 5-way-cross are connected to a blind flange and closed with a welding connection respectively. The lid is attached onto the steel chamber with a custom rectangular copper gasket.

7.2.2 Temperature Control of the Optical Resonator

The thermal conductivity of stainless steel of type AISI 304 is $\lambda_{\text{AISI 304}} = 16.2 \text{ W}/(\text{m}\cdot\text{K})$. This is a relatively low thermal conduction value compared to aluminum of type EN AW 5083 [$\lambda_{\text{EN AW 5083}} = 120 \text{ W}/(\text{m}\cdot\text{K})$]. A lower thermal conduction of the vacuum chamber makes the vacuum chamber a worse heat shield as discussed in Sec. 6.2.2. The copper box was polished with a high-gloss polish to obtain a very low emissivity coefficient. The inner heat shield was sent to plasotec GmbH to get it plasma polished. We assumed that we would reach the best emissivity coefficient of the copper parts by plasma polishing. Nevertheless, comparing the shininess of the inner heat shield and the copper box, the copper box seemed to be more shiny.

However, with a very stable active temperature control we should still be able to control the inner copper box to a stability of under 1 mK. The Peltier elements are ideally suited to react to both heating and cooling processes because they can both cool and heat an object. Peltier elements cool their cool side and the heat is dissipated on the hot side. We used the Peltier element TE-2-(127-127)-1.15 from TE Technology Inc. for our setup, since this Peltier element is vacuum compatible to pressures of less than 10^{-8} mbar [52]. The active temperature control uses the PI controller HTC1500-62 in combination with the PCB HTCEVALPCB from Wavelength Electronics and Omega 5500 $10 \text{ k}\Omega$ thermistors. The temperature of the thermistors is measured with a 4-wire resistance measurement with a Keithley Multichannel 2700 device.

For an optimal active temperature stabilization of the inner copper box we want the whole

copper box to be homogeneously heated. However, a Peltier element heats by conduction of heat and can only heat the copper box from one side because it must be properly heat sunk to the vacuum housing. We realized a good thermal contact between the Peltier element and the vacuum housing by placing the Peltier element on a copper plate. This copper plate is much bigger than the surface area of the Peltier element and ensures with its large surface area a low thermal conductive resistance between the Peltier element and the stainless steel chamber (see Eqn. (6.22)). In between the Peltier elements and the copper parts we placed a 0.1 mm thick indium foil. The surface of the indium foil is smooth and ensures a good thermal contact between the copper and the Peltier element even if the Peltier element's surface is not perfectly plane.

Because of the only very localized conductive heating of the Peltier elements, there will always be a temperature gradient over the copper box. To obtain an optimal temperature stability of the copper box we placed the thermistors on the copper box very close to the holes for the light to go through. Since these points are in the middle of the height of the copper box, the thermistors at these points see an average temperature of the copper box. Servoing on a setpoint close to here is supposed to minimize temperature fluctuations of the system.

7.2.3 Vibration isolation of the Steel-Chamber Cavity

To obtain an optimal vibration isolation performance, we decided to buy the vibration isolation platform 150 BM-8 from Minus-K Technology, which was chosen because of our weight estimation (estimated using Autodesk Inventor) of the cavity housing and components of ≈ 65 kg. Furthermore, the vibration isolation platform is large enough for our steel chamber cavity and optics needed to couple into the cavity. The vibration isolation platform has a vertical 0.5 Hz and horizontal 1.5 Hz natural frequency, respectively. Any vertical accelerations higher than 5 Hz are damped by 40 dB. Horizontal accelerations higher than 5 Hz are damped by 20 dB. The specifications named allow for accelerations smaller than 10^{-4}ms^{-2} .

7.3 Assembly of the Stainless Steel Chamber Cavity

7.3.1 Cleaning of the Vacuum Parts

All parts were cleaned according to the vacuum cleaning reference from Ref. [54] and Ref. [43]. However, some steps were changed. Hence we will take a look at the vacuum cleaning of the different parts.

Stainless Steel parts The machine shop had done a leak test of the chamber before the chamber arrived in the laboratory, where a vacuum level of 10^{-4} mbar was reached.

I washed the parts with deionized water, sonicated them in a Liquinox (from Alconox) soap solution at 50°C and rinsed them with acetone and with isopropanol. After washing the stainless steel parts we put them on aluminum foil in the oven and then baked them for 24 hours at 300°C.

Copper parts The copper box was very dirty after polishing it with paraffin sand paper. Paint thinner was used to wash off all residuals from the polishing procedure. This took several iterations and the venting holes had to be cleaned with Q-tips. Oxidized parts of the copper were treated with citric acid. After this initial cleaning process, we sonicated the copper parts, then we rinsed the copper parts with deionized water, with acetone, and then with isopropanol. We then put all copper parts in the oven on a layer of aluminum foil, flushed the oven with argon and baked at 130°C for 12 hours to avoid oxidizing the copper.

Viton pads The Viton pads were sonicated in a Liquinox soap solution and then washed with deionized water. Afterwards they were rinsed with isopropanol (not with acetone) and baked in the oven at 150°C for 16 hours to remove the adsorbed and absorbed water.

Electrical parts All electrical parts were washed off with deionized water and then sonicated in isopropanol. Especially the soldered connections were washed off with isopropanol very carefully.

Zerodur spacer The Zerodur spacer was rinsed with deionized water, acetone and isopropanol. We did not bake the Zerodur spacer as cooling the spacer too quickly might have degraded its thermal properties [32].

Viewports and ion pump and angle valve We blew nitrogen on the surfaces of the viewports. Apart from this we did not clean these parts.

After the baking procedure we put all parts in a vacuum bag that was flushed with argon. With this technique we tried to prevent the parts from adsorbing too much water molecules from the air. The baking process tries to dissolve them from the surface. Therefore leaving the baked parts in the air for some time reverses the baking process.

7.3.2 Assembly of the Inner parts of the Cavity

As a first step we soldered the Peltier elements in series with vacuum-compatible solder. We also prepared the electrical feedthrough vacuum side wires to not have accessibility problems when working in the steel chamber. After baking of the stainless steel chamber, we put the stainless steel housing on the vibration isolation platform. The center of mass position of the stainless steel chamber with everything attached was estimated using Autodesk Inventor. A picture of the the empty chamber is shown in Fig. 7.2(a).

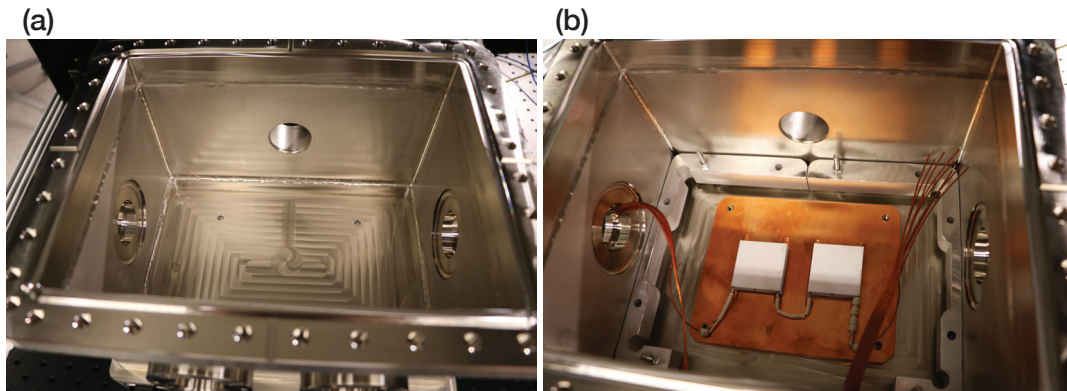


Fig. 7.2 (a) The empty steel chamber. (b) One of the copper sidewalls. One can see the blob of Torr Seal covering both the thermistor and the soldering connection to the wire.

The SUB-D-feedthroughs with Kapton insulated wires already attached were first connected to the chamber to be able to connect the Peltier elements directly. As a next step we mounted the copper heat sink plate with 3 set screws. However, it turned out that the heat sink plate was wobbling on the bottom plate of the chamber because its bottom surface was not plane. Thus we flattened the surface with sandpaper and put the heat sink back into the steel chamber (after another cleaning run). Then we placed the serially connected Peltier elements to the Kapton insulated wires. On the top and the bottom surface of the Peltiers we put indium foil for enhanced thermal connection. In the next step we glued the thermistors in the holes of the copper plate with Torr Seal. Due to the small wire size of the thermistors we ripped several of the thermistor wires in the next steps. Hence, we decided to do a rather unconventional solution: We soldered a 1 mm thick Kapton insulated wire on the Thermistor wire and then we put Torr Seal both over the thermistor and over the soldering connection, as can be seen in Fig. 7.2(b). This step should prevent any mechanical stress on the thermistors. Care was taken not to include any virtual leaks in the Torr Seal part and to electrically insulate the wires from the copper surface.

We then assembled the copper box. The next problem occurred when we wanted to lift the empty copper box in the chamber. The extrusions on the heat sink and the bottom plate of the copper plate were not deep enough to ensure that the Peltier elements were at the right spot and the box was not wobbling. As a solution to this problem we waterjetted a form which fits in between the vacuum chamber and the copper box and ensures that the copper box is in the right place. This tool was placed on both sides of the chamber and can be seen in Fig. 7.3(a).

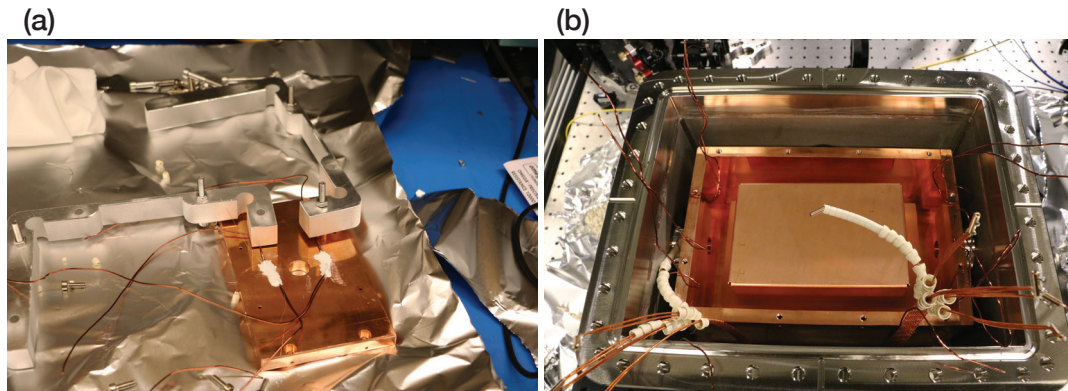


Fig. 7.3 (a) Picture of the mounting form to correctly place the copper box. On the heatsink one can see the Peltier elements. (b) The copper box is in the cavity. Also the inner heat shield is in place.

Following this process, we mounted the Zerodur spacer on top of Viton pads in the copper box. Also we put the inner heat shield into the copper box. The mounted inner shield can be seen in Fig. 7.3(b). Afterwards we closed the copper box with a the lid and connected the thermistors with the Kapton insulated wires. In the next step we connected the 5-way-cross to the ion pump, with the angle valve and then with the vacuum chamber. It is important to proceed in this order because the silver screws of the angle valve can otherwise not be accessed. In the next step we attached the viewports onto the vacuum chamber and then we tightened all CF-40 flanges with 18 Nm torque. We then connected the turbo pump with a bellows to the angle valve. An overview of the vacuum chamber with everything but the vacuum housing lid connected can be seen in Fig. 7.4.

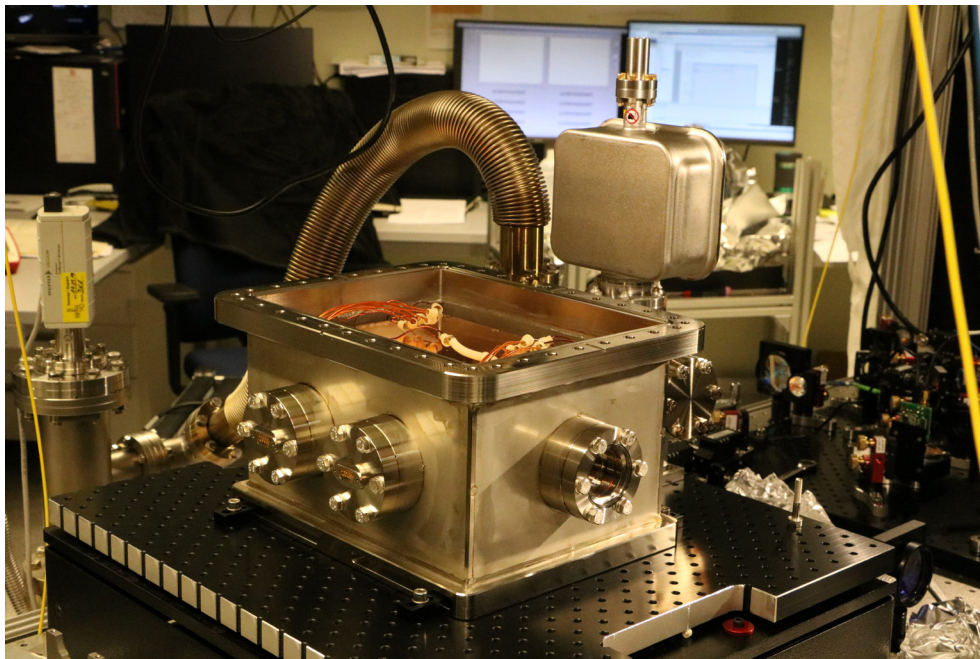


Fig. 7.4 On the picture one can see the vacuum housing in the front and the ion pump and the angle valve in the back.

Since we wanted to do a first bakeout of the vacuum housing before putting the optical resonator in, we closed the chamber with the lid. We applied a torque of 23 Nm to the M8 screws used here. We started the turbo pump and within the first 24 hours we reached a pressure of $7 \cdot 10^{-7}$ mbar. We then decided to bake the vacuum chamber. The maximum baking temperature was limited to 80°C due to the Peltier elements, whose maximum storage temperature is 80°C . Furthermore, one must be careful when heating the vibration isolation platform, since springs on the inside of the platform can be deformed. We vacuum baked the cavity with the vibration isolation platform underneath the cavity.

Baking for four days reduced the pressure on the pressure gauge attached to the turbo pump to $2 \cdot 10^{-7}$ mbar. We then turned off the turbo pump, flushed the cavity with argon, detached the turbo pump and moved the cavity from our small optical table to the laser optical table. There we opened the lid of the vacuum housing, the copper box and removed the lid of the upper heatshield to put in the cavity. The mounting position of the optical resonator on the Zerodur spacer with Viton pads is symmetric and can be seen in Fig. 7.5(a). A good overview of the position of the optical resonator within the vacuum housing and a close up on the rectangular copper gasket of the vacuum housing lid can be seen in Fig. 7.5(b).

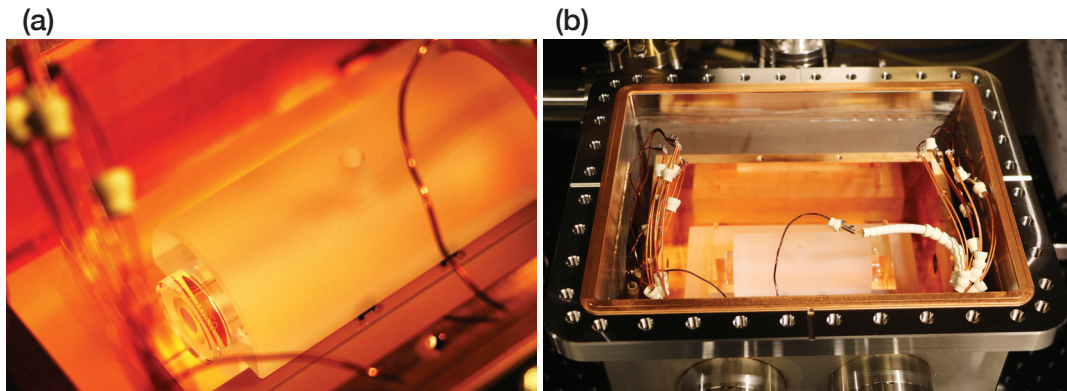


Fig. 7.5 (a) Picture of the optical resonator mounted with Viton pads on the Zerodur spacer. (b) The position of the optical resonator within the housing can be seen very well on this picture. The custom copper gasket (already used from the bakeout) can also be seen.

After putting the optical resonator in the cavity we put all heat shields back into their positions and closed the lid again. We then connected back the turbo pump and started pumping again. After a night of pumping, we started the ion pump at a pressure of 10^{-6} mbar and after three days of pumping we reached a pressure of $7 \cdot 10^{-7}$ mbar. We then valved off the turbo pump and disconnected it. After two more weeks of baking we reached a pressure of $6 \cdot 10^{-8}$ mbar. The pressure is still falling (very slowly). However, we could do a low temperature bakeout at 40-50°C for some weeks. Unfortunately this bakeout did not fit into the time schedule of my master's thesis and therefore we decided to do first measurements without a bakeout. A bakeout would give a better pressure but for this we would need to remove all optics on the cavity breadboard.

During the bakeout of the cavity we were already able to characterize the temperature characteristics of our system.

7.4 Analysis of the Temperature Properties of the Steel Chamber Cavity

In our vacuum system our copper box cools via a conductive process (connection via the Peltier elements) but also via a radiative process to the vacuum chamber and the inner heat shield. However, the two processes scale differently with temperature. The conductive cooling process is directly proportional to temperature changes while the radiative cooling process scales with T^4 . Hence, it is useful to approximate the radiative process with a linear process to obtain an overall linear behavior of the heating process [55]. With this approximation, the radiative heating process described in Sec. 6.2.2 can be expressed as

$$P_{\text{rad}} = \alpha_{\text{rad}} A (T_2 - T_1), \quad (7.1)$$

where α_{rad} is the characteristic radiative coupling of two objects and A is the area of the object emitting heat. Combining the two heat transfer processes, we obtain [55]

$$mc \frac{dT_2}{dt} = -\alpha_{\text{tot}} A (T_2 - T_1), \quad (7.2)$$

where α_{tot} describes the total coupling of our system. This equation holds if the heat conduction in a system dominates the heat convection, which is a valid assumption for our system since we can assign a single temperature to the copper box due to the good thermal conductivity of copper [55]. The solution of the differential equation in Eqn. (7.2) is an exponential decay. It is commonly called Newton's law of cooling and is given by

$$T_2(t) = T_1 + (T_1 - T_2)e^{-t/\tau}. \quad (7.3)$$

The time constant τ gives an estimate for how much our system is decoupled from the environment. We now want to understand which time constant our system has.

Our system consists of three different parts that can be seen in Fig. 7.6.

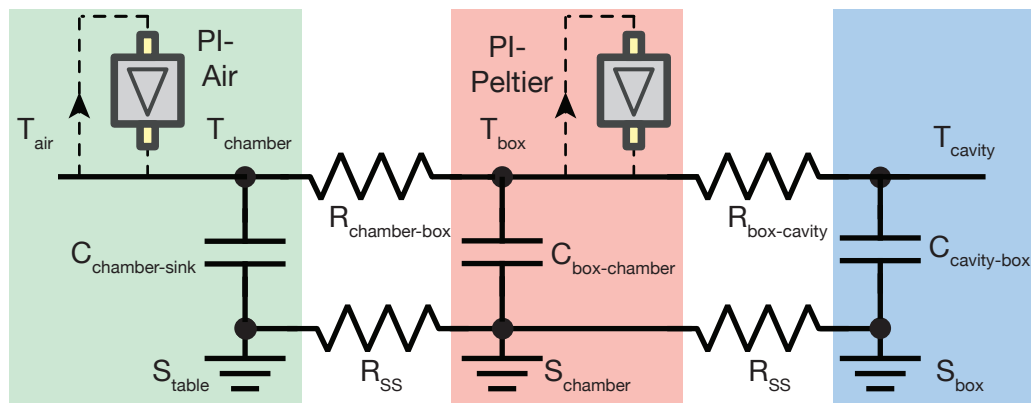


Fig. 7.6 The temperature control system consists of three different parts. The green shaded part of the system shows the actively temperature controlled components of the wood box and of the vacuum chamber. The red shaded part of the system shows the actively temperature controlled components of the vacuum chamber. The blue shaded part of the system represents the Zerodur holder, the inner heat shield and the optical resonator.

We start from the inside of the cavity to understand its setup. The optical resonator, the inner shield and the Zerodur holder (in this figure these elements are abbreviated as “the cavity”) are standing on Viton Pads, which are placed on the baseplate of the copper box. Heat between these two components can be transferred to the copper box with resistance $R_{\text{box-cavity}}$ radiatively or conductively via the Viton pads. Since the thermal conductivity of Viton is relatively small and the copper boxes are polished to get a small emissivity, the capacity $C_{\text{cavity-box}}$ is small. The cavity is heat sunk to the copper box. A PI loop actively stabilizes the temperature of the copper box. Hence, the temperature T_{box} is stable. The

copper box is heat sunk to the chamber and exchanges heat mostly via conduction to the vacuum chamber with thermal resistance $R_{\text{chamber-box}}$. Since the thermal contact resistance to the steel chamber is decreased by using indium foil the contact resistance from the copper box to the steel chamber is kept as low as possible to obtain a high thermal capacity $C_{\text{box-chamber}}$ and therefore good low pass filter characteristics. Finally, the steel vacuum chamber mounted on the vibration isolation platform is heat-sunk to the optical table. Additionally, we plan to build another wooden box around the cavity to decrease the air temperature fluctuations in the box (see Sec. 6.3).

A first characterization of the vacuum housing of the steel cavity was done by measuring the time constant of the temperature stabilization of the copper box. We heated up the copper box with Peltier elements to 40°C while the steel chamber was not pumped on (pressure of $\approx 10^{-4}$ mbar in the chamber) and let the system equilibrate for some time. We then turned off the heaters and the copper box cooled down exponentially. The temperature was measured with the thermistors glued to the copper box. We repeated the same heating process when the cavity was evacuated to a pressure of 2×10^{-7} mbar. The cooling process under the better vacuum conditions is denoted as August in Fig. 7.7, while the cooling process under the worse vacuum condition is denoted as September.

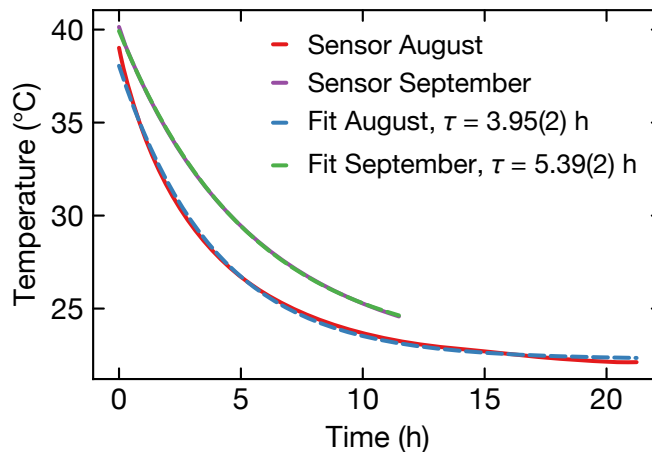


Fig. 7.7 The plot shows the exponential decrease of the temperature at the Left Bottom (LB) sensor after turning off the Peltier heaters for two time intervals in August and September. The copper box was stabilized with the Peltier heaters to around 40°C in both cases. The red trace (with the blue fit) was taken in August at a very high pressure in the chamber. The purple trace (with the green fit) was taken in September at a pressure of 2×10^{-7} mbar in the chamber.

The characteristic time constants of the exponential temperature decrease are $\tau_{\text{aug}} = 3.95(2)$ h and $\tau_{\text{sep}} = 5.39(2)$ h respectively. The error on the fit was obtained by calcu-

lating the total error $e_{\text{tot}} = \sqrt{e_{\text{fit}}^2 + e_{\text{therm}}^2}$ of the fit for the three different thermistors and of the thermistor values. The conduction properties of the copper box to the vacuum chamber were the same since the copper box was not moved in position. Contrary, we put the optical resonator into the copper box and therefore increased the weight of the copper box which increases the conductive link in between the copper box and the steel chamber. Hence, we attribute the longer time constant of the copper box under higher vacuum to the absence of air molecules that can transfer heat from the copper box to the steel chamber. However, the time constant of the vacuum chamber is long enough to suppress fast changes of the environment. The time constant is not long enough to suppress daily fluctuations. Therefore we need an additional heat shield that surrounds the vacuum housing as described in Sec. 6.3 to minimize periodic temperature changes. However, Stephan measured a characteristic time constant $\tau = 20.6(7)$ h for the first-generation cavity [43]. The difference in the time constant of almost factor 4 between the two cavities can be attributed to the higher conductive link of the steel cavity via the Peltier elements. In the first-generation cavity, four Viton pads with a total area of 400 mm^2 act as a conductive link between the copper box and the aluminum. For our steel chamber the area of the conductive link is $2 \times 1600 \text{ mm}^2$. Hence the Peltier elements have an eight times increased conductive link (see Eqn.(6.22) for the definition of the conductive resistance). The height of the Peltier elements is 8 mm and the height of the Viton pads in the aluminum cavity is 10 mm. Hence the thickness factor in the conductive link is comparable. However, the thermal conductivity coefficient of Viton ($\lambda_{\text{Viton}} = 0.2 - 1.3 \text{ W}/(\text{m} \cdot \text{K})$) [56]) is higher than the thermal conductivity of the Peltier element. From the measurement we assume the thermal conductivity of the Peltier elements to be four times smaller than the thermal conductivity of the Viton pads.

Looking at Fig. 7.6 another characteristic time constant is the speed with which heat is transferred from the outside of the steel box to the inside of the steel box. We measured this time constant during the bakeout of the steel chamber. Here, we wrapped the vacuum chamber of the cavity with one layer of aluminum foil, then we mounted heating tapes homogeneously around the vacuum chamber, put a layer of fiber glass and more aluminum around the chamber. The temperature was measured with K-type thermocouples attached to the the outside of the steel chamber. To start the bakeout procedure we ramped up the temperature of the vacuum chamber with a ramp speed of 0.5°C . This ramp speed value was chosen to not destroy viewports during baking. A graph of the temperature curves of the inside of the cavity and the outside of the steel chamber is shown in Fig. 7.8.

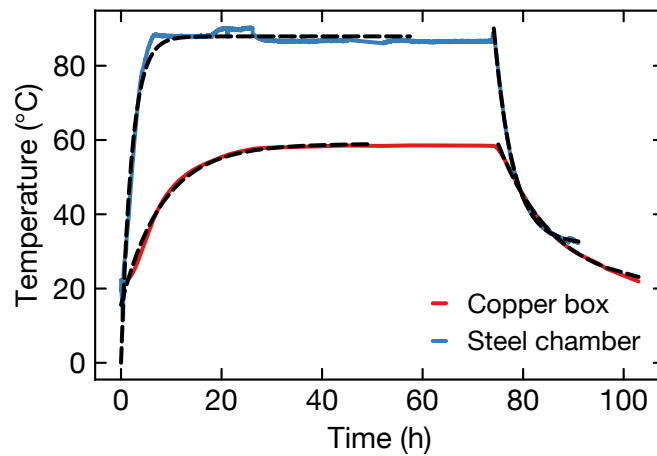


Fig. 7.8 Measurement of the heating and cooling time constants of the bakeout. The blue trace is the temperature measured over time with a thermocouple on the outside of the vacuum chamber. The red curve shows the temperature of one of the thermistors glued to the copper box. The black dashed lines show the fits to the temperature curves.

The decreased end temperature of the copper box in comparison with the vacuum chamber can be explained by the fact that the PI loop keeping the temperature at 85°C is servoing a thermocouple attached to the vacuum chamber. However, when reaching a steady state of the heating process, a lot of the heat will be flowing to the optical table via the vibration isolation platform which decreases the end temperature on the inside of the chamber. Even though Newton's law for cooling processes was defined for cooling processes only, we want to fit heating processes with an exponential decay ansatz as well [57], to get an estimate for the decoupling of the vacuum chamber and the copper box. The obtained exponential fits for the time constants of the heating and cooling process are given in Tab. 7.1.

$\tau_{\text{steel,heat}}$	$\tau_{\text{steel,cool}}$	$\tau_{\text{copper,heat}}$	$\tau_{\text{copper,cool}}$
2.1 h	3.8 h	8.25 h	11.3 h

Tab. 7.1 Fitted time constants of the bakeout process

The temperature of the outside of the steel chamber rises quickly with a time constant of $\tau_{\text{steel,heat}} = 2.1$ h. One can see that the thermistor on the copper box sees the temperature change almost instantly. However, the heating process on the inside is (with a time constant of $\tau_{\text{copper,heat}} = 8.25$ h) much slower than the heating process on the air side. Hence, the heating constant of the copper box on the inside is slower by almost a factor of 4. We can also fit an exponential decay to the cooling process of the steel chamber

after the baking process over approximately 70 h. It has a characteristic time constant of 3.8 h. The time constant of a cooling process compared to a heating process differs by a factor 2. This can be attributed to the additional thermal insulation of the fiber glass and aluminum foil. A longer cooling constant is even more prominent on the cooling time of the copper box. The characteristic cooling time is double the time as for the non insulated case. For this comparison another factor comes into play: When only heating the copper box, the radiative link (scaling as T^4) between the copper box and the vacuum chamber was larger than in the vacuum bakeout procedure, where the vacuum housing was also heated.

The low thermal link of the vacuum chamber to the copper box in combination with a good temperature control is able to achieve sub-mK temperature stability.

Chapter 8

Testing the Second-generation Cavity

After finishing the construction of the second-generation cavity we were able to frequency stabilize a laser to the cavity using the Pound-Drever-Hall (PDH) frequency stabilization scheme. The frequency stabilized laser is chosen to have a frequency close to the 1S_0 - 3P_1 -transition frequency, such that we can perform an optical heterodyne mixing of the laser stabilized to the second-generation cavity with the red MOT cooling laser stabilized to the first-generation cavity.

In this Chapter we discuss important characteristics of the Pound-Drever-Hall frequency-stabilization setup that determine the achievable frequency stability of a laser. Residual amplitude modulation on the EOM-crystal shifts the PDH-scheme error signal. Further, we measure the finesse of the optical resonator. With the locked laser in operation we compare a laser stabilized to the the second-generation cavity to a laser stabilized to the first-generation cavity. From this comparison we can determine an upper bound on the frequency instability of the two lasers stabilized to the first and second-generation cavity, respectively. Additionally we measure the zero-crossing temperature of the second-generation optical resonator.

8.1 Pound-Drever-Hall Frequency Stabilization

To understand how an amplitude modulation of the error signal of the Pound-Drever-Hall technique can come about, we first need to understand the principle of the Pound-Drever-Hall frequency-stabilization of a laser. Figure 8.1 gives an overview over the components of the PDH frequency-stabilization technique.

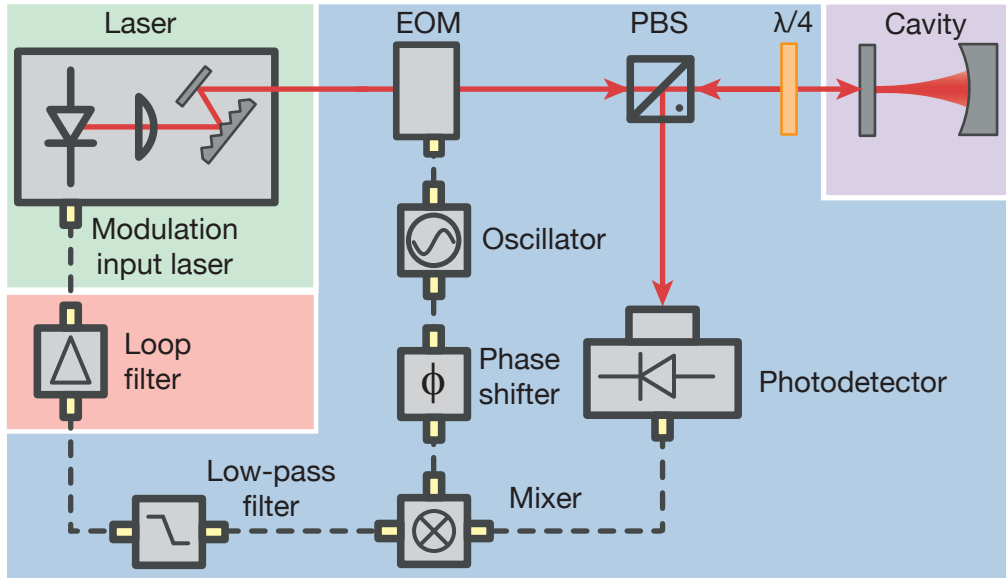


Fig. 8.1 Schematic of the Pound-Drever-Hall frequency stabilization setup. The laser to be locked is shaded in green. The light from the laser is phase modulated and then coupled into an optical resonator (purple). If not on resonance the light reflected from the cavity is converted to an electric signal in the photodetector. Then a phase detector detects the error signal for the frequency deviation. The blue shaded region acts as a phase detector. The obtained error signal is then fed to the loop filter (shaded red) and from there to the current modulation port of the laser.

The laser sends out light with frequency ω and an electric field which we can describe as $E_{\text{inc}} = E_0 e^{i\omega t}$. In an electro-optic-modulator (EOM) light is phase modulated with modulation frequency Ω . The resulting electric field is given by

$$E_{\text{EOM}}(\omega) = E_0 [J_0(\beta) e^{i\omega t} + J_1(\beta) e^{i(\omega+\Omega)t} - J_1(\beta) e^{i(\omega-\Omega)t}], \quad (8.1)$$

where the terms oscillating with $\omega \pm \Omega$ are called sidebands and where $J_i(\beta)$ are Bessel functions. Phase modulation processes are described in Sec. 2.2. The light is then transmitted through a polarizing beam splitter and coupled into the cavity. As described in Sec. 6.1, the cavity will only transmit light if the laser is on resonance with the cavity resonance. The cavity will therefore have the transfer function

$$F_{\text{cavity}}(\omega) = \frac{E_{\text{ref}}}{E_{\text{inc}}} = \frac{r(\exp(i\frac{\omega}{\omega_{\text{FSR}}}) - 1)}{1 - r^2 \exp(i\frac{\omega}{\omega_{\text{FSR}}})}, \quad (8.2)$$

for light that is reflected from the cavity. The free spectral range ω_{FSR} describes the angular frequency corresponding to the distance between two modes in the cavity. After passing the $\lambda/4$ plate twice the light reflected from the cavity is reflected from the PBS and focused onto a photodetector. The photodetector measures the intensity of the light

which is proportional to the square of the electric field. The AC-coupled signal produced by the photodetector can be expressed as [58]

$$\begin{aligned} P_{\text{PD}}(\omega) &= [E_{\text{EOM}} F_{\text{cavity}}(\omega)]^2 \\ &= J_0(\beta) J_1(\beta) \{ \text{Re} [F(\omega) F^*(\omega + \Omega) - F^*(\omega) F(\omega - \Omega)] \cos(\Omega t) \\ &\quad + \text{Im} [F(\omega) F^*(\omega + \Omega) - F^*(\omega) F(\omega - \Omega)] \sin(\Omega t) + 2\Omega \text{ terms} \}, \end{aligned} \quad (8.3)$$

where $F^*(\omega)$ is the complex conjugate of $F(\omega)$. The photodetector signal is AC-coupled, hence DC-terms vanish. The terms oscillating with frequency Ω correspond to the sidebands from the phase modulation. Higher order oscillations are low-pass filtered in the PDH frequency stabilization scheme.

If the modulation frequency Ω is sufficiently fast ($\Omega \gg \omega_{\text{cavity}}$ where ω_{cavity} is the linewidth of the cavity; (here $F = 270000$, $\omega_{\text{cavity}} \approx 2\pi \times 5 \text{ kHz}$) the phase modulated sidebands on the light are totally reflected and the photodetector signal can be demodulated with the modulation frequency Ω . Low-pass filtering this signal to remove the terms oscillating with frequency 2Ω gives the error signal [58]

$$\epsilon_{\text{PDH}} = -2J_0(\beta) J_1(\beta) \text{Im} [F(\omega) F^*(\omega + \Omega) + F^*(\omega) F(\omega - \Omega)]. \quad (8.4)$$

Close to the resonance of the cavity the error signal has a linear dependence on the frequency. The error signal vanishes if the laser is on resonance with the cavity's resonance. An illustration of this error signal can be found in Ref. [43]. Analogous to the phase locked loop example from Cha. 3 this error signal can be fed into a loop filter which then modulates the laser to frequency stabilize the laser to the cavity resonance.

8.2 Residual Amplitude Modulation (RAM)

In the PDH frequency-stabilization scheme we use phase modulators to modulate sidebands on the light. An electro-optic phase modulator consists of a crystal where a modulated electric field E_z is applied along the z -axis. Most of the times the crystal is a lithium niobate crystal with birefringent properties, i.e. the crystal axes have different refractive indices. We can apply an electric field on this crystal in z -direction to change the refractive index of the material. The refractive index of LiNbO_3 -crystals in z -direction can be described by [59]

$$\Delta n_z(t) = -\frac{1}{2} n_z^3 r_{zz} E_z(t), \quad (8.5)$$

where n_z is the refractive index for light polarized on the z -axis and r_{zz} is the electro optic coefficient, describing the coupling of the electric field to the change of the refractive index. Light which passes through the crystal sees a periodically modulated refractive index in z -direction. Hence, the propagation speed of the light through the crystal changes periodically and the phase of the light after the crystal is also modulated.

A real electro-optic modulator does not modulate the phase of the light perfectly. There are two main causes for an additional amplitude modulation of the electric field. First, multiple reflections on the surfaces of the EOM crystal generate etaloning effects inside the EOM. Hence the reflected electric field interferes and creates a standing wave which as a result modulates the amplitude [60]. The second main reason for amplitude modulation in the EOM is caused by a mismatch of the polarization plane of the EOM and the linearly polarized light field. If the polarization of the input beam is not aligned onto the electrically modulated axis of the EOM, the different components experience different phase shifts due to natural birefringence properties of the EOM crystal [61]. The further light is misaligned from the z-axis, the more it also sees a phase shift of the x- and y-axis of the EOM. The natural birefringence of the x- and y-axis is temperature dependent. Hence, an off-axis polarization of the EOM causes a temperature dependence of the phase shift of the light in x- and y-direction. This phase shift is converted to an amplitude modulation when passing a polarizing beam splitter as e.g. in the PDH-setup (see Fig. 8.1).

In the following we want to express the birefringence properties of light which passes the EOM, which is modulated with modulation frequency ω , and is focused on a photodiode. The current of the photodiode in the PDH-setup (see Fig. 8.1) has components of residual amplitude modulation. They can be modeled as [59, 61]

$$I(\Omega, t) = -E_0 \sin(2\beta) \sin(2\gamma) \sin(\Omega t) \sin[\Delta\phi(t) + \Delta\phi_{\text{comp}}(t)], \quad (8.6)$$

where $\sin(2\beta) \sin(2\gamma)$ are polarization alignment factors, $\Delta\phi$ is the phase shift due to the temperature dependence of the birefringence of the EOM crystal and $\Delta\phi_{\text{comp}}$ is an actively controlled phase shift compensating for the birefringence of the EOM. The natural birefringence properties of the EOM crystal can be compensated by changing the temperature of the EOM crystal and changing the offset DC-electric field [62] on the modulation voltage. Note that for a fully compensated phase shift, $I(\Omega)$ vanishes.

In the PDH-setup described in Sec. 8.1 the current from residual amplitude modulation will add onto the current from the PDH error signal in Eqn. (8.3). Both summands oscillate at frequency Ω . Hence, after demodulating the voltage from the photodetector and low pass filtering it, the error signal of the Pound-Drever-Hall locking technique contains a time varying offset from zero proportional to

$$\epsilon_{\text{RAM}} = -E_0 \sin(2\beta) \sin(2\gamma) \sin[\Delta\phi(t) + \Delta\phi_{\text{comp}}(t)], \quad (8.7)$$

determined by the natural birefringence properties. This offset shifts the zero crossing of the error signal. The PI-controller controls the laser's frequency such that the error signal is zero. Hence, an offset fluctuation of the error signal will lead to frequency fluctuations. The characteristic timescale of the offset fluctuations is the timescale of the temperature fluctuations changing the birefringence of the EOM crystal. To obtain a non-drifting frequency-stabilization, we hence need to control the RAM signal.

The residual amplitude modulation of the light field after passing the EOM and after being reflected is equal in magnitude since off resonant reflection from the optical resonator changes the electric field value by the factor -1 (see Eqn. (8.2)).

The authors of Ref. [61] suggest an active residual amplitude cancellation scheme. They were able to measure the residual amplitude modulation on their EOM crystal and actively cancel the effect of RAM by changing the temperature and an additional offset voltage to the modulation signal of their EOM.

Similarly, we want to check whether we can detect residual amplitude modulation. We measured the effect of temperature drifts on the residual amplitude modulation of an EOM crystal to estimate how much the error signal offset of the Pound-Drever-Hall scheme changes over time. We changed the temperature of the EOM casing periodically and measured the residual amplitude modulation signal proportional to the current from Eqn. (8.6).

For our Pound-Drever-Hall setup we compared the residual amplitude properties of two different kinds of EOMs: a bulk EOM with a crystal from Casix and an LC circuit resonant at 20.41 MHz and a fiber EOM model PM705 (Jenoptik). The test setup for the RAM measurement of the fiber EOM and the bulk EOM look differently and are shown in Fig. 8.2.

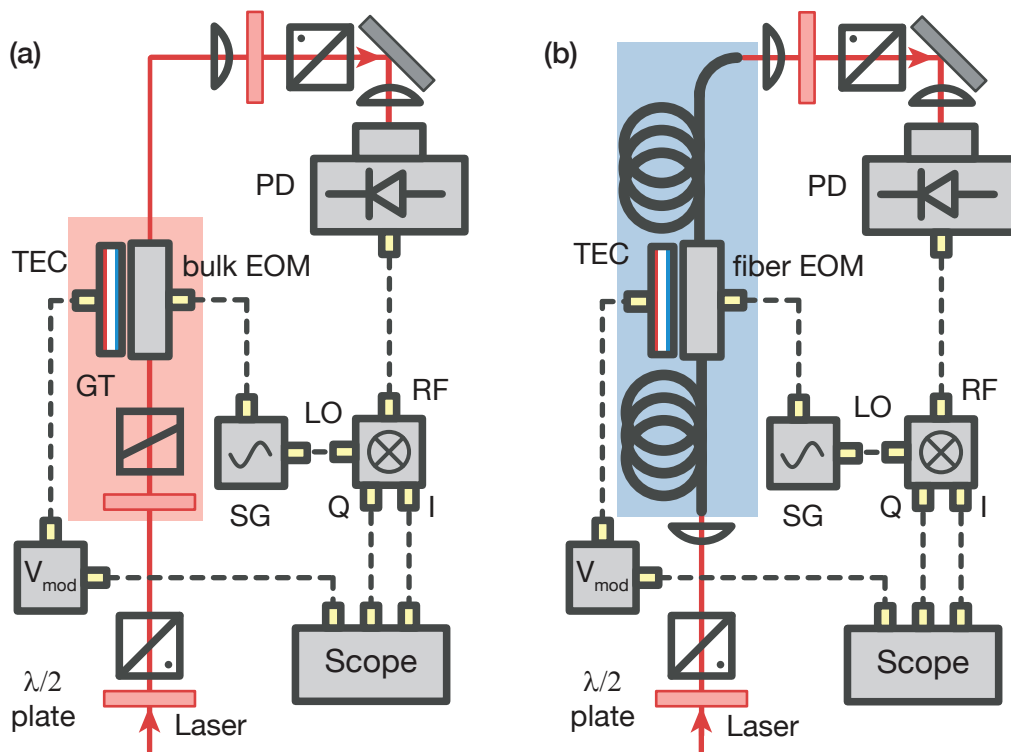


Fig. 8.2 Test setup for the detection of residual amplitude modulation caused by phase modulation in an EOM. (a) Test setup for the measurement of RAM caused by a bulk EOM. Light is polarization cleaned with a $\lambda/2$ -plate, a PBS and a Glan-Taylor polarizer (GT) and then guided onto the EOM. The casing of the EOM is temperature modulated with a Peltier element (TEC). After the EOM the phase fluctuations of the electric field are converted to amplitude fluctuations by a $\lambda/2$ -plate followed by a polarizing beam splitter (PBS). The light is focused on a fast photodetector. The photodetector signal is demodulated with an I-Q demodulator and then monitored on a oscilloscope. (b) Test setup for the measurement of RAM caused by a fiber EOM. Differences between the bulk EOM setup and the fiber EOM setup are shaded red and blue. Light from the laser is coupled into the fiber EOM, the out coupled light is polarization cleaned in the PBS. The detection method is the same as in the bulk EOM setup.

For a bulk EOM we need a polarizer in front of the EOM to align the electric field incident on the EOM to the polarization axis of the EOM. We tested the bulk EOM with the setup shown in Fig. 8.2(a).

The EOM crystal's temperature was periodically modulated on a time interval of 20 s. The RAM-current signal from Eqn. (8.6) was demodulated with the modulation frequency of the EOM on an I-Q demodulator. An I-Q demodulator allows to measure both the in-phase and the quadrature part of the demodulated RAM-signal which is in particular useful for determining changes of the amplitude of the RAM-signal. The demodulated signal from a double balanced mixer is a DC complex electric field. Using the phasor

picture (see Cha. 2), the DC-electric field has both a real and an imaginary part. With the oscilloscope we can only measure the real part of the electric field. If we by accident choose the phase delay of the coax-cable in an unfortunate way, a signal demodulated with a double balanced mixer might not contain any real part of the electric field. The I-Q demodulator measures both the demodulated RAM signal and the 90° phased shifted demodulated RAM signal. By simultaneously measuring the I and the Q port we can obtain the full RAM-signal. The magnitude of the RAM-signal, defined as $M = \sqrt{Q^2 + I^2}$, is compared to the temperature modulation on plot of the overlapping Allan deviation of the magnitude of the RAM-signal for different angles of the Glan-Taylor polarizator in Fig. 8.3.

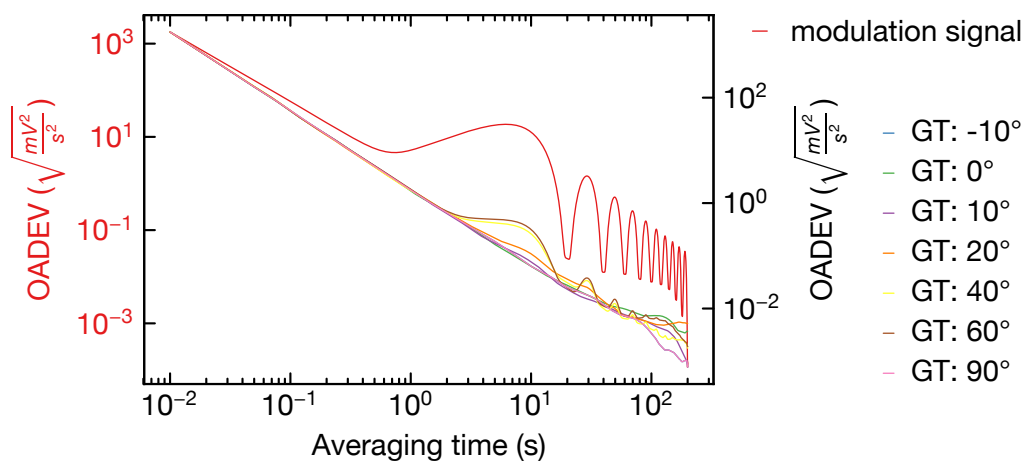


Fig. 8.3 The overlapping Allan deviation of the magnitude of the residual amplitude modulation on a bulk EOM. The overlapping Allan Deviation of the magnitude of the RAM signal is plotted against the averaging time. Shown on the left y-axis is the scaling of the temperature modulation signal (axis and trace in red). The right y-axis gives the scaling of the RAM-signals for different Glan-Taylor polarizator (GT) angles (black y-axis). The temperature was modulated with a period of 20 s. The magnitude of the dips of the Allan variance is dependent on the angle of the Glan-Taylor polarizator, indicating the EOM polarization axis. The z -axis of the EOM is approximately aligned with a Glan-Taylor polarization angle of 0° .

The RAM signal depends on the misalignment of the laser with respect to the polarization axis of the EOM crystal. We measured the temperature dependence of the RAM signal for different polarization mismatches between the light and the crystal modulation axis. The misalignment is given as the angle of the Glan-Taylor polarizator. Hence we expect the temperature of the EOM to change periodically over time when we periodically drive the temperature of the EOM with a TEC. This behavior can be well understood by looking at the overlapping Allan deviation of the RAM oscillations. A periodic signal will aver-

age over its oscillation period. Hence, the temperature modulation trace in Fig. 8.3 has periodic dips over multiples of its oscillation period. The RAM-signal shows similar dips at the oscillation period of the temperature driving. Therefore, we can infer a correlation between the temperature driving of the EOM and the RAM signal. The temperature dependence of the RAM signal is maximal for a misalignment of the polarization of the light between 40° and 60° and almost fully vanishes for light polarizations matching the polarization of the EOM crystal.

With a fiber EOM one can circumvent a misalignment of the polarization of the light with the crystal modulation axis. The light is coupled into a polarization maintaining fiber (PM-fiber), which is glued onto the the EOM-case aligned to the EOM polarization axis. The EOM PM705 has polarizing characteristics, hence the polarization of the light incident on the EOM is not dependent on the input polarization. We tested the temperature dependence of the RAM-signal of the fiber EOM with a similar test setup as for the bulk EOM. The test setup is shown in Fig. 8.2(b). The light from the laser is polarization cleaned, coupled into the fiber EOM, phase modulated and then coupled out of the fiber. The rest of the setup is analogous to the bulk EOM test setup.

The overlapping Allan deviation of the RAM signal of the fiber EOM when temperature modulating the EOM crystal is shown in Fig. 8.4.

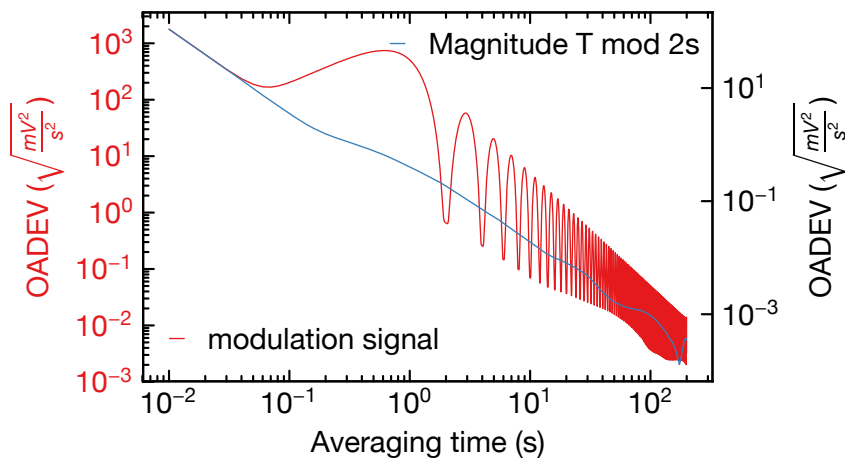


Fig. 8.4 The overlapping Allan deviation of the magnitude of the residual amplitude modulation on a fiber EOM. The overlapping Allan Deviation OADEV of the magnitude of the RAM signal is plotted against the averaging time. The left y-axis gives a the scaling of the temperature modulation signal (axis and trace in red). The right y-axis gives the scaling of the RAM-signal (black axis). The temperature was modulated with a period of 2s. We can not see a clear dip on the RAM signal which can be correlated to the modulation signal.

As can be seen in Fig. 8.2 the RAM signal of the fiber EOM when temperature modulating the TEC-element does not show a significant temperature dependence similarly to the bulk EOM measurement for Glan-Taylor angles close to 0° .

We were not able to see a change of the demodulated signal of the electric field on the oscilloscope by manually changing the temperature of the fiber EOM. We conclude that an active control of the temperature of the fiber EOM does not make sense when using our detection method. Hence, the best way to suppress residual amplitude modulation is a stabilization of the temperature of the fiber EOM with a temperature controller.

8.3 Finesse Measurement of the Cavity

To measure the finesse of the cavity we set up the optics for a Pound-Drever-Hall frequency stabilization to the second-generation cavity. The schematic of the optics setup was built similarly to the setup of the first-generation cavity [43]. We locked a home-built external cavity diode laser at a wavelength of 689.4 nm to the cavity. The laser was built by a previous bachelor student and is denoted as “homebuilt linear laser” in the following. The setup and the characterization of the laser are described in Ref. [63, 64]. The coating of the optical resonator was chosen to have a finesse of approximately $F = 280000$ for both the clock transition of strontium and the red MOT transition at a wavelength of 698 nm and 689 nm, respectively.

After having locked the laser to the cavity we were able to measure the finesse of the cavity. To do so, we shuttered off the light going to the cavity setup with a double-pass AOM. Then we measured the exponential decay of the light intensity stored in the cavity as described in Sec. 6.1. We made sure that the fall-time of the AOM (Gooch & Housego 3350-199 with a specified fall-time of 9 ns at a beam diameter of 50 μm) is much shorter than the expected ringdown time constant of the optical resonator (approximately 30 μs). We measured the decaying transmission light intensity of the optical resonator and fitted the solution of the differential equation (given in Eqn. (6.8)) to the measured voltage from the photodetector. We then extracted the ringdown time from the fit. Averaging over 20 datasets we obtain a time constant of $\tau = 29.03(3) \mu\text{s}$. A fit of the ringdown data is shown in Fig. 8.5.

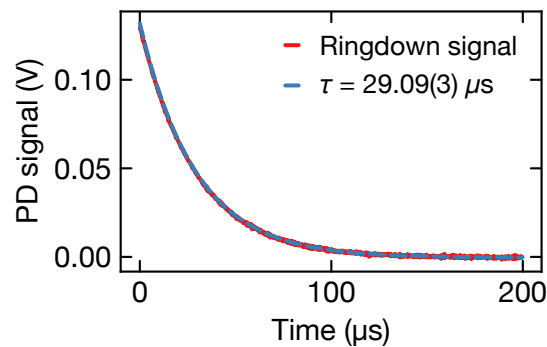


Fig. 8.5 Measurement of the characteristic time constant of the ringdown of the cavity. The red trace shows the transmitted light intensity through the cavity on a photodetector. The blue trace is a fit to the exponential decay of the light intensity and gives us a characteristic ring-down time constant of $\tau = 29.03(3) \mu\text{s}$.

The time constant τ can be converted to the finesse of the optical resonator using Eqn. (6.9). Hence we could determine the finesse of the optical resonator for light at a wavelength of 689.4 nm to be $F = 2.742(2) \times 10^5$. This value for the finesse roughly matches with the finesse $F = 281000$ measured for the first-generation cavity [43]. In future, the the finesse of the optical resonator at the clock laser wavelength of 698 nm should also be tested since the cavity will eventually be used to frequency-stabilize the clock laser.

8.4 Optical Heterodyne Mixing of Two Narrow Lasers

With the first-generation and the second-generation cavities in our lab we are now able to compare the line shapes of two different lasers frequency stabilized to their respective high finesse cavities. This measurement gives us an upper limit on the frequency uncertainty of both lasers as explained in Sec. 5.1.

For our measurement we beat two lasers with a wavelength of approximately 689.4 nm. The first laser is a Toptica DL pro laser in a Littrow configuration typically used for cooling on the red MOT transition. The second laser is the homebuilt linear laser. The red MOT laser is frequency stabilized to the first-generation cavity and the homebuilt linear laser is frequency stabilized to the second-generation cavity. Both lasers are set up with the same laser driving electronics set Toptica SYS DC 110 and the PI-controller Toptica FALC 110. We did an optical heterodyne beat measurement of the two stabilized lasers. A schematic of the heterodyne mixing setup can be found in Fig. 8.6.

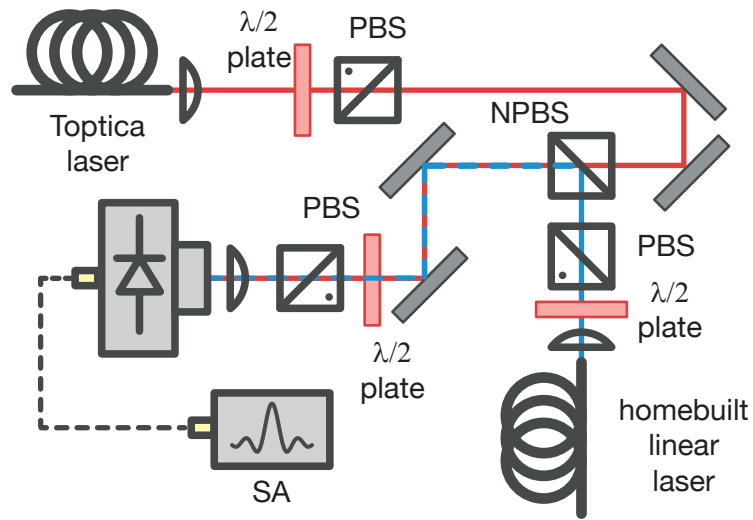


Fig. 8.6 Heterodyne mixing setup to compare the line shape of two lasers. Light from two lasers is outcoupled. Both beams are polarization cleaned with a $\lambda/2$ -plate and a polarizing beam splitter (PBS). Then they are overlapped on a non-polarizing beam splitter (NPBS) and aligned onto a high bandwidth photodetector. A spectrum analyzer is connected to the photodetector to monitor the heterodyne mixing power spectral density.

We couple light from the two lasers into a fiber. We then outcouple light from the two fibers on the heterodyne mixing setup. Here we polarization clean both beams with a $\lambda/2$ -plate and a polarizing beam splitter. We then combine the two beams on a non-polarizing beam splitter and focus both beams onto a high bandwidth photodetector (Newport 818-BB-45). After aligning the combined beam on the photodetector we can see a heterodyne beat signal of the two beams, which is shown in Fig. 8.7.

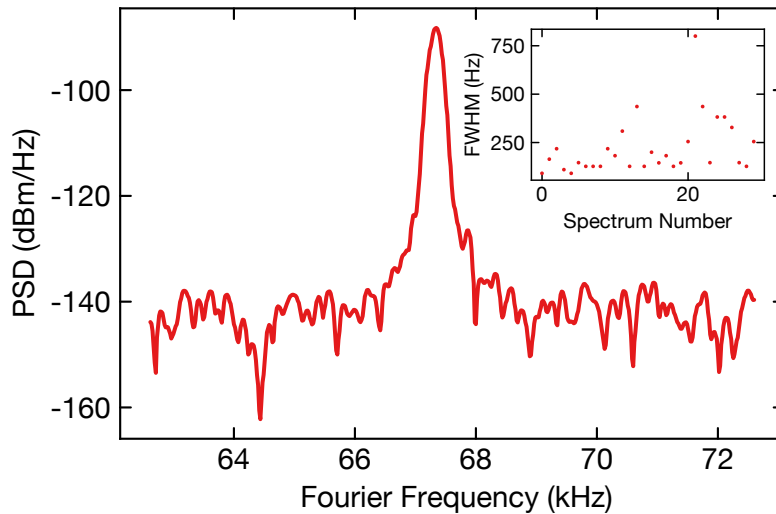


Fig. 8.7 Heterodyne mixing signal of the Toptica laser and the homebuilt linear laser. The power spectral density of the heterodyne mixing spectrum is plotted against the Fourier frequency with a frequency offset of 2296.5 MHz. By averaging over 20 power spectral densities of the beat signal we obtain a full width half maximum $\text{FWHM} = 1.7(8) \times 10^2 \text{ Hz}$ of the laser. The inset shows the FWHM for each measured power spectral density. The resolution bandwidth of the spectrum analyzer $\text{RBW} = 30 \text{ Hz}$ limits the resolution of this plot.

The beat signal of the two lasers has a full width half maximum of $\text{FWHM} = 1.7(8) \times 10^2 \text{ Hz}$. However, the measured FWHM of the two lasers has a high standard deviation. The sweep of the spectrum analyzer can not always follow the sweep of the spectrum analyzer, since the laser jitters too fast for the spectrum analyzer to follow. The data was taken with a resolution bandwidth of 30 Hz over an averaging time of 1 s.

The measured FWHM of the beat signal gives us an upper bound on the linewidth of the two lasers. We expect the measured FWHM not to be the final limit for the FWHM of the two lasers. Using the Toptica FALC, a high bandwidth PI controller for laser frequency stabilization, and a high finesse cavity we should be able to obtain a laser with a $\text{FWHM} \approx 1 \text{ Hz}$ [65]. Possible reasons for the increased full linewidth of the two lasers are:

Open laser lid of the homebuilt linear laser The laser lid of the homebuilt linear laser is not yet closed since our current design does not have an electrical feedthrough for the current modulation signal of the laser from the PI-controller. This means that environmental influences can couple into the laser.

Coupling efficiency of the lasers to the cavity The coupling efficiency of transmitted light through the cavity compared to coupled light into the cavity is 10 % for the first-generation cavity and 5 % for the second-generation cavity. The coupling to the second-generation cavity can still be improved. A higher transmission signal

corresponds to a better mode matching of the cavity TEM_{00} mode and the Gaussian beam coupled into the cavity. A better mode matching of the Gaussian beam to the cavity mode gives a better signal-to-noise ratio of the Pound-Drever-Hall error signal.

Fluctuating transmission on the Toptica laser lock The transmission signal of the Toptica laser coupled to the first-generation cavity is fluctuating non-periodically. We attribute this fluctuation to a possible optical feedback problem of the laser.

No fiber noise cancellation We did not actively cancel the phase noise from the optical fibers transferring light from the two lasers to the optical heterodyne mixing setup. When guiding light through a fiber the line shape of the laser can broaden to full width half maxima on the order of 1 kHz [36].

We could not yet attribute the fluctuation of the transmission signal through the first-generation cavity to a specific noise source.

The beat frequency of the two lasers is stable enough to characterize the thermal time constant of the optical resonator and to measure the zero crossing temperature of the optical resonator. Further optimization of both laser frequency-stabilization systems is still required.

8.5 Determining the Zero Crossing Temperature of the Optical Resonator

As described in Sec. 6.2, the relation between temperature changes of the optical resonator, changes of the cavity spacer length and hence changes of the resonance frequency of the optical resonator were discussed. With the heterodyne mixing signal between two lasers stabilized to two different cavities we can measure changes of the beat frequency. Neglecting the pressure fluctuations which are on the 100 Hz scale (as discussed in Sec. 6.4) and assuming that the cavity is vibrationally isolated to the environment, the change in beat frequency is connected to the temperature change of the optical resonator. By changing the temperature of the copper box in the second-generation cavity, we can observe how quickly the beat frequency of the Toptica laser and the homebuilt linear laser changes. However, we need to account for the resonance frequency drifts of the first-generation cavity, which we determined to be approximately 150 kHz. This frequency drift will be the major error component in the following calculations.

8.5.1 Resonance Frequency Drift caused by a Change of Temperature

For the measurement of the frequency drift of the cavity caused by a change in temperature we heated up the copper box in the second-generation cavity to a temperature of

26.3°C and let the system equilibrate for three days at this temperature. We measured the beat frequency before the first temperature change to be 2291.531 MHz. We then increased the set point of the PI control of the temperature of the copper box to 27.5°C. The copper box heated up within 45 min to the set temperature. This temperature increase happened very quickly compared to the expected temperature time constant of the optical resonator. Hence, the heating of the copper box can be seen as a step temperature response for the optical resonator. After reaching the set temperature the PI-controller keeps the temperature of the copper box at a constant value so we can assume that the copper box's temperature is homogeneously distributed and radiates heat homogeneously onto the optical resonator.

After heating up the copper box we measured how the beat frequency between the Toptica and the homebuilt linear laser changes in time due to the temperature change in the second-generation cavity. The beat frequency is proportional to the temperature change, which can be approximated by Newton's law of cooling as given in Eqn. (7.3) for the beat-frequencies

$$f(t) = (f_{\text{initial}} - f_{\text{end}}) \exp\left(-\frac{t}{\tau}\right) + f_{\text{end}}, \quad (8.8)$$

where f_{initial} is the start frequency at the beginning of the temperature change seen by the cavity, f_{end} is the fitted final frequency resulting from the temperature change after waiting for an infinite amount of time and τ is the time constant of the beat signal drift. The measurement of the beat frequency for a temperature step from 26.3°C to 27.5°C is shown in Fig. 8.8.

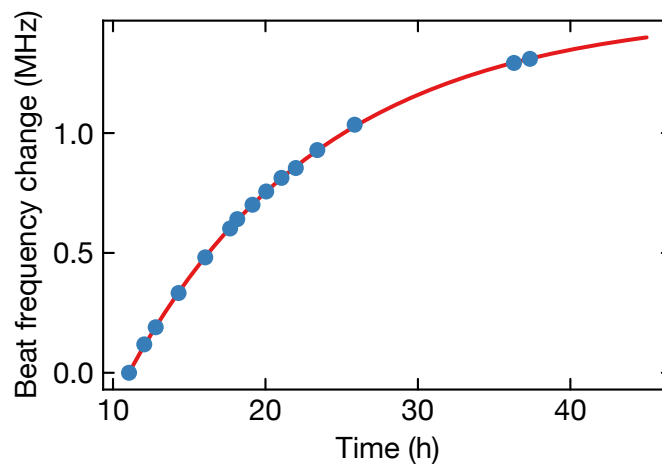


Fig. 8.8 The change of the beat frequency between the Toptica laser and the homebuilt linear laser after a temperature change of the copper box from 26.3°C to 27.5°C is plotted against time (blue points). We obtain a fitted final frequency $f_{\text{final}} = 2294.783(6)$ MHz and a time constant of the exponential decay of $\tau = 13.0(2)$ h (red trace).

Fitting Eqn. 8.8 to the beat frequencies gives a time constant of the resistive coupling between the copper box and the optical resonator. It is given as 13.0(2) h. Further we can get a final frequency $f_{\text{final}} = 2294.783(6)$ MHz from the fit, which gives us the beat frequency value, which corresponds to the response of a temperature change to the beat frequency after waiting an infinite amount of time.

8.5.2 The Zero Crossing Temperature of the Optical Resonator

With the fitted final frequencies f_{initial} from the temperature changes of the cavity we can now determine the zero crossing temperature of the optical resonator. Our optical resonator from Stable Laser Systems was specified by the manufacturer to have a zero crossing temperature of $32.75^\circ\text{C} \pm 1^\circ\text{C}$. We measured drifts of the frequency within the range of 26°C and 36°C . For each temperature change we measured the frequency drift over time and fitted an exponential in the same way as shown in Fig. 8.8.

Using the final frequency value f_{final} as the resonance frequency drift of the optical resonator caused by a temperature change ΔT , we could determine the zero crossing temperature of the optical resonator. In Fig. 8.9 the plot and the fit of the frequency drift of the heterodyne mixing measurement caused by a temperature change is shown.

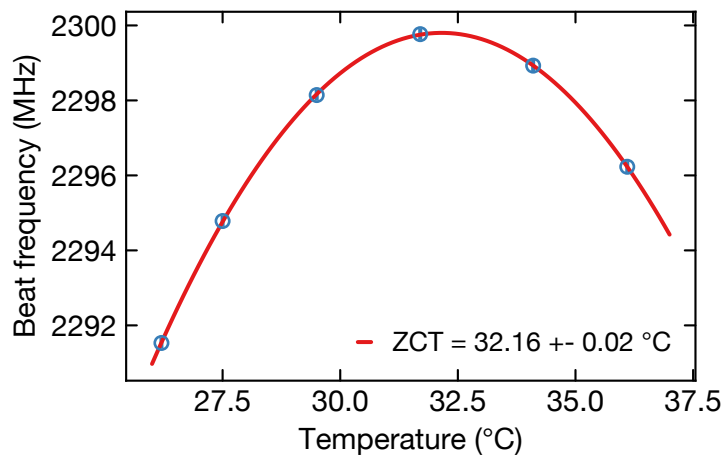


Fig. 8.9 Beat frequency of the heterodyne beat of the Toptica laser and the homebuilt linear laser plotted against temperature of the spacer (blue points). The datapoints are given with error bars obtained from the frequency drift fits. From a parabola fit to the frequency values we obtain a zero crossing temperature (ZCT) of $32.16(2)^\circ\text{C}$.

We were able to determine the zero crossing temperature $T = 32.16(2)^\circ\text{C}$ by fitting the

parabola [44]

$$f_{\text{beat}}(T) = \frac{a}{2}(T - T_0)^2 + \frac{b}{3}(T - T_0)^3 + \text{off}, \quad (8.9)$$

where T_0 is the zero crossing temperature, off is a constant offset on the beat frequencies and a and b are the thermal expansion factors explained in Sec. 6.2.2, to the fitted final frequencies f_{final} after a temperature change. The model ignores linear drifts of the beat frequency, they are determined for our old cavity to be on the scale of 30 mHz/s. At the zero crossing temperature any temperature fluctuations of the environment will have minimal impact on the change of the resonance frequency.

8.6 Thermal Coupling of the Optical Resonator to the Copper Box

To fully characterize the temperature behavior of the second-generation cavity system, we can now also characterize the time constant of the coupling of the optical resonator to the copper box. With the data taken for the zero crossing temperature of the optical resonator we can extract the time constants τ of the fits. They are shown in Fig. 8.10.

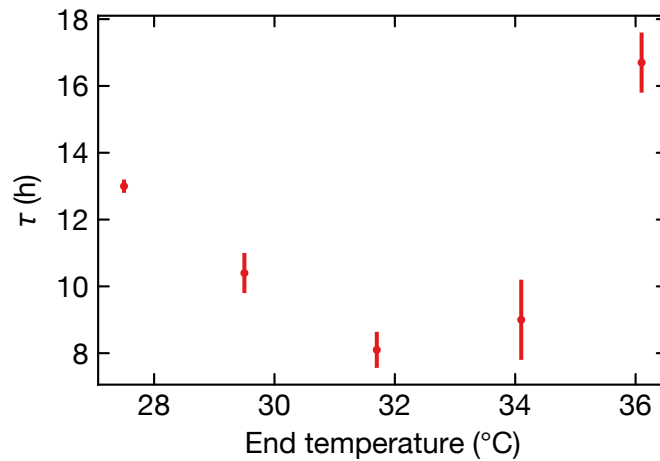


Fig. 8.10 Plot of the characteristic time constants of the frequency drifts induced by a temperature change plotted against the end temperature of each heating process.

We see a temperature dependence of the time constant of the optical resonator. The time constant of the temperature is lower for temperatures which are closer to the zero crossing temperature of the optical spacer and increase for temperatures further away from the zero crossing temperature.

We attribute this phenomenon to a higher heat capacity of the optical resonator. The heat capacity can be shown to be a linear function of the coefficient of thermal expansion α_{CTE} [66], thus we expect a minimum of the timeconstants where α_{CTE} is minimal.

However, this conclusion is not final. We have to take more (continuous) data of the beat frequency to exclude that temperature fluctuations of the first generation cavity caused a decrease of the timeconstant around the zero crossing temperature. Since the frequency changes caused by a temperature change are minimal around the zero crossing temperature, the effect of a drift of the first generation cavity is maximal around the zero crossing temperature.

With a thermal coupling constant of the inner cavity we can fully describe the thermal couplings of the second-generation cavity as given in Fig. 7.6. Close to the zero-expansion coefficient the time constant of the heating process is approximately 8 h.

Chapter 9

Conclusion and Outlook

In this thesis, I reported on the design of a clock laser system for strontium. As a first step, we designed a low-noise and high-bandwidth photodetector for laser stabilization. I summarized the working principle of our photodetector. Although the parasitic capacitance on the photodetector's printed circuit board still limits its bandwidth, we were able to push the parasitic capacitance down to be on the order of the parasitic capacitance of the transimpedance amplifier used in the photodetector. Furthermore, I compared the gain/bandwidth characteristics of our gain-adaptable photodetector and compared the noise characteristics of the fast photodetector board to be on the same level as the Thorlabs PD10A2 for frequencies up to 100 MHz. In conclusion, our photodetector has comparable performance as commercial photodetectors, but can be optimized for many different use-cases in our lab.

Once the full clock laser frequency stabilization setup is complete, we want to transfer narrow-linewidth light from the clock laser to the main experiment through fibers. To not broaden the spectrum of the laser, we employ an active noise cancellation scheme of the acoustic, temperature, and pressure noise that is incident on the fiber. I reported on the design of a fiber-noise-cancellation phase-locked loop with a bandwidth of 20 kHz and a maximal noise suppression of 20 dB.

When running the main experiment and looking at the atom number after the red MOT cooling stage we saw fluctuations of the resonance frequency of the first generation reference cavity in our laboratory on the order of 150 kHz. I analyzed the resonance frequency fluctuations of the first generation cavity and can attribute them to temperature fluctuations inside the vacuum chamber.

As not only the resonance frequency of the first generation cavity was fluctuating but also vacuum problems with this cavity appeared, we decided to build a new reference cavity for both the red MOT transition and the clock transition. I reported on the design and construction of a second-generation cavity. The design of this second-generation cavity is modified from the design of the first generation cavity. To circumvent vacuum problems we decided to build the vacuum housing from stainless steel and to prevent outgassing from resistive heaters we decided to temperature-stabilize the cavity with TEC-elements. We reached a pressure of $6 \cdot 10^{-8}$ mbar. This pressure can still be improved by a low temperature vacuum bakeout. The characteristic coupling constant of the copper box

inside the vacuum housing for heating processes is 8.2 h. Hence, the vacuum housing can damp fast temperature fluctuations of the environment.

Further, I reported on the analysis of shifts of the error signal of the Pound-Drever-Hall frequency stabilization scheme caused by residual amplitude modulation (RAM) of light passing the electro-optic modulator (EOM) crystal. I determined a temperature dependence of the RAM signal for a misalignment of the modulation axis of the crystal in a bulk EOM, but could not see a temperature dependence of the RAM signal in a fiber EOM, where a correct alignment of the fiber axis is ensured by gluing the fiber onto the EOM casing. With two lasers stabilized to the first- and second-generation cavities, we were able to obtain an optical heterodyne beat signal giving us an upper limit of the instantaneous linewidth of the two lasers of $1.7(8) \times 10^2$ Hz at an averaging time of 1 s and a resolution bandwidth of 30 Hz. I reported on determining the zero crossing temperature of the second-generation optical resonator to be $32.16(2)^\circ\text{C}$. Finally I determined the resistive coupling of the second-generation optical resonator to have a time constant of 8 h close to the zero crossing temperature. The time constants of the fitted resonance frequency drifts of the optical resonator are minimal close to the zero crossing temperature and are higher for temperature changes further away from the zero crossing temperature. I attribute this to a change in heat capacity close to the zero crossing temperature which is caused by a change of the coefficient of zero expansion of the optical resonator.

With the first and the second-generation cavity in our laboratory we have a platform to test the performance of the fiber noise cancellation and test the effect of residual amplitude modulation on the error signal of one of the lasers locked to the two cavities. With the addition of a frequency comb to our laboratory we are now able to thoroughly analyze the the changing time constant of the heating process of the second generation optical resonator.

The fiber noise cancellation project is not yet finished. The printed circuit boards will have to be redesigned since the first iteration boards had bugs like oscillating amplifiers that we could not solve on the board (but by external modifications). Additionally, we want to separate the two voltage controlled oscillators on the board with RF-shielding and by placing the oscillators on two separate PCBs. Suggestions for changes of the fiber noise cancellation design are given in Sec. 5.6. The fiber noise cancellation phase locked loop can be adapted to other applications where incoherent noise on e.g. two different fibers must be in common mode.

In conclusion, within this master's thesis project I designed a narrow linewidth laser system for ultracold strontium with low noise electronics and a careful system design. I made many improvements to the existing system but there is still more optimization to do to address the clock transition of strontium atoms with a laser with an instantaneous linewidth on the order of 1 Hz.

Acknowledgments

I would like to begin by thanking **Prof. Immanuel Bloch** for giving me the opportunity to join his group.

I would especially like to thank my supervisor **Dr. Sebastian Blatt** for his guidance and for sharing his passion for physics (and precision) with me. His proofreading of this thesis was invaluable. I am truly thankful for Sebastian's commitment to the success of his students.

I would now like to take the chance and thank the people with whom I have worked in the laboratory.

Dr. Neven Šantić has been a great mentor for me. His introduction to laser frequency stabilization got me started on my master's thesis project. I am thankful for his approachability for any and all questions. His efforts for us Master's students are admirable. I would especially like to thank him for his help during the time of the cavity assembly (when every helping hand was needed), for helping me to take datapoints at the end of my thesis and for proofreading of my thesis.

I would like to thank **Annie Jihyun Park** for being a very good tutor of my first Ultracold Quantum Gases course, for guiding me through the daily laboratory life since then, for being "the nicest" office mate during the time of my master's thesis and for always being responsive to questions.

André Heinz had been my office mate during my early time as an intern in the strontium laboratory. He showed me how to work with optics and vacuum systems. We have had many great discussions, not only about physics, but about every kind of subject.

Dr. Stepan Snigirev has always been very responsive to all my questions and guided me through my first electronics projects. I would like to thank him for helping me with web programming problems.

My co-master student **Etienne Staub** was great company on my journey of learning new things about optics, electronics, mechanics and physics everyday. Especially at the end of this thesis, it was invaluable to have someone to share my problems and my time schedule with.

I would like to thank **Jan Trautmann** for proofreading of this thesis and for helping me with my move.

I would like to thank **Ivan Kokhanovskyi** for building the laboratory's second 689 nm laser, which I used for the characterization of the second generation cavity.

I would like to thank **Mateo Kruljac** for helping me with the, not so glamorous, assembly of the second generation cavity vacuum chamber.

Fabian Finger got me started with my first electronic projects as an intern. Thank you for guiding me through this.

I would like to thank my fellow Bloch-group members who made me feel like being a part of a big family during my time at MPQ. I had a great time discussing physics and technical issues with them. Unfortunately my kicker skills only got slightly better during my time here, although I tried my very best every day.

A special thanks goes to **Karsten Förster** for guiding me through my everyday electronic problems since the start of my internship. His efforts to improve the design of the photodetector and to implement the fiber noise cancellation system were crucial for my master's thesis. I would also like to thank **Anton Mayer** for invaluable technical contributions to the design of the second-generation cavity and for general advice regarding mechanical issues. I would like to thank **Olivia Mödl** for her technical contributions.

Further, I would like to thank **Kristina Schuldt** and **Doreen Seidl** for helping with organizational matters.

I am happy for the support of all my friends in Munich, around Munich and everywhere else.

Finally, I would like to thank my family for their constant support. I would like to thank **Anna** for continuously providing me with new energy and for her constant love and support.

References

- [1] M. Abdel-Hafiz *et al.* *Guidelines for developing optical clocks with 10^{-18} fractional frequency uncertainty*, arXiv: [1906.11495](https://arxiv.org/abs/1906.11495) (2019).
- [2] A. D. Ludlow, M. M. Boyd, J. Ye, E. Peik, and P. O. Schmidt. *Optical atomic clocks*, *Rev. Mod. Phys.* **87**, 637–701 (2015). DOI: [10.1103/RevModPhys.87.637](https://doi.org/10.1103/RevModPhys.87.637).
- [3] M. A. Norcia, J. R. K. Cline, J. A. Muniz, J. M. Robinson, R. B. Hutson, A. Goban, G. E. Marti, J. Ye, and J. K. Thompson. *Frequency Measurements of Superradiance from the Strontium Clock Transition*, *Phys. Rev. X* **8**, 021036 (2018). DOI: [10.1103/PhysRevX.8.021036](https://doi.org/10.1103/PhysRevX.8.021036).
- [4] A. Cooper, J. P. Covey, I. S. Madjarov, S. G. Porsev, M. S. Safronova, and M. Endres. *Alkaline-Earth Atoms in Optical Tweezers*, *Phys. Rev. X* **8**, 041055 (2018). DOI: [10.1103/PhysRevX.8.041055](https://doi.org/10.1103/PhysRevX.8.041055).
- [5] M. A. Norcia, A. W. Young, and A. M. Kaufman. *Microscopic Control and Detection of Ultracold Strontium in Optical-Tweezer Arrays*, *Phys. Rev. X* **8**, 041054 (2018). DOI: [10.1103/PhysRevX.8.041054](https://doi.org/10.1103/PhysRevX.8.041054).
- [6] S. Kondov, C. .-H. Lee, K. H. Leung, C. Liedl, I. Majewska, R. Moszynski, and T. Zelevinsky. *Molecular lattice clock with long vibrational coherence*, arXiv: [1904.04891](https://arxiv.org/abs/1904.04891) (2019).
- [7] A. Ciamei, A. Bayerle, C.-C. Chen, B. Pasquiou, and F. Schreck. *Efficient production of long-lived ultracold Sr_2 molecules*, arXiv: [1705.01422](https://arxiv.org/abs/1705.01422) (2017).
- [8] C.-C. Chen, S. Bennetts, R. González Escudero, B. Pasquiou, and F. Schreck. *Continuous guided strontium beam with high phase-space density*, arXiv: [1907.02793](https://arxiv.org/abs/1907.02793) ().
- [9] M. Takamoto, F.-L. Hong, R. Higashi, and H. Katori. *An optical lattice clock*, *Nature* **435**, 321–324 (2005). ISSN: 1476-4687. DOI: [10.1038/nature03541](https://doi.org/10.1038/nature03541).
- [10] A. D. Ludlow, M. M. Boyd, T. Zelevinsky, S. M. Foreman, S. Blatt, M. Notcutt, T. Ido, and J. Ye. *Systematic Study of the ^{87}Sr Clock Transition in an Optical Lattice*, *Phys. Rev. Lett.* **96**, 033003 (2006). DOI: [10.1103/PhysRevLett.96.033003](https://doi.org/10.1103/PhysRevLett.96.033003).
- [11] M. Yasuda, T. Kishimoto, M. Takamoto, and H. Katori. *Photoassociation spectroscopy of ^{88}Sr : Reconstruction of the wave function near the last node*, *Phys. Rev. A* **73**, 011403 (2006). DOI: [10.1103/PhysRevA.73.011403](https://doi.org/10.1103/PhysRevA.73.011403).
- [12] A. Heinz, A. J. Park, J. Trautmann, N. Šantić, S. Porsev, M. Safronova, I. Bloch, and S. Blatt. “State-dependent optical lattices for strontium”. in preparation. 2019.

- [13] R. B. Hutson, A. Goban, G. E. Marti, L. Sonderhouse, C. Sanner, and J. Ye. *Engineering Quantum States of Matter for Atomic Clocks in Shallow Optical Lattices*, Phys. Rev. Lett. **123**, 123401 (2019). DOI: [10.1103/PhysRevLett.123.123401](https://doi.org/10.1103/PhysRevLett.123.123401).
- [14] X. Zhang, M. Bishof, S. L. Bromley, C. V. Kraus, M. S. Safronova, P. Zoller, A. M. Rey, and J. Ye. *Spectroscopic observation of $SU(N)$ -symmetric interactions in Sr orbital magnetism*, Science **345**, 1467 (2014). DOI: [10.1126/science.1254978](https://doi.org/10.1126/science.1254978).
- [15] S. Stellmer, R. Grimm, and F. Schreck. *Production of quantum-degenerate strontium gases*, Phys. Rev. A **87**, 013611 (2013). DOI: [10.1103/PhysRevA.87.013611](https://doi.org/10.1103/PhysRevA.87.013611).
- [16] B. J. DeSalvo, M. Yan, P. G. Mickelson, Y. N. Martinez de Escobar, and T. C. Killian. *Degenerate Fermi Gas of ^{87}Sr* , Phys. Rev. Lett. **105**, 030402 (2010). DOI: [10.1103/PhysRevLett.105.030402](https://doi.org/10.1103/PhysRevLett.105.030402).
- [17] S. L. Campbell *et al.* *A Fermi-degenerate three-dimensional optical lattice clock*, Science **358**, 90–94 (2017). DOI: [10.1126/science.aam5538](https://doi.org/10.1126/science.aam5538).
- [18] M. S. Safronova, Z. Zuhrianda, U. I. Safronova, and C. W. Clark. *Extracting transition rates from zero-polarizability spectroscopy*, Phys. Rev. A **92**, 040501 (2015). DOI: [10.1103/PhysRevA.92.040501](https://doi.org/10.1103/PhysRevA.92.040501).
- [19] L. Mandel and E. Wolf. *Coherence Properties of Optical Fields*, **37**. (1965). DOI: [10.1103/RevModPhys.37.231](https://doi.org/10.1103/RevModPhys.37.231).
- [20] B. E. A. Saleh and M. C. Teich. *Fundamentals of photonics; 2nd ed.* Wiley series in pure and applied optics. Wiley, 2007. ISBN: 978-1-119-50687-4.
- [21] R. P. Scott, C. Langrock, and B. H. Kolner. *High-dynamic-range laser amplitude and phase noise measurement techniques*, IEEE Journal of Selected Topics in Quantum Electronics **7**, 641–655 (2001). DOI: [10.1109/2944.974236](https://doi.org/10.1109/2944.974236).
- [22] D. Howe, D. Allan, and J. Barnes. “Properties of Signal Sources and Measurement Methods”, 1981, pp. 669–716. DOI: [10.1109/FREQ.1981.200541](https://doi.org/10.1109/FREQ.1981.200541).
- [23] F. M. Gardner. *Phaselock Techniques*. 3rd ed. John Wiley & Sons, Inc., 2005. ISBN: 978-0-471-43063-6.
- [24] W. G. Nagourney. *Quantum electronics for atomic physics and telecommunication*. 2nd ed. Oxford graduate texts. Oxford: Oxford University Press, 2014. ISBN: 978-0-199-66548-8.
- [25] R. Loudon. *The quantum theory of light*. Third Edition. Oxford University Press, 2000. ISBN: 978-0-198-50176-3.
- [26] P. Gallion and G. Debarge. *Quantum phase noise and field correlation in single frequency semiconductor laser systems*, IEEE Journal of Quantum Electronics **20**, 343–349 (1984). DOI: [10.1109/JQE.1984.1072399](https://doi.org/10.1109/JQE.1984.1072399).
- [27] D. S. Elliott, R. Roy, and S. J. Smith. *Extracavity laser band-shape and bandwidth modification*, Phys. Rev. A **26**, 12–18 (1982). DOI: [10.1103/PhysRevA.26.12](https://doi.org/10.1103/PhysRevA.26.12).

- [28] G. D. Domenico, S. Schilt, and P. Thomann. *Simple approach to the relation between laser frequency noise and laser line shape*, Appl. Opt. **49.**, 4801–4807 (2010). DOI: [10.1364/AO.49.004801](https://doi.org/10.1364/AO.49.004801).
- [29] K. J. Åström and R. M. Murray. *Feedback Systems: An Introduction for Scientists and Engineers*. Princeton University Press, 2004. ISBN: 978-069-113576-2.
- [30] J. Bechhoefer. *Feedback for physicists: A tutorial essay on control*, Rev. Mod. Phys. **77**, 783–836 (2005). DOI: [10.1103/RevModPhys.77.783](https://doi.org/10.1103/RevModPhys.77.783).
- [31] P. Horowitz and W. Hill. *The Art of electronics*. Third Edition. Cambridge University Press, 2015. ISBN: 978-0-521-80926-9.
- [32] N. Janša. “A frequency-stable diode laser system for spectroscopy and trapping of Sr atoms”. Master’s Thesis. Fakultät für Physik der Ludwig-Maximilians-Universität München, 2016. URL: http://ultracold.sr/publications/thesis_nejc_jansa.pdf.
- [33] J. Graeme. *Photodiode Amplifiers*. Mc-Graw-Hill, 1995. ISBN: 978-0-471-43063-6.
- [34] X. Ramus. *Transimpedance considerations for High-Speed Amplifiers*. Tech. rep. Texas Instruments Incorporate, 2009. URL: <http://www.ti.com/lit/an/sboa122/sboa122.pdf>.
- [35] *Datasheet Texas Instruments LM6609 operational amplifier*. 2019. URL: <http://www.ti.com/lit/ds/symlink/lmh6609.pdf>.
- [36] L.-S. Ma, P. Jungner, J. Ye, and J. L. Hall. *Delivering the same optical frequency at two places: accurate cancellation of phase noise introduced by an optical fiber or other time-varying path*, Opt. Lett. **19.**, 1777–1779 (1994). DOI: [10.1364/OL.19.001777](https://doi.org/10.1364/OL.19.001777).
- [37] P. A. Williams, W. C. Swann, and N. R. Newbury. *High-stability transfer of an optical frequency over long fiber-optic links*, J. Opt. Soc. Am. B **25.**, 1284–1293 (2008). DOI: [10.1364/JOSAB.25.001284](https://doi.org/10.1364/JOSAB.25.001284).
- [38] D. Ren, K. M. Lawton, and J. A. Miller. *Application of cat’s-eye retroreflector in micro-displacement measurement*, Precision Engineering **31.**, 68 (2007). DOI: <https://doi.org/10.1016/j.precisioneng.2006.02.002>.
- [39] ABRACON LLC; *Datasheet ABLNO*. 2018. URL: <https://abracon.com/PrecisionTiming/ABLJO.pdf>.
- [40] Vectron International; *Datasheet VS-705*. 2014. URL: <https://www.vectron.com/products/vcso/vs705.pdf>.
- [41] Analog Devices AD 8675 operational amplifier. 2019. URL: <https://www.analog.com/media/en/technical-documentation/data-sheets/AD8675.pdf>.
- [42] Texas Instruments LM6624 operational amplifier. 2019. URL: <http://www.ti.com/lit/ds/symlink/lmh6626.pdf>.

- [43] S. H. Wissenberg. “Stabilizing diode lasers to an ultrastable reference cavity”. Master’s Thesis. Fakultät für Physik der Ludwig-Maximilians-Universität München, 2017. URL: http://ultracold.sr/publications/thesis_stephan_wissenberg.pdf.
- [44] T. Legero, T. Kessler, and U. Sterr. *Tuning the thermal expansion properties of optical reference cavities with fused silica mirrors*, J. Opt. Soc. Am. B **27**., 914–919 (2010). DOI: [10.1364/JOSAB.27.000914](https://doi.org/10.1364/JOSAB.27.000914).
- [45] J. Sanjuan, N. Gürlebeck, and C. Braxmaier. *Mathematical model of thermal shields for long-term stability optical resonators*, Opt. Express **23**., 17892–17908 (2015). DOI: [10.1364/OE.23.017892](https://doi.org/10.1364/OE.23.017892).
- [46] J. Millo, D. V. Magalhães, C. Mandache, Y. Le Coq, E. M. L. English, P. G. Westergaard, J. Lodewyck, S. Bize, P. Lemonde, and G. Santarelli. *Ultrastable lasers based on vibration insensitive cavities*, Phys. Rev. A **79**, 053829 (2009). DOI: [10.1103/PhysRevA.79.053829](https://doi.org/10.1103/PhysRevA.79.053829).
- [47] W. Riley. *Handbook of Frequency Stability Analysis*. NIST Special Publication 1065. 2008. URL: <https://tf.nist.gov/general/pdf/2220.pdf>.
- [48] S. Snigirev, A. J. Park, A. Heinz, I. Bloch, and S. Blatt. *Fast and dense magneto-optical traps for strontium*, Phys. Rev. A **99**, 063421 (2019). DOI: [10.1103/PhysRevA.99.063421](https://doi.org/10.1103/PhysRevA.99.063421).
- [49] E. A. Donley, T. P. Heavner, F. Levi, M. O. Tataw, and S. R. Jefferts. *Double-pass acousto-optic modulator system*, Review of Scientific Instruments **76**., 063112 (2005). DOI: [10.1063/1.1930095](https://doi.org/10.1063/1.1930095).
- [50] S. Stellmer. “Degenerate quantum gases of strontium”. PhD Thesis. University of Innsbruck, 2013. URL: <http://www.ultracold.at/theses/2013-stellmer.pdf>.
- [51] U. Sterr, T. Legero, T. Kessler, H. Schnatz, G. Grosche, O. Terra, and F. Riehle. “Ultrastable lasers: new developments and applications”, *Time and Frequency Metrology II*. Ed. by T. Ido and D. T. Reid. Vol. 7431. International Society for Optics and Photonics. SPIE, 2009, p. 33. DOI: [10.1117/12.825217](https://doi.org/10.1117/12.825217).
- [52] J. Alnis, A. Matveev, N. Kolachevsky, T. Udem, and T. W. Hänsch. *Subhertz linewidth diode lasers by stabilization to vibrationally and thermally compensated ultralow-expansion glass Fabry-Pérot cavities*, Phys. Rev. A **77**, 053809 (2008). DOI: [10.1103/PhysRevA.77.053809](https://doi.org/10.1103/PhysRevA.77.053809).
- [53] K. Jousten. *Handbook of Vacuum Technology*. 1st ed. Wiley - VCH, 2016. ISBN: 978-3-527-41338-6.
- [54] K. M. Birnbaum. “Cavity QED with Multilevel Atoms”. PhD Thesis. California Institute of Technology, 2005. URL: https://thesis.library.caltech.edu/2144/1/kmb_thesis_final_oneside.pdf.
- [55] M. Vollmer. *Newton’s law of cooling revisited*, European Journal of Physics **30**., 1063–1084 (2009). DOI: [10.1088/0143-0807/30/5/014](https://doi.org/10.1088/0143-0807/30/5/014).

- [56] RollerTech GmbH - Datasheet FPM. URL: <https://www.kbrt.de/en/applications/fluoro-elastomers-fpm-fkm/>.
- [57] A. Heinz. “Frequency Stabilization of Lasers in an Optical Clock Experiment”. Master’s Thesis. Friedrich-Alexander University Erlangen Nuremberg, 2015.
- [58] E. D. Black. *An introduction to Pound–Drever–Hall laser frequency stabilization*, American Journal of Physics **69.**, 79–87 (2001). DOI: [10.1119/1.1286663](https://doi.org/10.1119/1.1286663).
- [59] N. C. Wong and J. L. Hall. *Servo control of amplitude modulation in frequency-modulation spectroscopy: demonstration of shot-noise-limited detection*, J. Opt. Soc. Am. B **2.**, 1527 (1985). DOI: [10.1364/JOSAB.2.001527](https://doi.org/10.1364/JOSAB.2.001527).
- [60] E. A. Whittaker, M. Gehrtz, and G. C. Bjorklund. *Residual amplitude modulation in laser electro-optic phase modulation*, J. Opt. Soc. Am. B **2.**, 1320 (1985). DOI: [10.1364/JOSAB.2.001320](https://doi.org/10.1364/JOSAB.2.001320).
- [61] W. Zhang *et al.* *Reduction of residual amplitude modulation to 1×10^{-6} for frequency modulation and laser stabilization*, Opt. Lett. **39.**, 1980 (2014). DOI: [10.1364/OL.39.001980](https://doi.org/10.1364/OL.39.001980).
- [62] Q. A. Duong, T. D. Nguyen, T. T. Vu, M. Higuchi, D. Wei, and M. Aketagawa. *Suppression of residual amplitude modulation appeared in commercial electro-optic modulator to improve iodine-frequency-stabilized laser diode using frequency modulation spectroscopy*, Journal of the European Optical Society-Rapid Publications **14.**, 25 (2018). DOI: [10.1186/s41476-018-0092-x](https://doi.org/10.1186/s41476-018-0092-x).
- [63] I. Kokhanovskiy. “Construction of an interference-filter-stabilized diode laser for experiments with ultracold strontium atoms”. Bachelor’s Thesis. Fakultät für Physik der Ludwig-Maximilians-Universität München, 2019. URL: http://ultracold.sr/publications/thesis_ivan_kokhanovskiy.pdf.
- [64] E. Staub. “Developing a High-Flux Atomic Beam Source for Experiments with Ultracold Strontium Quantum Gases”. Master’s Thesis. Fakultät für Physik der Ludwig-Maximilians-Universität München, 2019. URL: http://ultracold.sr/publications/thesis_etienne_staub.pdf.
- [65] M. Notcutt. personal communication. 2019.
- [66] J. Garai. *Correlation between thermal expansion and heat capacity*, Calphad **30.**, 354 (2006). DOI: <https://doi.org/10.1016/j.calphad.2005.12.003>.

Selbstständigkeitserklärung

Hiermit erkläre ich, die vorliegende Arbeit selbständig verfasst zu haben und keine anderen als die in der Arbeit angegebenen Quellen und Hilfsmittel benutzt zu haben.

München, den 01.10.2019

Rudolf Haindl